Liquid crystals in photonic crystal fibers: fabrication, characterization and devices

Scolari, Lara

Publication date:
2009

Document Version
Publisher's PDF, also known as Version of record

Liquid crystals in photonic crystal fibers: fabrication, characterization and devices

Ph.D. Thesis
Lara Scolari

March 14th, 2009

DTU Fotonik
Department of Photonics Engineering

DTU Fotonik
Department of Photonics Engineering
Technical University of Denmark
Ørsteds Plads 345V
DK-2800 Kgs. Lyngby
Denmark

Contents

Preface

The work presented in this thesis has been carried out as a part of my Ph.D. project in the period March 15$^{\text{th}}$ 2006–March 14$^{\text{th}}$ 2009.

The work took mainly place at DTU Fotonik (Department of Photonics Engineering), Technical University of Denmark. A five months research stay was spent at The College of Optics and Photonics (CREOL), University of Central Florida, USA.

The project was financed by the Technical University of Denmark and supervised by

- Anders O. Bjarklev, Professor, dr.techn., DTU Fotonik, Technical University of Denmark, Kgs. Lyngby, Denmark
- Thomas T. Alkeskjold, Ph.D., Crystal Fibre A/S, Birkerød, Denmark
- Lars Eskildsen, Ph.D., KOHERAS A/S, Birkerød, Denmark
- Paolo Bassi, Professor, Department of Electronics, Computer Science and Systems (DEIS), University of Bologna, Italy

Acknowledgements

First of all I would like to thank my supervisors Professor Anders Bjarklev and Dr. Thomas Tanggaard Alkeskjold, for giving me the opportunity to work at DTU Fotonik as a PhD student and for their guidance during the project. I am indebted to Associate Professor Lars Eskildsen, who supervised this project for one year, for the time he found to help me with the equipment in the lab and for always being there whenever I needed to talk about my research progress. My gratitude to co-supervisor Professor Paolo Bassi, from University of Bologna, for being a constant reference point in the last three years.

Many thanks to Research Scientist Sebastian Gauza, who gave me valuable advices about the topic of liquid crystals and guided me in the usage of a number of devices for the characterization of liquid crystals while I was at the College of Optics and Photonics, University of Central Florida, USA. Thanks to his wife Gosia and their son Stasio, for welcoming me so warmly and for the pleasant time we spent together. I would also like to thank Professor Shin-Tson Wu, for giving me the opportunity to join his group for 5 months.

Thanks to Associate Professor Jesper Lægsgaard for always keeping his door open when I had questions about theory and simulations. Thanks to Martin Nordal Petersen for a fruitful collaboration between my group and the Networks group at DTU Fotonik and for a very good friendship. Thanks to Christina Olausson and Danny Noordegraaf not only for a joint collaboration, but also for keeping the lab lively and with a good atmosphere while we were working together. Thanks to my officemates Johannes Weirich and Lei Wei for many scientific discussions and many fun hours. Thanks to my colleagues Michael Frosz, Dmitry Turchinovich, Kristian

Nielsen, Alessio Stefani, Haiyan Ou and Morten Bache for many work and not-work related talks. Thanks to Professor Karsten Rottwitt for keeping a good atmosphere in the group. Thanks to Lars Hagedorn Frandsen for helping with the SEM machine. Thanks to master students Danny Noordegraaf and Anna Chiara Brunetti for being so dedicated to their projects.

Many thanks to Paolo Bassi, Lars Eskildsen, Johannes Weirich, Pablo V. Holm-Nielsen, Lei Wei, Christina Olausson, Sebastian Gauza and Danny Noordergraaf for proof-reading parts of this thesis and give me useful comments.

Finally, I would like to thank my family, Pablo, and all my friends in Copenhagen, in Italy, and around the world, for giving me constant encouragement and taking a good care of me during the last hectic 3 months of this PhD. Thanks to all of you for your patience.

Abstract

In this PhD thesis an experimental and theoretical study of devices based on Photonic Crystal Fibers (PCFs) infiltrated with Liquid Crystals (LCs) is carried out.

PCFs can be divided into two main categories depending on the physical mechanism that provides light guidance. One type of PCF operates by the Modified-Total-Internal-Reflection (M-TIR) principle and has a solid core surrounded by a periodic lattice. The other type of PCF operates for the Photonic BandGap (PBG) effect. This fiber possesses a periodic cladding in which only some frequencies are allowed to propagate. If a "defect" is introduced in this structure, i.e. the periodicity is broken, the frequencies with inhibited propagation in the cladding are trapped in the "defect". The transmission spectrum of these fibers exhibits bandgaps and, therefore, minima and maxima of the transmission.

Liquid Crystals (LCs) are self-organized materials which exhibit very high electro-optic and thermo-optic effects due to high birefringence and high dielectric anisotropy. LCs reorients when an external electric field is applied and their refractive indices are strongly dependent on temperature. The infiltration of these materials into the air-holes of a solid core PCF changes the guiding principle from M-TIR to PBG. The light is confined to the silica core by coherent scattering from the LC-filled holes and the transmission spectrum presents bandgaps. These bandgaps can be tuned by applying an electric field or by varying the temperature. Therefore, tunable all-in-fiber devices with controllable optical properties can be realized, for example tunable filters, electrically controlled switches, polarization controllers and polarizers.

This thesis focuses on the fabrication and characterization of Liquid Crystal Photonic Bandgap (LCPBG) fiber devices which can find applications in optical communication systems and Optical Coherence Tomography (OCT). The physical properties of PCFs and LCs relevant for the thesis are reviewed. The fabrication of Gaussian filters for OCT is investigated. A tapering technique is used to shape the transmission spectrum and Gaussian filters with a broad thermal tunability are achieved. Tunable bandwidth bandpass filters, Polarization Maintaining (PM) filters, gain equalization filters based on nanoparticle-doped LCs, tunable waveplates and notch filters based on Long-Period Gratings (LPGs) in LCPBG fibers are demonstrated. Simulations are performed in order to validate the experimental results. Finally, an LCPBG fiber device which filters the Amplified Spontaneous Emission (ASE) noise caused by Erbium Doped Fiber Amplifiers (EDFAs) is used in an optical transmission system. The performances of the system in terms of Optical Signal-to-Noise Ratio (OSNR) are investigated with and without the filter. The experiments carried out show that the benefits of the filtering are dramatic, proving also that LCPBG fiber devices can be successfully integrated in optical systems.

In conclusion, LCPBG fiber devices exhibit very interesting characteristics that, as shown, make them ready for applications in future optical systems.

Resumé (Danish abstract)

I denne PhD afhandling beskrives et eksperimentelt og teoretisk studie af komponenter baseret på fotoniske krystalfibre infiltreret med flydende krystaller.

Fotoniske krystalfibre kan inddeles i to hovedkategorier afhængigt af den fysiske mekanisme, der sikrer lysets udbredelse i fibrene. Den ene type krystalfibre virker ved Modificeret-Total-Indre-Reflektions (M-TIR) princippet og har en fast kerne omgivet af en periodisk gitterstruktur. Den anden type krystalfibre virker ved den fotoniske båndgabs effekt. Sidstnævnte fibertype indeholder en periodisk kappestruktur i hvilken kun lys med bestemte frekvenser er tilladt udbredelse. Når man introducerer en såkaldt "defekt" i denne struktur, dvs. når man bryder periodiciteten, vil lys med de frekvenser, der ikke er tilladt udbredelse i kappen, blive indfanget i defekten. Disse fibres transmissionsspektre udviser båndgab og derfor minima og maxima i transmissionen.

Flydende krystaller er selvorganiserende materialer, der udviser meget høje elektro-optiske og termo-optiske effekter pga. høj dobbeltbrydning og høj dielektrisk anisotropi. Flydende krystaller re-orienteres, når der påtrykkes et eksternt elektrisk felt, og deres brydningsindices er stærkt temperaturafhængige. Når disse materialer infiltreres i lufthullerne i kappen af en fastkerne krystalfiber ændres det bølgeledende princip fra M-TIR til båndgabseffekt. Lyset er bundet til glasfiberkernen gennem kohærent spredning fra kappehullerne fyldt med flydende krystaller og fiberens transmissionsspektre udviser herigennem båndgabseffekt. Disse båndgab kan ændres gennem påtrykning af elektriske felter eller gennem variation af temperaturen. Derfor kan vi realisere fiberkomponenter med kontrollerbare optiske egenskaber - f.eks. justerbare filtre, elektrisk kontrollerede kontak-

ter, polarisationskontroller og polarisatorer.

Denne afhandling fokuserer på fabrikation og karakterisering af flydende krystal fyldte fotoniske krystalfiber komponenter, der kan anvendes i optiske kommunikationssystemer og indenfor optisk kohærens tomografi. De fysiske egenskaber af krystalfibrene og de flydende krystaller beskrives. Fabrikation af Gaussiske filtre til anvendelse indenfor optisk kohærens tomografi undersøges. Der benyttes en taperingsteknik til at forme transmissionsspektret, og herigennem opnås Gaussiske filtre med en bred termisk justerbarhed. Båndpas filtre med justerbar båndbredde, polarisationsbevarende filtre, filtre til udglatning af forstærkningsspektre baseret på nano-partikel doterede flydende krystaller, justerbare bølgeplader, og notch filtre baseret på langperiodiske fibergitre er demonstreret. Der er udført numeriske simuleringer for at validere de eksperimentelle resultater. Endelig, benyttes en flydende krystal fyldt båndgabsfiber komponent til at filtrere forstærket spontan emissions støj fra en Erbium-doteret fiber forstærker i et optisk transmissionssystem. Systemets virkemåde med hensyn til signal-støj forhold undersøges med og uden filterkomponenten, og de gennemførte eksperimenter viser, at fordelene ved filtrering er betydelige, hvilket også beviser, at flydende krystal fyldte krystalfiber komponenter med fordel kan integreres i optiske systemer.

Konkluderende kan vi sige, at flydende krystal fyldte krystalfiber komponenter har vist sig at have mange interessante egenskaber, der placere dem på tæsklen til anvendelse i morgendagens kommercielle systemer.

PhD publication list

Journal publications

1. **L. Scolari**, S. Gauza, H. Xianyu, L. Zhai, L. Eskildsen, T. T. Alkeskjold, S. -T. Wu, and A. Bjarklev, "Frequency tunability of solid-core photonic crystal fibers filled with nanoparticle-doped liquid crystals," Optics Express **17**(5), 3754–3764 (2009).

2. J. Weirich, J. Lægsgaard, **L. Scolari**, L. Wei, T. T. Alkeskjold, and A. Bjarklev, "Biased liquid crystal infiltrated photonic bandgap fiber," Optics Express **17**(6), 4442–4453 (2009).

3. L. Wei, L. Eskildsen, J. Weirich, **L. Scolari**, T. T. Alkeskjold, and A. Bjarklev, "Continuously tunable all-in-fiber devices based on thermal and electrical control of negative dielectric anisotropy liquid crystal photonic bandgap fibers," Applied Optics **48**(3), 497–503 (2009).

4. M. N. Petersen, **L. Scolari**, T. Tokle, T. T. Alkeskjold, S. Gauza, S. -T. Wu, and A. Bjarklev, "Noise filtering in a multi-channel system using a tunable liquid crystal photonic bandgap fiber," Optics Express **16**(24), 20067–20072 (2008).

5. **L. Scolari**, C. B. Olausson, J. Weirich, D. Turchinovich, T. T. Alkeskjold, A. Bjarklev, and L. Eskildsen, "Tunable polarisation-maintaining filter based on liquid crystal photonic bandgap fibre," Electronics Letters **44**(20), 1189–1190 (2008).

6. D. Noordegraaf, **L. Scolari**, J. Lægsgaard, T. T. Alkeskjold, G. Tartarini, E. Borelli, P. Bassi, J. Li and S. -T. Wu, "Avoided-crossing-based liquid-crystal photonic-bandgap notch filter," Optics Letters **33**(9), 986–988 (2008).

7. G. Tartarini, T. T. Alkeskjold, **L. Scolari**, A. Bjarklev, and P. Bassi, "Spectral properties of liquid crystal photonic bandgap fibres with splay-aligned mesogens," Optical and Quantum Electronics **39**(10-11), 913–925 (2007).

8. T. T. Alkeskjold, **L. Scolari**, D. Noordegraaf, , J. Lægsgaard, J. Weirich, L. Wei, G. Tartarini, P. Bassi, S. Gauza, S. -T. Wu, and A. Bjarklev, "Integrating liquid crystal based optical devices in photonic crystal fibers," Optical and Quantum Electronics **39**(12-13), 1009–1019 (2007).

9. D. Noordegraaf, **L. Scolari**, J. Lægsgaard, L. Rindorf, and T. T. Alkeskjold, "Electrically and mechanically induced long period gratings in liquid crystal photonic bandgap fibers," Optics Express **15**(13), 7901–7912 (2007).

10. **L. Scolari**, T. T. Alkeskjold, and A. Bjarklev, "Tunable gaussian filter based on tapered liquid crystal photonic bandgap fibre," Electronics Letters **42**(22), 1270–1271 (2006).

Conference contributions

1. **L. Scolari**, C. B. Olausson, D. Turchinovich, T. T. Alkeskjold, A. Bjarklev, and L. Eskildsen, "A polarization maintaining filter based on a liquid-crystal-photonic-bandgap-fiber," Proceedings of *European Conference on Optical Communication ECOC 2008*, paper P.1.10, pp. 19–20, Brussels, Belgium (2008).

2. L. Wei, **L. Scolari**, J. Weirich, T. T. Alkeskjold, L. Eskildsen, and A. Bjarklev, "High thermal and electrical tunability of negative dielectric liquid crystal photonic bandgap fibers," Proceedings of *Conference on Lasers and Electro-Optics / The International Quantum Electronics Conference CLEO/IQEC 2008*, paper CThEE5, San Jose (CA), USA (2008).

3. L. Wei, L. Eskildsen, J. Weirich, **L. Scolari**, T. T. Alkeskjold, and A. Bjarklev, "Tunable all-in-fiber waveplates based on negative dielectric liquid crystal photonic bandgap fibers," Proceedings of *IEEE Lasers and Electro-Optics Society Annual Meeting LEOS 2008*, paper MEI, Newport Beach (CA), USA (2008).

4. L. Wei, L. Eskildsen, J. Weirich, **L. Scolari**, T. T. Alkeskjold, and A. Bjarklev, "A dual-function all-in-fiber device based on negative dielectric liquid crystal photonic bandgap fibers," Proceedings of *Asia Optical Fiber Communication and Optoelectronic Exposition and Conference AOE 2008*, paper SuB5, Shanghai, China (2008).

5. A. C. Brunetti, **L. Scolari**, J. Weirich, L. Eskildsen, G. Bellanca, P. Bassi, and A. Bjarklev, "Gaussian filtering with tapered oil-filled photonic bandgap fibers," Proceedings of *1st Workshop on Specialty Optical Fibers and Their Applications WSOF 2008*, pp 113-116, Saõ Pedro (SP), Brazil (2008).

6. **L. Scolari**, S. Gauza, H. Xianyu, L. Zhai, L. Eskildsen, T. T. Alkeskjold, S. T. Wu, and A. Bjarklev, "Nanoparticles doped liquid crystal filled photonic bandgap fibers," Proceedings of *1st Workshop on Specialty Optical Fibers and Their Applications WSOF 2008*, pp 29-32, Saõ Pedro (SP), Brazil (2008). **Awarded with the LEOS-WSOF 2008 Best Student Paper**.

7. J. Weirich, L. Wei, **L. Scolari**, J. Lægsgaard, L. Eskildsen, T. T. Alkeskjold, and A. Bjarklev, "Simulating the bandgap shift of a biased liquid crystal infiltrated photonic crystal fiber," Proceedings of *European Optical Society Annual Meeting EOSAM 2008 Digest TOM 3 -Nanophotonics, Photonic Crystals and Metamaterials*, abstract no. 1261, Paris, France (2008).

8. J. Weirich, J. Lægsgaard, T. T. Alkeskjold, J. S. Hesthaven, **L. Scolari**, L. Wei, L. Eskildsen, and A. Bjarklev, "Biased liquid crystal photonic bandgap fiber," Proceedings of *Conference on Lasers and Electro-Optics / The International Quantum Electronics Conference CLEO/IQEC 2008*, paper CThEE6, San Jose (CA), USA (2008).

9. J. Weirich, L. Wei, **L. Scolari**, A. Bjarklev, and T. T. Alkeskjold, "Liquid crystals and photonic bandgap fiber components," Annual Meeting of the Danish Optical Society (DOPS), Risø National Laboratory, Denmark (2007).

10. **L. Scolari**, T. T. Alkeskjold, D. Noordegraaf, G. Tartarini, P. Bassi, and A. Bjarklev, "Liquid crystal photonic bandgap fiber components,"

Asia Pacific Optical Communications APOC 2007, (invited), published in Optoelectronic Materials and Devices II, proceedings of the SPIE, Volume 6782, paper 678215, Wuhan, China (2007).

11. **L. Scolari**, G. Tartarini, E. Borelli, T. T. Alkeskjold, H. C. M. Hansen, P. Bassi, and A. Bjarklev, "Tunable bandpass filter based on photonic crystal fiber filled with multiple liquid crystals," Proceedings of *IEEE Lasers and Electro-Optics Society Annual Meeting LEOS 2007*, paper TuS4, pp. 319–320, Orlando (FL), USA (2007).

12. T. T. Alkeskjold, **L. Scolari**, D. Noordegraaf, J. Lægsgaard, A. Bjarklev, G. Tartarini, D. Castaldini, P. Bassi, J. Li, S. Gauza, and S. T. Wu, "Integrating optical devices in microstructured optical fibers," Proceedings of *International Conference on Materials for Advanced Technologies ICMAT 2007*, pp. 2–7, (invited), Singapore (2007).

13. T. T. Alkeskjold, **L. Scolari**, D. Noordegraaf, and A. Bjarklev, "Hybrid photonic crystal fiber devices for polarization analysis and control," Proceedings of *International Conference on Spectroscopic Ellipsometry ICSE4*, paper MoP.108, pp. 132, Stockholm, Sweden (2007).

14. D. Noordegraaf, **L. Scolari**, J. Lægsgaard, L. H. Rindorf, and T. T. Alkeskjold, "Electrically tunable long-period gratings in liquid crystal photonic bandgap fibers," Proceedings of *Conference on Optical Fiber Communication OFC 2007*, paper OThP2, Anaheim (LA), USA (2007).

15. **L. Scolari**, T. T. Alkeskjold, and A. Bjarklev, "Gaussian filtering with tapered liquid crystal photonic bandgap fibers," Proceedings of *IEEE Lasers and Electro-Optics Society Annual Meeting LEOS 2006*, paper ThN3, pp. 829–830, Montréal (QC), Canada (2006).

Relevant publications from my Master Thesis

1. **L. Scolari**, T. T. Alkeskjold, J. Riishede, A. Bjarklev, D. S. Hermann, A. Anawati, M. D. Nielsen, and P. Bassi, "Continuously tunable devices based on electrical control of dual-frequency liquid crystal filled photonic bandgap fibers," Optics Express **13**(19), 7483–7496 (2005).

2. M. W. Haakestadt, T. T. Alkeskjold, M. D. Nielsen, **L. Scolari**, J. Riishede, H. E. Engan, and A. Bjarklev, "Electrically tunable photonic bandgap guidance in a liquid crystal filled photonic crystal fiber," IEEE Photonic Technology Letters **17**(4), 819–821 (2005).

3. T. T. Alkeskjold, **L. Scolari**, K. Rottwitt, A. Bjarklev, and C. Peucheret, "Tunable photonic bandgap fiber based devices for optical networks," Proceedings of *International Conference on Transparent Optical Networks / European Symposium on Photonic Crystals (ICTON/ESPC)*, paper Mo.C2.4, invited, Barcelona, Spain (2005).

4. **L. Scolari**, T. T. Alkeskjold, J. Riishede, M. D. Nielsen, D. S. Hermann, A. Anawati, P. Bassi, and A. Bjarklev, "Electrically controllable liquid crystal photonic bandgap fiber with dual-frequency control," Proceedings of *IEEE/LEOS Workshop on Fibres and Optical Passive Components WFOPC 2005*, pp. 14–19, Mondello (PA), Italy (2005).

Books or chapter in books

1. P. Bassi, **L. Scolari**, and R. Zoli, *Propagazione di onde elettromagnetiche* (CLUEB 2006).

2. A. Bjarklev, T. T. Alkeskjold, and **L. Scolari**, chapter 8, *Krystaller i dobbelt forstand* in the book *Optiske horisonter*, pp.141–155 (COM.DTU 2007).

Chapter 1

Introduction

The invention of optical fibers has revolutionized the telecommunication scene due to the large amount of information they can carry. Such waveguides rely on light being guided by the physical mechanism of Total-Internal-Reflection (TIR), which is achieved only if the core has a higher refractive index compared to the outer cladding. Light launched in the core is completely reflected at the interface core/cladding [1–3].

Optical fibers have not only been successful as transmission medium in telecommunication systems, but they have found applications in sensing, fiber lasers, medicine, illumination, non linear processing, amplification etc. Despite their remarkable properties, the increased complexity of the applications in which optical fibers play a role led to a need of fibers that could carry more power, perform better sensing, had multiple cores, higher nonlinearities, higher birefringence and with a widely engineerable dispersion.

Some of these requirements found a solution when, in 1998, the first optical fiber guiding light for a different principle than TIR was proposed [4]. This fiber exhibited a photonic crystal cladding and guided light by the Photonic BandGap (PBG) effect: a periodic structure exhibited frequency intervals where no field solution existed and a "defect" (core) induced in this periodic structure (cladding) allowed the frequencies forbidden in the cladding to propagate in the "defect" itself. With this in mind, light could travel in a core with a lower refractive index compared to that of the surrounding medium, or even in air. These fibers are called Photonic

Crystal Fibers (PCFs).

Two different types of PCFs exist, one guiding light for the PBG effect, as explained above, and one guiding light for a principle called Modified-Total-Internal-Reflection (M-TIR), in which the light is confined in a higher-index core obtained by introducing micro-size air-holes in the cladding [5, 6]. PCFs have unique properties that standard optical fibers do not possess, e.g. endlessly single-mode behavior [7], high-nonlinearities and widely engineerable dispersion which can be exploited for supercontinuum generation [8], high-numerical aperture that can be used for high-power cladding-pumped fiber lasers [9], high birefringence etc.

PCFs have another unique property: they possess micro-holes surrounding the core. These holes can be filled with tunable liquid materials, opening up the opportunity to fabricate all-in-fiber tunable devices. All-in-fiber devices are extremely attractive as they are small, compact and they can easily be coupled to fibers, therefore avoiding alignment issues. Furthermore, being based on fibers, they exhibit circular symmetry and, therefore, polarization sensitivity, such as Polarization Dependent Loss (PDL) and Polarization Mode Dispersion (PMD) can be reduced compared to planar-based components. Moreover, tunability is an attractive property since tunable filters are, for example, needed in the fabrication of tunable fiber lasers, in reconfigurable optical networks, sensing etc.

In 2002 *Bise et al.* [10] demonstrated, for the first time, that it was possible to transform a PCF that guided light for M-TIR into a PBG waveguide by filling its air-holes with a high-index liquid. By tuning the temperature of the high-index liquid, the position of the bandgaps could be tuned.

Polymers were also infiltrated by *Eggleton et al.* in a special type of PCF called "grapefruit"-shaped Microstructured Optical Fiber (MOF). Tunable gratings [11, 12] and tunable birefringence [13] were demonstrated by using this technique and tunability was achieved by changing the temperature of the infiltrated polymer.

Further progress in the field was made in 2003 by *Alkeskjold et al.*, who demonstrated, for the first time, the feasibility of filling Liquid

Crystals (LCs) in PCFs. LCs are organic materials which exhibit very high electro-optic and thermo-optic effects due to high birefringence and high dielectric anisotropy. The reason for using LCs instead of high-index liquids or polymers is due to their short response time as they can be tuned by applying an external electric field. Furthermore, their anisotropy gives more degrees of freedom than conventional isotropic liquids. Devices based on PCFs filled with LC were demonstrated. Thermal [14, 15], electrical [16–18] and optical tunability [19] were achieved. The waveguiding mechanism was also studied and it is still under study since the complexity of such structures is very high [20–23].

The further step naturally coming after a new discovery in the engineering field is the search for applications and the investigation of new devices. This has been the work carried out during this PhD project and the main topic of this thesis. The thesis presents fabricated devices based on Liquid Crystal Photonic Bandgap (LCPBG) fibers which can find applications in optical systems. The fabrication process is described and the characteristics of the obtained devices are illustrated. The experimental results are supported with simulations. It is also found that, by combining a tapering technique, the shape of the transmission spectrum of these devices can be tailored, opening up new applications, for example, the fabrication of filters for Optical Coherence Tomography (OCT) systems. The thesis treats also an experiment in which a LC-filled PCF is inserted in an optical communication systems. The success of the experiment represents the first proof of the suitability of these new devices to be used in optical communication systems.

1.1 Thesis structure

Chapter 2 describes fundamental aspects of PCFs. A basic classification of these fibers is given, introducing the two main types of PCFs and their properties. Focus is given to PCFs which guide light by the M-TIR principle. The PBG effect induced when these fibers are infiltrated with liquids is discussed. The last section of the chapter describes the bandgap formation when LCs are infiltrated in the holes of a PCF. Furthermore, the transmission spectra of PCFs infiltrated with liquids and PCFs infiltrated

with LCs are discussed and compared.

Chapter 3 introduces LCs and their properties. Electro-optical and elastic properties of LCs are discussed. The theory concerning dispersion and temperature dependence of the LC refractive indices is presented and validated with measurements of a commercial LC. An experimental study on the alignment of various LCs infiltrated in micro-size silica capillary is treated at the end of this chapter.

Chapter 4 is devoted to the description of a typical LCPBG fiber device. The procedure for the infiltration of LCs into the PCF is described, together with the setup for the measurement of the transmission spectrum and the measurement of the thermal and electrical tunability. Transmission and tunability are determined for an LCPBG fiber device and compared to simulations obtained with a finite element code. The dynamics of the device is also described. These results are presented in more detail in [24] and in [18].

Chapter 5 documents the experimental work carried out for the fabrication and characterization of Gaussian filters based on tapered LCPBG fiber devices and on oil-based PCFs. The working principle behind these filters is explained. Various filters fabricated by using LCs and oils are described and compared, showing the suitability to be used in OCT, where a broad band source is required to exhibit a Gaussian shape. The experimental results concerning the oil-filter are validated with simulations based on a Beam Propagation Method (BPM). These results can be found in [25–27].

Chapter 6 illustrates various fabricated LCPBG fiber devices which may find applications in optical communication systems. The following devices were demonstrated: a tunable bandwidth bandpass filter, a Polarization Maintaining (PM) filter, a gain equalization filter based on nanoparticle-doped LC, two tunable waveplates and various notch filters based on Long-Period Gratings (LPGs) induced in LCPBG fibers. This work can also be found in [18, 28–32].

Chapter 7 presents an experiment demonstrating that LCPBG fiber devices are suitable for being used in an optical transmission system. A

device filtering the Amplified Spontaneous Emission (ASE) noise caused by amplifiers is fabricated and the advantages given by the filter in terms of signal-to-noise ratio are investigated. The demonstration that LCPBG fiber devices have real applications in optical communication systems is important because it is the first step towards a more mature technology. The results presented in this chapter can be also found in [33].

Finally, the thesis is concluded in Chapter 8.

Chapter 2

Photonic crystal fibers

Optical fibers were discovered in the 1970s and are now the backbone of telecommunication systems due to the large amount of information they can carry. Specially designed optical fibers are also used for a variety of other applications, including sensors, fiber lasers, medicine, illumination and much more. Standard step-index optical fibers guide light by total internal reflection, which takes place only if the core has a refractive index higher than the outer cladding. Light launched in the core is completely reflected at the interface core/cladding and is, therefore guided in the core [1–3].

A new way of guiding light started to appear in 1987, when Yablonovitch [34] and John [35] discovered that compound dielectric materials, deliberately created with a structural size of the same order of magnitude as the wavelength of light, gave the possibility of a new phenomenon named Photonic BandGap (PBG). These novel periodic structures were called photonic crystals in order to emphasize their periodic nature and PBG because they exhibited frequency intervals where no field solution existed. Light incident on a PBG material with a frequency within its PBG is reflected from the material, since the light is not allowed to propagate through it. Only light with certain wavevectors is allowed to propagate in the structure [36]. If a defect, i.e. an irregularity in the regular pattern, is introduced somewhere in this structure, the wavelengths forbidden in the periodic material are now allowed to "stay" in the defect as the photonic crystal running along the defect prevents them from "escaping". The refractive index is not required to be higher than that of the periodic material. By

using this idea light can be trapped inside a hollow core (defect). Therefore, light can even be guided in air.

This is the basic idea behind PBG Photonic Crystal Fibers (PCFs): they possess a 2D periodic dielectric structure invariant in the longitudinal direction, that surrounds a defect. In this way they are able to guide light along the longitudinal direction. The first optical fiber with photonic crystal cladding was demonstrated in 1996 by Knight et al. [5]. This fiber did not guide by the PBG effect but by a principle that is similar to Total-Internal-Reflection (TIR). In 1998 Knight et al. [4] demonstrated the first PCF which guided light by the PBG effect. This fiber represented the start of a new era of optical fiber technology.

This chapter contains an introduction to the field of PCFs. The aim is to briefly introduce the most important properties which make PCFs attractive for the fabrication of optical components. In section 2.1 a classification of different types of PCFs is presented. Section 2.2 introduces index-guiding PCFs and their properties. In section 2.3 the most important properties of PBG fibers are discussed, including liquid-filled PBG fibers and Liquid Crystal (LC)-filled PBG fibers. A short summary is given at the end of the chapter.

2.1 Classification of photonic crystal fibers

In PCFs the periodic arrangement of air-holes in the cladding ensures the guiding of the light into the core. Fig. 2.1 shows a schematic drawing of the cross-section of a typical PCF. Here a structure with a triangular lattice is shown, but other geometries can be used, such as honeycomb or Kagomé [37]. Fiber designed with random cladding structure were also proposed [38]. The core is formed by introducing a defect in the structure, either by omitting an air-hole or by adding extra air-holes. A PCF can be described by the geometry of the air-hole arrangement, by the air-hole size (diameter) d, by the inter-hole distance (pitch) Λ, and by the cladding diameter D. The relative hole-size d/Λ is also a commonly used parameter. The definition of core diameter is not as clear as for standard optical fibers, but for PCFs with a triangular lattice, for example, the core diameter is often defined as $2\Lambda - d$, as depicted in Fig. 2.1.

Two main classes of PCFs can be identified: one consisting of fibers

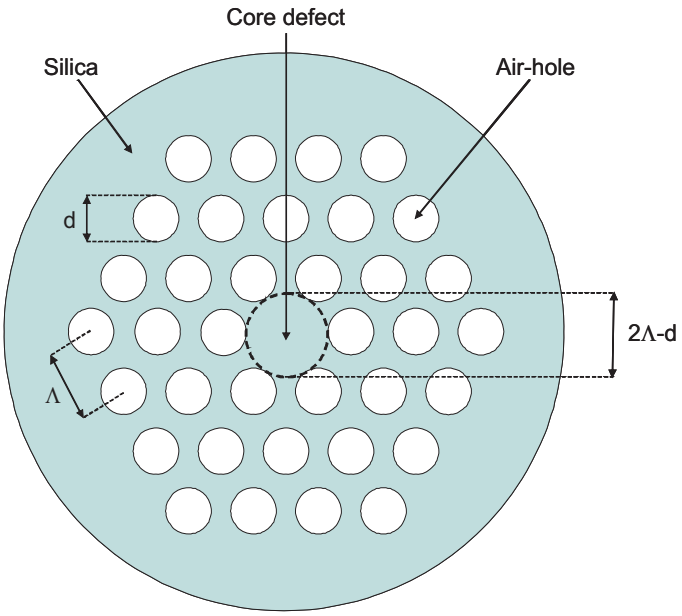

Figure 2.1: Cross-section of a silica PCF. Design parameters such as hole size d and inter-hole distance Λ are illustrated. The core is formed by omitting a central air-hole.

operating by a Modified-Total-Internal-Reflection (M-TIR) principle, similar to that of standard fibers, and referred to as index-guiding fibers, and the other consisting of fibers which guide light by the PBG effect, referred to as PBG fibers. Each of the two main classes can be divided into a number of subclasses, which are determined by the type of fiber structure and their specific properties. For the index-guiding fibers three subclasses can be identified: Large-Mode-Area (LMA), which have relatively large dimension and small effective refractive index contrast to spread out the transverse field, High Numerical Aperture (HNA) fibers, which have a central part surrounded by a ring of relatively large hole, and Highly-Non-Linear (HNL) fibers, which have a very small core in order to increase the nonlinearities. PBG fibers can be separated into Low-Index Core (LIC) fibers and Hollow-Core (HC) fibers. The LIC fibers confine light into the core by the PBG effect but, although the effective refractive index of the core is lower than that of the cladding, most of the power is confined in the material with the

higher index and not in the air-holes. On the contrary, HC fibers have the majority of the optical power in the central air-hole of the structure.

2.2 Index-guiding photonic crystal fibers

Index-guiding PCFs guide light in a solid core by the M-TIR principle. The total internal reflection is caused by the lower refractive index in the microstructured air-filled region with respect to the core index. They are realized by omitting the central hole of the photonic crystal lattice, as illustrated in Fig. 2.1. An optical micrograph of this fiber is shown in Fig. 2.2.

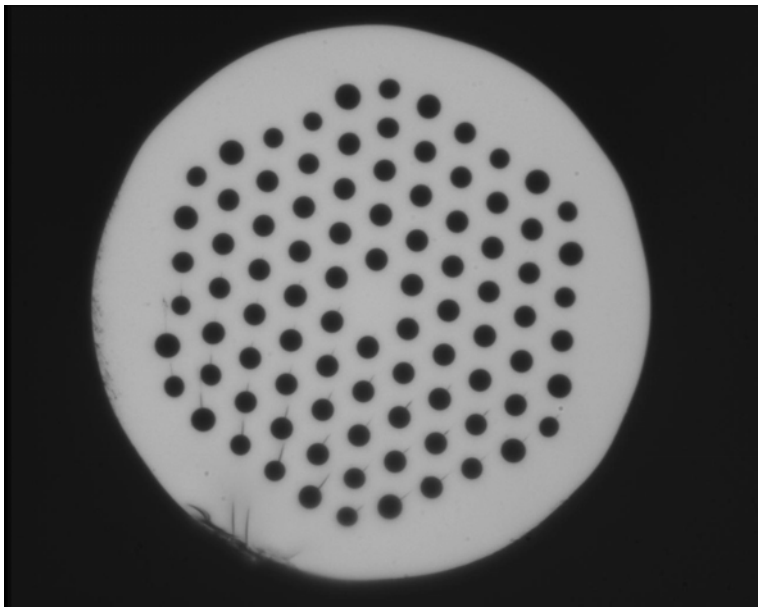

Figure 2.2: Optical micrograph of the end facet of an index-guiding PCF, LMA-15 ($d = 5\mu m$, $\Lambda = 10\mu m$). Picture appear courtesy of Crystal Fibre A/S.

For these fibers the effective index of the guided mode is between the refractive index of the core and the refractive index of the cladding, as in standard fibers. There are many differences between index-guiding PCFs and traditional fibers. First of all, PCFs are made with an unique and pure silica glass instead of using different materials for the core and the cladding (usually, in standard fibers germanium is used to raise the refractive index

of the core). Another important difference between index-guiding PCFs and standard fibers is that for index-guiding PCFs the cladding index is strongly dependent to the wavelength used, while this does not hold for standard optical fibers. In a standard step-index fiber with core radius ρ and core and cladding indices n_{co} and n_{cl}, the number of guided modes is determined by the V value [39]

$$V = \frac{2\pi\rho}{\lambda}\sqrt{n_{co}^2 - n_{cl}^2} \tag{2.1}$$

where λ is the wavelength of the light launched in the fiber. V must be less than 2.405 for the fiber to be single-mode. For standard optical fibers, the cladding index is not wavelength-dependent and thus single-mode fibers are in fact multimode for light of sufficiently short wavelength because V increases as λ decreases. For index-guiding PCFs, the effective refractive index of the cladding can be understood as the average index in the cladding weighted by the intensity distribution of the light. At shorter wavelengths the field becomes more concentrated in the silica regions and avoids the holes and the effective cladding index rises. Therefore, the difference between the core and cladding refractive indices decrease as the wavelength decreases and counteracts the increase in V given by the term λ at the denominator. This allows for endlessly single mode operation from ultra violet (UV) to infrared wavelengths [7]. For an index-guiding PCF with a triangular lattice of air-holes, the relative hole-size d/Λ has to be less than 0.4 to guarantee endlessly single mode behavior [40, 41]. The endlessly single-mode behavior can also be understood if we consider the glass space between two neighboring holes like a pathway along which light can "escape" from the core. The periodic material is like a modal filter: if the lobe of the fundamental mode is close to 2Λ and d/Λ is smaller than 0.4, the fundamental mode is not able to "escape" from the "sieve". Higher order modes can "escape" from the core using the pathways of glass between the air holes [6], since their lobe dimensions are smaller. Consequently, the fiber is single-mode. On the contrary, if the fiber is produced with a d/Λ larger than 0.4, successive higher order modes are trapped in the core because they cannot "escape" through the glass strands. Therefore, a correct choice of the geometry can guarantee that only the fundamental mode is guided, pushing the second-order mode cut-off to an infinitely high frequency.

Index-guiding PCFs have other interesting features: they are more

bending resistent than standard optical fibers and they have unique dispersion properties that standard optical fibers do not possess. On the other hand, PCFs present some problems: birefringence since it is difficult to avoid defects and non-uniformities during the fabrication process and higher losses with respect to standard optical fibers.
In this thesis, among the many different types of index-guiding fibers, only LMA type fibers will be used. Typical values of losses for these fibers are about 2dB/km at 1550nm and 7dB/km in the wavelength range 700-1000nm (for a LMA-10 [42]).

2.3 Photonic bandgap fibers

PBG fibers guide light by the true PBG effect. The light is confined in the low-index core as the PBG effect makes propagation in the microstructured cladding region impossible for certain wavelengths. In other words the core is the defect of a perfect structure and the presence of such a defect allows for the existence of modes at frequencies that fall inside the PBG. Therefore, these kinds of fibers may only support guided modes with certain transmission windows determined by the periodic lattice surrounding the low-index or hollow core. Fig. 2.3 shows an example of an HC PBG fiber. The fiber has a triangular arrangement of air-holes with an inter-hole distance of $3.8\mu m$ and a central core with a diameter of $10.9\mu m$ obtained by removing 7 hexagonal unit cells of the cladding.

An intuitive explanation about the nature of the guided mode in the hollow core of the fiber can be given. By observing Fig. 2.3, it is easy to notice that the microstructured cladding of this fiber presents a large number of silica strands. Each isolated silica strand supports many distinct waveguide modes, each with a different value of propagation constant β. Since the silica strands are close to each other, they couple to each other and they form bands of modes, each band now covering a range of β values. This is a very important difference with respect to standard fibers or index-guiding PCFs. Standard fibers or index-guiding PCFs have a continuum of coupled cladding modes, while PBG fibers support a discrete set of cladding modes separated by bandgaps. When an air-hole defect is introduced in the structure, a core mode can be confined in the defect. This core mode falls between the bands of cladding modes and, if the fiber is HC, it propagates in air. Therefore, its effective index n_{eff} is less than 1.

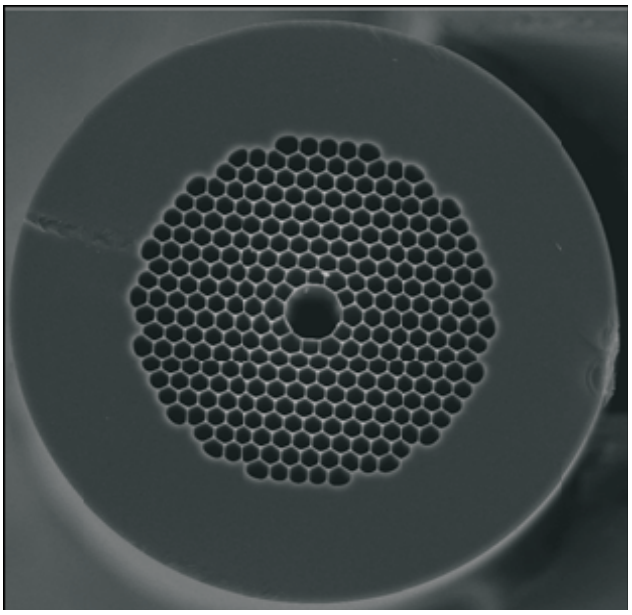

Figure 2.3: SEM of the end facet of a PBG fiber, HC-1550 (core diameter=10.9μm, $\Lambda = 3.8\mu m$). This fiber exhibits a bandgap around 1550nm. Picture appear courtesy of Crystal Fibre A/S.

This is because, in general, the effective index of the core mode has to be lower than the material forming the core, in order to give rise to a confined mode. For standard optical fibers, $n_{co} > n_{eff,co} > n_{cl}$ must hold in order for the mode in the core to be oscillatory and for the modes in the cladding to be exponentially decaying. For PBG fibers, according to the explanation above, the transmission spectrum will exhibit bandgaps and, for HC fibers, the mode will propagate in air with a n_{eff} less than 1. This offers the possibility of minimizing the effects of the material loss and dispersion, allowing for high power transmission.

An important difference between PBG fibers and index-guiding PCFs is that single-mode guidance can be obtained for a broad frequency range in case of PBG fibers (depending on the structure of the fiber) but not for an infinite frequency range, as for index-guiding PCFs. Similarly to index-guiding PCFs, PBG fibers are fabricated with a single material, without the need of using dopants to increase the refractive index. The

losses are high compared to standard fibers or index-guiding PCFs. The fiber shown in Fig. 2.3 presents a loss of about 20dB/Km at 1550nm. It is believed that a reduction of losses may be achieved by improving the axial uniformity of the structure [43].

2.3.1 Liquid-filled photonic bandgap fibers

When an index-guiding PCF is infiltrated with a liquid having a higher refractive index with respect to silica, PBGs are formed since the structure supports a discrete set of cladding modes [10]. The discretization of cladding modes is caused by the cladding structure, that consists of a number of separated index-guiding waveguides. The modes supported by these high-index rods couple together and form bands of modes which are nearly degenerate, i.e. they have approximately the same refractive index. Each band corresponds to coupled bands of LP_{01}, LP_{11}, LP_{21} modes, which are separated by bandgaps. If a core defect is introduced in this structure, the fiber will support a mode falling in between the bands of cladding modes and having an effective index lower than silica [20]. This core mode, if excited, cannot couple to the cladding modes, since its effective index is too far from the effective index of the cladding modes. Light cannot be guided in the core at the wavelengths at which the cladding modes cross the silica line, since at these wavelengths the effective index of the cladding equals the silica refractive index and the cladding structure becomes transparent. Therefore, minima in the transmission spectrum will appear at these wavelengths.

Fig. 2.4 shows the LP_{01}, LP_{11}, LP_{21} cladding modes together with the PBG mode in the core and the silica refractive index. The dispersion of silica was taken into account by using the Sellmeier equation. The structure simulated in Fig. 2.4 is made for a structure of 5×5 high-index rods. The material is isotropic with a refractive index of 1.5. The background material is silica, the hole diameter d is $3.45\mu m$ and the inter-hole distance Λ is $7.15\mu m$. The simulation tool named MIT Photonic Bands (MPB) was used to calculate the effective indices. This code is based on a plane-wave expansion method [44–46].

2.3.2 Anti-resonance

Information about the spectral characteristics of a liquid-filled PBG fiber can be obtained by considering the high-index waveguides as Fabry-Perot resonators. Narrowband resonances of these resonators correspond to transmission minima for the light propagating in the core, while wide antiresonances correspond to a high transmission coefficient for the low-index core waveguide [47, 48]. The resonant condition is found by calculating the cut-off of a single waveguide [49]. At the modal cut-off the effective refractive index of the cladding equals the refractive index of silica and the entire waveguide structure becomes effectively transparent [50]. The light is, therefore, not guided and this corresponds to a minimum in the transmission spectrum. The wavelengths at which minima appear in the transmission spectrum can be estimated from the cut-off condition

$$\lambda_m = \frac{2d\sqrt{n_2^2 - n_1^2}}{m + 1/2} \tag{2.2}$$

where λ_m is the cut-off wavelength of the mode m, d is the diameter of the high-index rods, n_2 and n_1 are the isotropic indices of the liquid infiltrated in the fiber and the material (silica) and m is an integer number which corresponds to the modal number.

Fig. 2.4 shows, together with the cladding modes, the cut-off wavelengths calculated with Eq. (2.2). There is excellent agreement between the cut-off wavelengths calculated with this model and the simulated bandgaps. The anti-resonance model is very useful because, in order to determine the spectral properties of a liquid-filled PBG fiber, only the individual properties of the high-index waveguides need to be known, rather than their position and number. Only the refractive index of the high-index inclusions n_2, the index of the material n_1 and the diameter of the inclusions d are needed to calculate the cut-off wavelengths.
Eq. (2.2) also shows that the position of the cut-off can be varied by changing the refractive index of the liquid infiltrated in the holes. Therefore, by using a liquid with a tunable refractive index, tunability of the bandgaps can be achieved. If n_2 increases, the bandgaps will move towards longer wavelengths and vice versa.

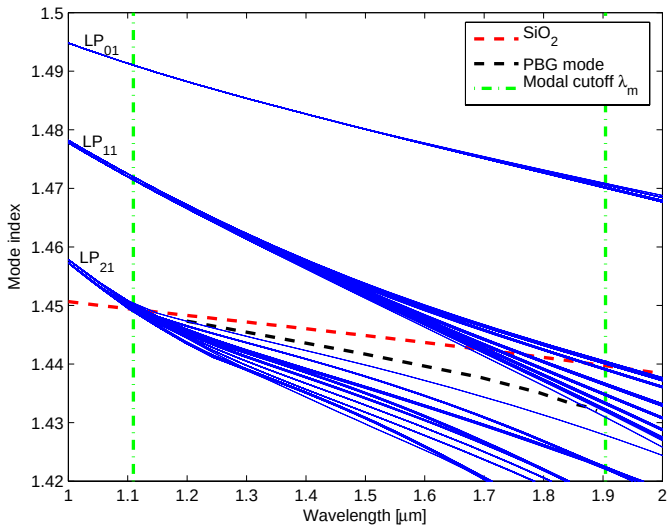

Figure 2.4: Simulated effective mode indices of the isotropic high-index rods (blue lines) and simulated core mode (black line). The cut-off wavelengths of the high-index rods are also calculated by using Eq. (2.2) (green lines) and show good agreement with the simulate ones.

2.3.3 Liquid crystal photonic bandgap (LCPBG) fibers

When LCs are infiltrated in the holes of a PCF, the mechanism of bandgap formation is the same as the one described for isotropic liquids. In fact, LCs have refractive indices higher than that of silica and the high-index rods form isolated waveguides. From Fig. 2.4, we know that the first band of coupled cladding modes is made of the LP_{01} modes, the second of the LP_{11} modes and the third of the LP_{21}. LP_{11} modes consist of a combination of coupled TE_{01}, TM_{01} and HE_{21}, while the LP_{21} modes are a combination of EH_{11} and HE_{31}. The electric field distribution and the intensity distribution of these modes are illustrated in Fig. 2.5. The modes forming each band are "nearly" degenerate if the air-holes are filled with an isotropic material. In the case of anisotropic materials, such as LCs, these modes loose their degeneracy since the refractive index experienced by each mode is different. If we take, for example, the TE_{01}, TM_{01} and HE_{21}, we notice that the electric field distribution is different and therefore the modes will experience a differ-

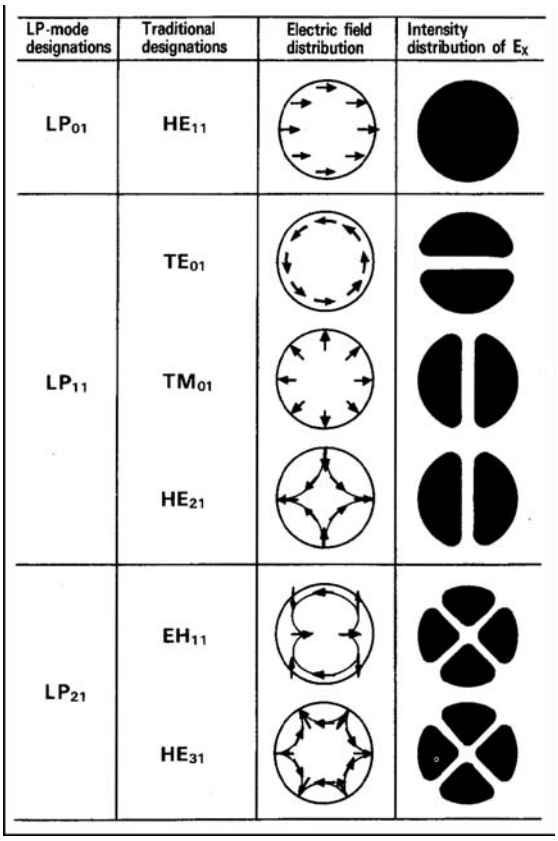

Figure 2.5: Electric field distribution and intensity distribution of LP modes [51]. Reprinted with permission from Elsevier.

ent refractive index in the x-, y- or z- direction, depending on the alignment of the LC. Therefore, additional transmission dips in the transmission spectrum are found for LCs with respect to isotropic materials, as a result of the splitting of the degeneracy of the modal cut-off [22]. This can be observed in Fig. 2.6, where simulated spectra of an isotropic liquid-filled PCF and of an anisotropic LC-filled PCF are compared [22]. The parameters of these simulations are: hole size $d = 1.55\mu m$, inter-hole distance $\Lambda = 5\mu m$, refractive index of silica $n_{SiO2} = 1.45$, LC extra-ordinary refractive index $n_e = 1.7$ and ordinary refractive index $n_o = 1.5$. In the isotropic case, $n_e = n_o$. The transmission spectra were evaluated by using a full-vectorial beam propaga-

tion method and taken after beam propagated along the fiber at $z = 1mm$.

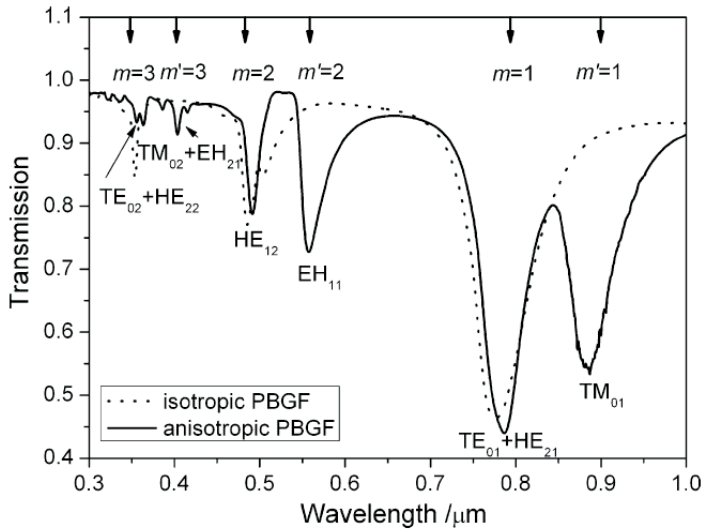

Figure 2.6: Simulated transmission spectra for an isotropic liquid-filled PCF and for an anisotropic LC-filled PCF [22]. Reprinted with permission from Elsevier.

2.4 Summary

In this chapter PCFs were introduced and their unique properties discussed. Two types of fibers, index-guiding PCFs and PBG fibers were presented and their characteristics discussed. Special focus was given to index-guiding PCFs filled with isotropic liquids and anisotropic LCs. When filled, these fibers start guiding light for PBG effect, exhibiting bandgaps in their transmission spectrum. The differences between the isotropic and anisotropic case were underlined.

Chapter 3

Liquid crystal theory

Usually, matter is considered to have three different states: solid, liquid and gas. However, this is a simplification and there are states of matter that do not fall into any of these three categories, for example plasma at very high temperatures, superfluid helium at very low temperatures or Liquid Crystals (LCs). LCs are fascinating materials which flow like liquids and exhibit, at the same time, optical birefringence like crystalline solids. They possess much larger electro-optical, thermo-optical and opto-optical coefficients than any other known materials [52–54]. For this reason, LCs are of great interest and have been largely used for commercial products such as notebook computer displays, desktop monitors, mobile phones, high-definition televisions, but also for other types of applications, for example as beam steerers, tunable focus lenses, polarization devices, tunable filters for telecommunication purposes [55] or in nonlinear optics as soliton waveguides [56, 57].

In this chapter the main features of LCs will be rapidly recalled to introduce terms, definitions and properties used in the rest of the thesis. The interested reader may however refer to [52–55, 58] for a comprehensive description of the properties of LCs. In section 3.1 an overview of various LC types and a description of the phases that they exhibit is provided. Section 3.2 and 3.3 describe, respectively, thermal and dispersion properties of LCs. Section 3.4 describe their elastic properties, section 3.5 discusses their dielectric properties and section 3.6 the LC elastic free-energy. In section 3.7, the effect of the application of an external electric field is described. Finally, section 3.8 presents a study on the alignment of various

LCs infiltrated in a silica capillary. A short summary is given at the end of the chapter.

3.1 Liquid crystal phases

LCs have a certain number of characteristics that make them unique. They consist of organic molecules which can have a rod-like (calamitic LCs) or a disk-like (discotic LCs) shape. The most used ones are the rod-like LCs and these are also the ones considered in this thesis.

LCs can be found in an intermediate phase possessing no order in at least one direction and, at the same time, showing a degree of anisotropy [53]. LCs possess orientational order, i.e. the symmetry axis of the molecules is on average parallel to a well-defined direction, $\vec{n}$, called *director* and often denoted as a unit vector $\widehat{n}$. A positional (or translational) order has also been observed for certain phases of liquid crystalline materials, i.e. the system of molecules is invariant under translation by an integer number of the lattice translation vector.

The size of a LC molecule is in the order of several nanometers and the length is five or more times larger than its width. Fig. 3.1(a) and Fig. 3.1(b) show, respectively, the chemical structure and the space-filling model of a well-known LC 4'-n-pentyl-4-cyano-biphenyl (abbreviated as 5CB). The molecule is rod-like (or cylindrical) and it is, therefore, possible to regard it as a rod (or a cylinder), as shown in Fig. 3.1(c). More in detail, the biphenyl core is rigid, while the hydrocarbon chain is a flexible tail. In fact, it is the combination of rigidity and flexibility which allows these materials to exhibit liquid crystal phases (LC mesomorphism). It is known that completely flexible molecules most likely will not create an orientational order, being rather isotropic materials while in liquid state. On the contrary, completely rigid molecules would go from an isotropic phase to a crystalline phase with a temperature decrease, without experiencing any liquid crystal phase.

Fig. 3.2 shows examples of phases that rod-like molecules may form. At high temperature, as shown in the right of Fig. 3.2, the LC is in the isotropic phase and the molecules do not have orientational nor positional order and the long and short axis of the molecules can point in any direction.

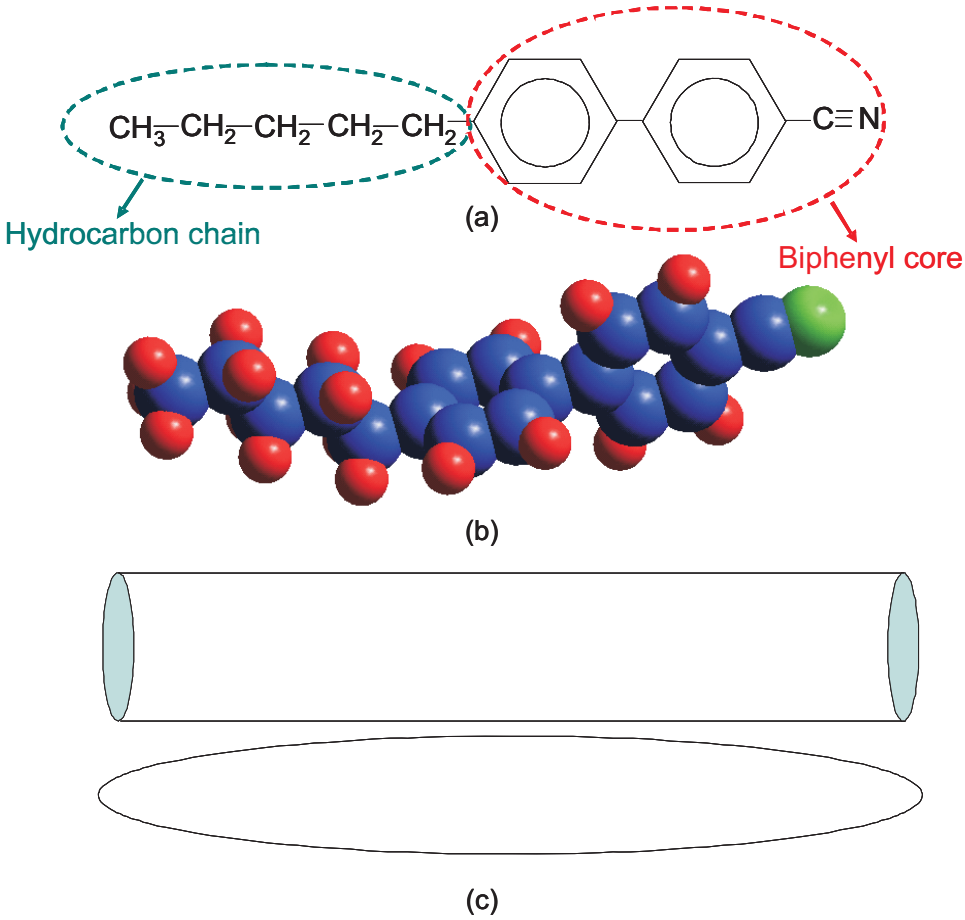

Figure 3.1: Example of a single molecule LC, 5CB: (a) chemical structure, (b) space-filling model, (c) physical model.

By decreasing the temperature, the material goes into a *nematic* phase, in which the molecules possess orientational, but not positional order. The long axis of the molecules has a preferred direction $\widehat{n}$ around which the molecules fluctuates because of thermal motion. Since there are an equal number of molecules pointing in one direction than in the opposite, the director is invariant to a 180° rotation, which mathematically means $\widehat{n} \leftrightarrow -\widehat{n}$ [58, 59]. LCs exhibit also full rotational symmetry around $\widehat{n}$. By further decreasing the temperature, the LC may transform through a phase transition into a

smectic-A phase, in which the molecules have partial positional order and tend to arrange themselves in layers. In this phase, the director is perpendicular to the layers direction. If the temperature is further decreased, the *smectic-C phase* appears, in which the director is not perpendicular to the layers anymore, but tilted. Several phases with higher positional order of the molecules are known and detailed in specific literature, i.e. E, B, K, and others [53]. At low temperature, the material is in the crystal phase.

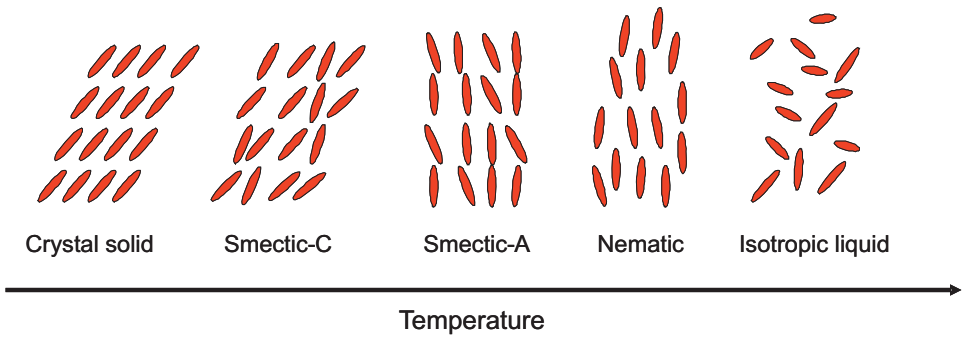

Figure 3.2: Phases of rod-like molecules versus temperature.

In order to specify the amount of orientational order in a LC phase, the order parameter S is used

$$S = \frac{1}{2}\langle 3\cos^2\theta - 1\rangle \tag{3.1}$$

where $\langle\rangle$ indicates thermal averaging and θ is the angle between each molecules and the director $\widehat{n}$. If the molecules are perfectly oriented (crystal state), then $\theta = 0$ and $S = 1$. On the contrary, if the molecules are randomly oriented around $\widehat{n}$, then $S = 0$ and there is no orientational order, i.e. the material is in its isotropic state. Mesomorphic behavior is observed for the liquid crystalline materials when the order parameter S is between 1 and 0. Therefore, the higher the value of the order parameter, the more ordered the LC phase is. The order parameter decreases as the temperature increases and most common values of S are between 0.3 and 0.8 for rod-like liquid crystals.

The LCs discussed in this section are called *thermotropic* as the transition from one phase to another occurs when the temperature is changed.

There is another type of LC called *lyotropic* which is the most common form of LCs in nature and it is exhibited by molecules which are mixed with a solvent. For lyotropic LCs, the transition between one phase to another happens when the solvent concentration is varied. Examples of these LCs are solutions of biomolecules such as cell membranes, DNA or viruses [60].

3.2 Temperature effect on liquid crystal refractive indices

3.2.1 General equations

The temperature effect is important in case of LC devices. In fact, a temperature change induces a change of the order parameter and, therefore, a change of the extraordinary (n_e) and ordinary (n_o) refractive indices. This effect can be exploited in the fabrication of tunable LC devices in which a desired temperature adjustment may vary the properties of the device. It can also be an unwanted effect if, for example, an external electric field is applied to tune the device and temperature stabilization might be required in order to avoid temperature drifts.

The birefringence Δn is the difference between n_e and n_o and the average refractive index $\langle n \rangle$ is defined as [55]

$$\langle n \rangle = \frac{n_e + 2n_o}{3} \tag{3.2}$$

Therefore, n_e and n_o can be rewritten

$$n_e = \langle n \rangle + \frac{2}{3}\Delta n \tag{3.3}$$

$$n_o = \langle n \rangle - \frac{1}{3}\Delta n \tag{3.4}$$

When the temperature is not too close to the clearing point, that is the temperature at which LCs become isotropic, the Haller [61] approximation can be used in order to express the temperature dependence of Δn

$$\Delta n(T) \approx (\Delta n)_o (1 - \frac{T}{T_c})^{\beta} \tag{3.5}$$

where $(\Delta n)_o$ is the birefringence in the crystalline state ($T = 0K$), T_c the clearing temperature of the LC and β is a material constant. The temperature dependence of the average refractive index is linear [62]

$$\langle n \rangle = A - BT \tag{3.6}$$

By substituting Eq. (3.5) and Eq. (3.6) into Eq. (3.3) and Eq. (3.4), the temperature dependence of n_e and n_o is derived [63]

$$n_e(T) \approx A - BT + \frac{2(\Delta n)_o}{3}(1 - \frac{T}{T_c})^\beta \tag{3.7}$$

$$n_o(T) \approx A - BT - \frac{(\Delta n)_o}{3}(1 - \frac{T}{T_c})^\beta \tag{3.8}$$

This is the so-called four-parameter model for the description of the temperature dependence of the LC refractive indices [63].

3.2.2 An example

The parameters A, B and $(\Delta n)_o, \beta$ can be obtained by a two-stage fitting of the measured refractive indices to Eq. (3.6) and Eq. (3.5). The refractive indices at various temperatures and wavelengths were measured by using a multiwavelength Abbe refractometer. The one used was an Atago model DR-M4. These measurements were taken at the College of Optics and Photonics (CREOL), University of Central Florida. The refractive indices were measured at different wavelengths (450 nm, 486 nm, 546 nm 589 nm, 633 nm and 656 nm) by using different interference filters. The temperature was generally varied from $15°C$ to $55°C$ in steps of $5°C$. Table 3.1 and 3.2 list the measured ordinary and extraordinary refractive indices of a commercially available negative dielectric liquid crystal called MLC-6884 from Merck which has a clearing temperature of $74.5°C$. The asterisk indicates the impossibility to read the value of the refractive index on the Abbe refractometer, since it was below the working range of the device. After measuring the temperature dependent n_e and n_o, the data at one wavelength were arranged into $\langle n(T) \rangle$ and $\Delta n(T)$ and the parameters A, B and $(\Delta n)_o, \beta$ could be obtained in a fairly straightforward way by using fitting tools available in commercial mathematical softwares. This technique is very useful for simulations since the refractive indices can be extrapolated for any temperature. For the measured LC, the values of the calculated four parameters are shown in Table 3.3. Fig. 3.3 shows the measured values of n_e and n_o at

T[°C]	486nm	546nm	589nm	633nm	656nm
15	*	1.48373	1.48116	1.47896	1.47803
20	*	1.48246	1.48036	1.47723	1.47660
25	*	1.48146	1.47893	1.47593	1.47556
30	*	1.48020	1.47743	1.47486	1.47386
35	*	*	1.47650	1.47373	1.47280
40	*	*	1.47556	1.47263	1.47200
45	*	*	1.47400	1.47123	1.47080
50	*	*	1.47316	1.47026	1.46973
55	*	*	1.47210	1.46933	1.46883

Table 3.1: Measured ordinary refractive index of MLC-6884 for various wavelengths and temperatures.

T[°C]	486nm	546nm	589nm	633nm	656nm
15	1.59353	1.58523	1.58133	1.57760	1.57643
20	1.59030	1.58226	1.57773	1.57446	1.57320
25	1.58660	1.57866	1.57490	1.57116	1.56996
30	1.58293	1.57510	1.57133	1.56733	1.56640
35	1.57930	1.57150	1.56750	1.56383	1.56250
40	1.57513	1.56740	1.56343	1.55970	1.55866
45	1.57056	1.56306	1.55896	1.55550	1.55420
50	1.56590	1.55823	1.55456	1.55106	1.55000
55	1.56033	1.55306	1.54923	1.54570	1.54433

Table 3.2: Measured extraordinary refractive index of MLC-6884 for various wavelengths and temperature.

589nm and 656nm, together with the estimated ones (solid lines) using the four-parameter model. The estimated curves fit very well the experimental data, as it can be observed in the same figure. By deriving Eq. (3.7) and Eq. (3.8), the temperature gradient for n_e and n_o can be derived

$$\frac{dn_e}{dT} = -B - \frac{2\beta(\Delta n)_o}{3T_c(1-\frac{T}{T_c})^{1-\beta}} \tag{3.9}$$

$$\frac{dn_o}{dT} = -B + \frac{\beta(\Delta n)_o}{3T_c(1-\frac{T}{T_c})^{1-\beta}} \tag{3.10}$$

From Eq. (3.9) it can be noticed that n_e decreases as the temperature in-

λ	A	B	Δn	β
546nm	1.52292	0.00036	0.10772	0.25220
589nm	1.52123	0.00042	0.10535	0.23220
633nm	1.51824	0.00042	0.10429	0.23114
656nm	1.51725	0.00042	0.10406	0.23664

Table 3.3: Four-parameters values (A, B, Δn, β) describing the temperature dependence of MLC-6884 refractive indices.

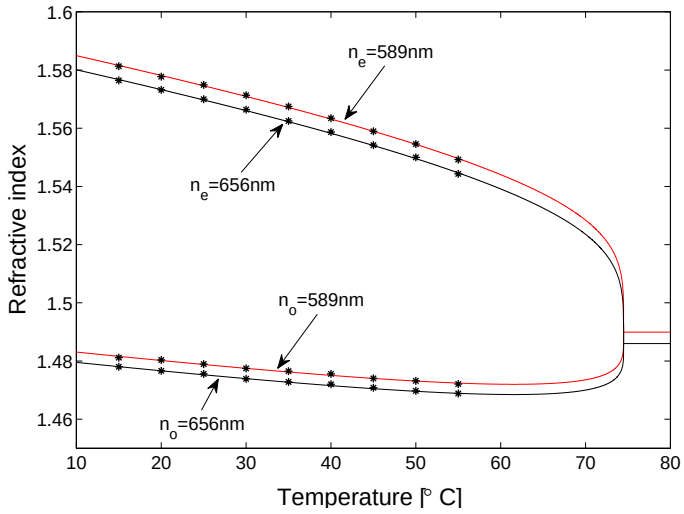

Figure 3.3: Measured (dots) and estimated (solid lines) extraordinary (n_e) and ordinary (n_o) refractive indices for MLC-6884 at 589nm and 656nm.

creases. Eq. (3.10) consists of a negative and a positive term. When the temperature is below T_c, the positive term can be smaller than the negative one, resulting in a negative $\frac{dn_o}{dT}$. As the temperature increases, the positive term also increases and jumps to a large positive number, therefore making $\frac{dn_o}{dT}$ positive. This effect can be observed in Fig. 3.3, with results concerning the LC MLC-6884.

3.3 Wavelength dependence of liquid crystal refractive indices

3.3.1 General equations

In order to describe the dispersion properties of LCs, the extended Cauchy Equation is used. The original Cauchy Equation was intended for isotropic liquids and gases, but it has been shown that it can be extended to include also anisotropic liquids [64]. The extended Cauchy Equation fits very well the experimental data [64] and can be written as

$$n_e = A_e + \frac{B_e}{\lambda^2} + \frac{C_e}{\lambda^4} \tag{3.11}$$

$$n_o = A_o + \frac{B_o}{\lambda^2} + \frac{C_o}{\lambda^4} \tag{3.12}$$

where $A_{e,o}$, $B_{e,o}$ and $C_{e,o}$ are three Cauchy's coefficients that can be determined by measuring the refractive indices of the LC material at three (or more) different wavelengths and by fitting the experimental data to Eq. (3.11) and Eq. (3.12). Afterwards, the refractive indices at any wavelengths can be extrapolated by using Eq. (3.11) and Eq. (3.12).

3.3.2 An example

Table 3.4 shows the Cauchy coefficients in the temperature range $15-30°C$ for the LC MLC-6684. The dispersion of MLC-6884 for two different tem-

$T[\circ C]$	A_e	B_e	C_e	A_o	B_o	C_o
15	1.5585	0.00696	0.00031	1.46412	0.00628	-0.00013
20	1.55521	0.00696	0.00032	1.44958	0.01537	-0.00166
25	1.55081	0.00792	0.00012	1.46104	0.00623	-0.00004
30	1.5462	0.00853	0.00003	1.45634	0.00844	-0.00039

Table 3.4: Cauchy's coefficients in the temperature range $15-30°C$ for MLC-6884.

peratures, $T = 15°C$ and $T = 30°C$ is illustrated in Fig. 3.4 together with the experimentally measured points.

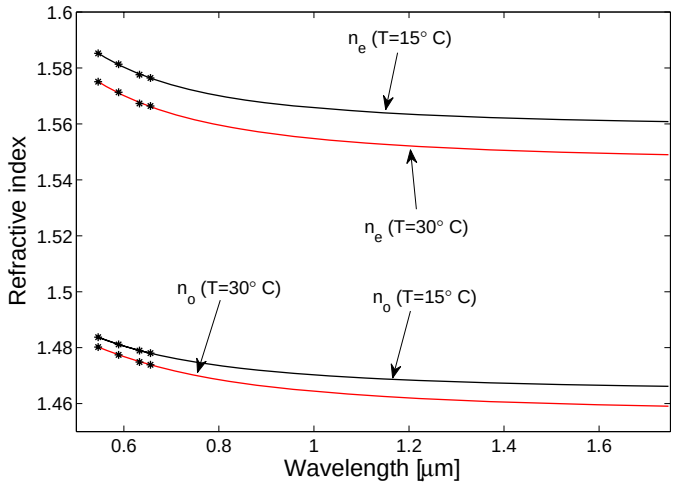

Figure 3.4: Dispersion of the extra-ordinary (n_e) and ordinary (n_o) refractive indices at $T = 15°C$ and $T = 30°C$.

3.4 Elastic properties

The molecular order of LCs has interesting consequences for the mechanical properties of these materials. LCs exhibit elastic behavior and any attempt to deform the uniform alignments of the directors and the layered structures (in case of smectics) results in an elastic restoring force. The constants of proportionality between deformation and restoring stresses are known as elastic constants. There are three basic elastic constants involved in the electro-optics of LCs depending on the molecular alignment in a given geometry: the splay (K_{11}), the twist (K_{22}), and the bend (K_{33}) [60]. For many LC compounds and mixtures, the magnitude of the elastic constants follows the order $K_{33} > K_{11} > K_{22}$ with typical values in the range of 3-25 pN. Fig. 3.5 illustrates the changes of shape of volume elements which can be described through the elastic constants K_{11}, K_{22} and K_{33}.

3.5 Dielectric properties

It is well known that LCs respond to electric fields. This is because the dielectric constants along the long molecular axis ($\varepsilon_{\|}$) and along any axes

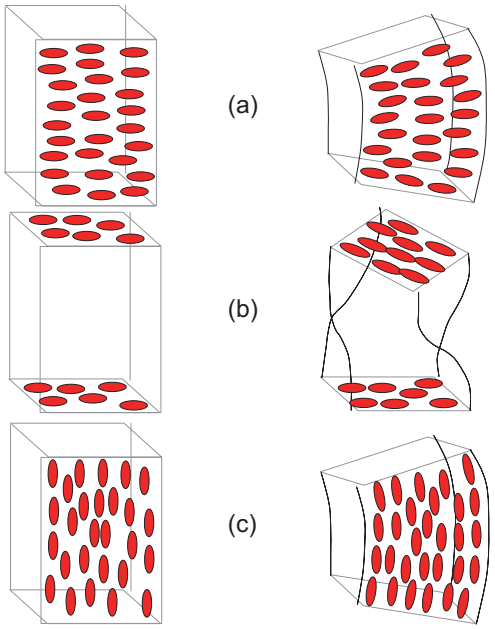

Figure 3.5: Meaning of the elastic constants: splay (a), twist (b) and bend (c).

perpendicular to it ($\varepsilon_\perp$) differ in value. $\Delta\varepsilon$, defined as $\varepsilon_\parallel - \varepsilon_\perp$, depends on the dipole moment μ strength and distribution θ with respect to the long molecular axis, temperature and applied frequency.

A dipole moment is induced by attaching polar groups, such as fluoro (F), cyano (CN) and isothiocyanato (NCS), to the phenyl ring that is normally present in LCs. Fig. 3.6(a) illustrates the positions in which polar groups can be attached. The dielectric anisotropy $\Delta\varepsilon$ is positive when the LC molecule, has an effective dipole at $\theta < 55°$ and is negative when the effective dipole is situated at $\theta > 55°$ [60]. If a molecule has two (or more) dipole moments (μ_1 and μ_2), its effective dipole can be calculated by the vector addition method illustrated in Fig. 3.6(b). In Fig. 3.6(b), one dipole is along the molecular axis and the second one is at an angle ϕ, with respect

to the molecular axis. The resultant dipole moment μ_r can be calculated as

$$\mu_r = \sqrt{\mu_1^2 + \mu_2^2 + 2\mu_1\mu_2 \cos\phi} \tag{3.13}$$

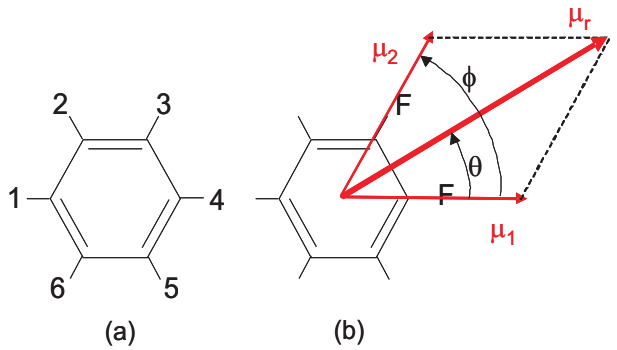

Figure 3.6: (a) Phenyl ring and possible positions of the polar groups, (b) Vector addition method for the calculation of the resultant dipole.

3.5.1 Positive $\Delta\varepsilon$

Nematic LCs with a positive $\Delta\varepsilon$ are the most common LCs, and among them, fluorinated compounds are the most used for Thin-Film-Transistor (TFT) Liquid Crystal Display (LCD) applications [65]. A typical fluorinated structure is shown in Fig. 3.7. The single fluoro compound has $\Delta\varepsilon \sim 5$ if F is attached to the phenyl ring in position 4, which provides a dipole along the principal molecular axis, as shown in Fig. 3.7. In order to further increase

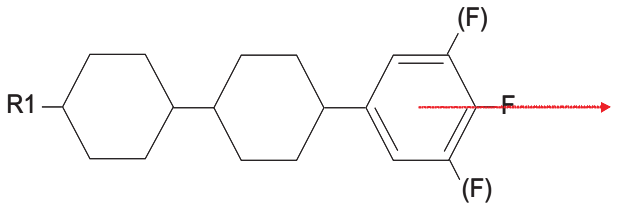

Figure 3.7: Chemical structure of a LC with a positive $\Delta\varepsilon$.

$\Delta\varepsilon$, more fluoro groups can be added in position 3 and 5 and the resultant

dipole will still be along the principal axis of the molecule. With 3 fluoro groups, a high $\Delta\varepsilon$ of around 10 is obtained. On the other hand, by adding more polar groups like F the molecule becomes bigger and, therefore, the moment of inertia increases. This causes the rotational viscosity to increase and, as it will be discussed later in this thesis, high viscosity makes LC devices slow to respond to an external electric field.

3.5.2 Negative $\Delta\varepsilon$

LCs with a negative dielectric anisotropy are used in glass cells with a vertical alignment configuration. Their typical application is in large size LCD TV panels and projection systems given that, in this configuration, the contrast ratio is much higher than any planar type of alignment. This is mainly due to an excellent dark state, which is typically observed for vertically aligned types of configuration. In order to exhibit a negative $\Delta\varepsilon$, molecules

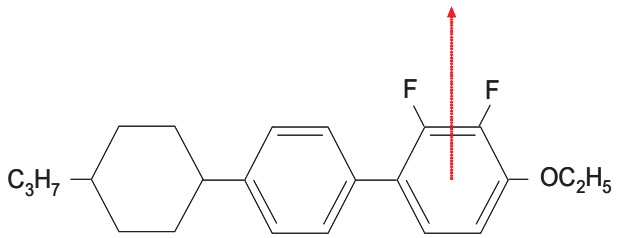

Figure 3.8: Chemical structure of a LC with a negative $\Delta\varepsilon$.

must have the dipole in perpendicular direction with respect to the principal molecular axis. The polar groups should, therefore, be attached in positions $(2, 3)$ of a phenyl ring. Again, the fluoro group is most frequently used, because of its high electronegativity and relatively low mass and atomic radius. Fig. 3.8 shows a typical negative $\Delta\varepsilon$ LC compound in which two lateral fluoro groups have been added. The estimated $\Delta\varepsilon$ is around -4. In order to increase $\Delta\varepsilon$, more fluoro groups can be attached but this, as for positive $\Delta\varepsilon$, increases the viscosity.

3.5.3 Dual-frequency liquid crystals

LC mixtures can be made such that they exhibit a property called dual-frequency. Dual-frequency LCs have a $\Delta\varepsilon$ which is positive at low

frequencies and negative at high frequencies. The frequency at which $\Delta\varepsilon = 0$ is called the crossover frequency. The major advantage in the use of these LCs is that, despite their high rotational viscosity, they exhibit a fast response time to applied electric field. Standard LCs have a faster rise time than decay time, but by driving the dual-frequency LC with an electric field at low frequency to switch it on and high frequency to switch it off, the decay can be made comparable with the rise time [66]. Dual-frequency LC mixtures are made of both positive and negative $\Delta\varepsilon$ compounds. Normally, the positive $\Delta\varepsilon$ compound is frequency dependent, with $\Delta\varepsilon$ decreasing as a function of frequency, while the negative $\Delta\varepsilon$ compound shows no frequency dependence. The resulting overall $\Delta\varepsilon$ of a dual-frequency LC is frequency dependent, with a crossover frequency. Fig. 3.9 shows $\varepsilon_{\parallel}$, $\varepsilon_{\perp}$ and $\Delta\varepsilon$ of a

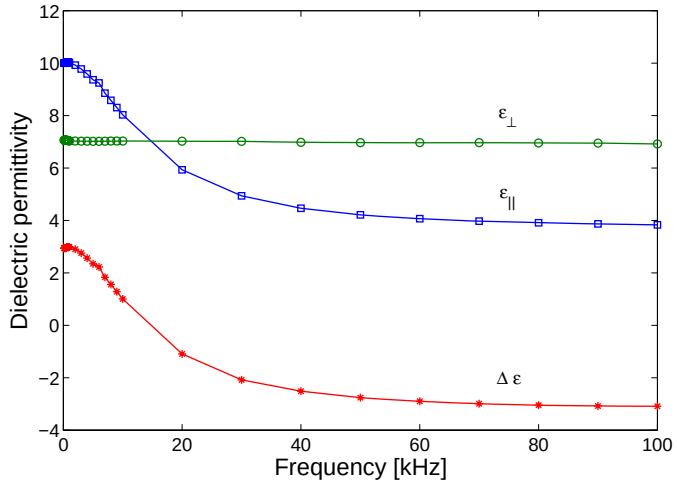

Figure 3.9: Frequency dependence of dielectric permittivities and dielectric anisotropy of a dual-frequency LC named MDA-00-3969 (or MLC-2048).

commercially available dual-frequency LC named MDA-00-3969 (or MLC 2048) from Merck. This LC will be used along this thesis for the fabrication of various LC devices.

The value of the LC dielectric constants affect the operation voltage and response time. In a cell with a planar alignment, for example, the

threshold voltage V_{th}, i.e. the voltage above which the LC starts to reorient, is related to the dielectric anisotropy ($\Delta\varepsilon = \varepsilon_{\parallel} - \varepsilon_{\perp}$) and the splay elastic constant K_{11} as [59]

$$V_{th} = \pi\sqrt{\frac{K_{11}}{\Delta\varepsilon}} \tag{3.14}$$

Therefore, a low threshold voltage can be achieved by having a material with a high $\Delta\varepsilon$.

Also the elastic constants affect the LCs performance. They affect primarily the threshold voltage and the response time. From the expression of the threshold voltage written above, one can note that a smaller K_{11} will result in a lower threshold voltage. However, the response time of LC devices is proportional to the visco-elastic coefficient $\frac{\gamma_1}{K_{ii}}$, where γ_1 is the rotational viscosity. Therefore, a small elastic constant is unfavorable from the point of view of the response time.

3.6 Elastic free-energy

The splay, the twist and the bend elastic constants are also present in the expression for the elastic free-energy density of a LC, which can be written as [53, 59]

$$F = \frac{K_{11}}{2}(\nabla \cdot \vec{n})^2 + \frac{K_{22}}{2}(\vec{n} \cdot \nabla \times \vec{n})^2 + \frac{K_{33}}{2}(\vec{n} \times \nabla \times \vec{n})^2 \tag{3.15}$$

The integral of the free-energy density F over the LC domain is the free-energy. This quantity is very important because the alignment of the LC can be determined by its minimization. As it will be explained in the next section, if an electric field is applied to the LC, another term is added to Eq. (3.15) and the total free-energy needs to be minimized again in order to find the new alignment induced by the application of the external field.

3.7 Electro-optic effect

If an electric field is applied to a LC it will exert a torque on the LC director, because the minimization of the free-energy contribution requires the LC to move. Depending on the sign of the dielectric anisotropy (i.e. depending wether $\varepsilon_{\parallel}$ is larger or smaller than $\varepsilon_{\perp}$), this torque will turn the director

respectively along or perpendicular to the field director.

As shown in Fig. 3.10(c) we can decompose the electric field E in two components: $E_{\|}$, parallel to the director $\vec{n}$ and $E_{\perp}$, perpendicular to the director $\vec{n}$. Thus, the displacement $\vec{D}$ is equal to

$$\begin{aligned} \vec{D} &= \varepsilon_{\|}\vec{E_{\|}} + \varepsilon_{\perp}\vec{E_{\perp}} = \\ &= \Delta\varepsilon\vec{E_{\|}} + \varepsilon_{\perp}\vec{E} \end{aligned} \tag{3.16}$$

With reference to Fig. 3.10(c) we can write $E_{\|} = (\vec{n} \cdot \vec{E})\vec{n}$.

Therefore

$$\vec{D} = \varepsilon_{\perp}\vec{E} + \Delta\varepsilon\vec{n}(\vec{n} \cdot \vec{E}) \tag{3.17}$$

When an external electric field is applied to the LC, this will contribute to

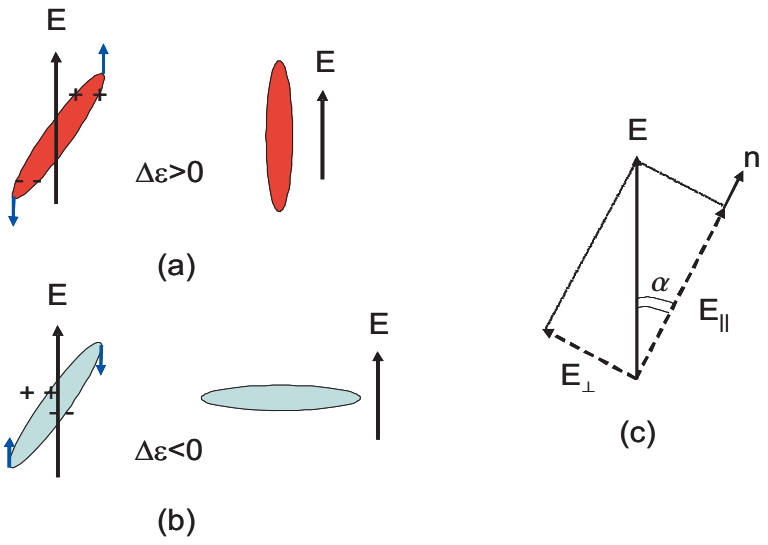

Figure 3.10: Depending on the sign of the dielectric permittivity, the LC director will tend to align parallel (a) or perpendicular (b) to the external electric field.

the free-energy density of the LC with the following term

$$F_\varepsilon = -\int_0^E \vec{D} \cdot d\vec{E} = \tag{3.18}$$

$$= -\frac{1}{2}\varepsilon_\perp E^2 - \frac{1}{2}\Delta\varepsilon(\vec{n} \cdot \vec{E})^2 \tag{3.19}$$

With α the angle between $\vec{E}$ and $\vec{n}$, the contribution to the free-energy density becomes

$$F_\varepsilon = -\frac{1}{2}\varepsilon_\perp E^2 - \frac{1}{2}\Delta\varepsilon E^2 \cos^2\alpha \tag{3.20}$$

The lowest energy state can be obtained by minimizing Eq. (3.20).

Therefore:

- if $\Delta\varepsilon > 0$, the minimum of the energy is when $\alpha = 0$ (director turned into the field direction)
- if $\Delta\varepsilon < 0$, the minimum of the energy is when $\alpha = \frac{\pi}{2}$ (director perpendicular to the field direction)

3.7.1 Rise time of liquid crystals (τ_{ON})

In order to obtain information about the dynamics of the LCs, i.e. rise time and decay time, all the forces determining the position of the LC need to be considered. In the case of the rise time, the dynamics is described by a balance between the dielectric torque and the viscous torque [59]. The dielectric torque is given by the negative derivative of the free-energy contribution with respect to α

$$\Gamma_\varepsilon = -\frac{\partial F_\varepsilon}{\partial\alpha} =$$

$$= -\Delta\varepsilon E^2 \cos\alpha \sin\alpha = \tag{3.21}$$

$$= -\frac{1}{2}\Delta\varepsilon E^2 \sin 2\alpha$$

The viscous torque Γ_v, always opposite in sign to the rate of change of the director, works against any change of the director field

$$\Gamma_v = -\gamma_1 \frac{\partial\alpha}{\partial t} \tag{3.22}$$

where, as before, γ_1 is the rotational viscosity of the LC (with a typical value is $0.1\frac{Ns}{m^2}$). Adding this torque Γ_v to Γ_ε, the equilibrium condition for small values of α can be written as [59]

$$\Delta\varepsilon E^2\alpha + \gamma_1\frac{\partial\alpha}{\partial t} = 0 \tag{3.23}$$

Therefore, α goes from its initial value α_0 to 0 according to

$$\alpha = \alpha_0 e^{\frac{-t}{\tau}} \tag{3.24}$$

where τ is the time constant of the system and corresponds to

$$\tau_{ON} = \frac{\gamma_1}{\Delta\varepsilon E^2} \tag{3.25}$$

3.7.2 Decay time of liquid crystals (τ_{OFF})

When the electric field is removed, the LC molecules will relax back to the previous position. In this case, the dynamics is described with a balance of the restoring elastic torque and the viscous torque [59]. The restoring torque Γ_r is the following [59]

$$\Gamma_r = -K\frac{\pi^2}{d^2}\alpha \tag{3.26}$$

where K is the elastic constant describing the deformation, d is the cell thickness and α the deformation angle. By solving $\Gamma_r + \Gamma_v = 0$, the expression for the decay time can be determined to be

$$\tau_{OFF} = \frac{\gamma_1 d^2}{K\pi^2} \tag{3.27}$$

3.7.3 Fredericks transition

The class of field instabilities called Fredericks transition is the most common effect LC devices are based on. By observing Eq. (3.21) which expresses the dielectric torque, one can note that two specific cases exist: $\alpha = 0$ and $\alpha = \frac{\pi}{2}$. If a LC with a positive $\Delta\varepsilon$ exhibits a planar alignment (also called *homogeneous*, Fig. 3.11(a)), then, when placed between two electrodes, the director will be perpendicular to the electric field ($\alpha = \frac{\pi}{2}$) and no dielectric torque will be exerted on the molecules. The same happens with a LC with a negative $\Delta\varepsilon$ that is vertically aligned (also called *homeotropic*, Fig. 3.11(b)). In this case $\alpha = 0$ and, again, no dielectric

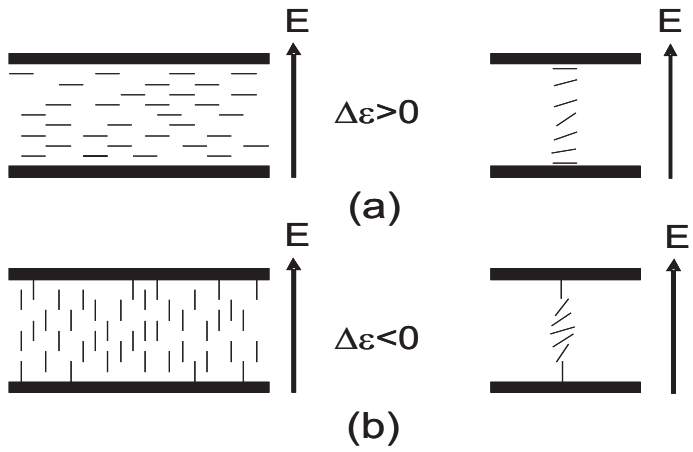

Figure 3.11: Deformation of the director caused by an electric field in a homogeneous (a) and homeotropic (b) case. The deflection is maximum in the middle of the cell and zero at the boundaries.

torque will realign the molecules. However, the orientational order is not perfect in a nematic LC since the forces that try to keep the molecules in one direction are strongly counteracted by thermal motion. For any fluctuation of the director out of the horizontal (homogeneous case) or vertical (homeotropic case) position, a dielectric torque will appear, trying to move the director, respectively, in a vertical or horizontal position. This torque is counteracted by an elastic torque trying to keep the molecules in their original position. When the electric field reaches a threshold such that the dielectric torque is higher than the elastic torque, the director will be reoriented toward being parallel (Fig. 3.11(a)) or perpendicular (Fig. 3.11(b)) to the direction of the electric field. This threshold is named Fredericks transition. As illustrated in Fig. 3.11, the director orientation does note change near the electrodes, since it is fixed by the boundary conditions on the electrode plates [52, 67].

By balancing the elastic free-energy density and the contribution to the free-energy density given by the electric field, one can obtain an expression for the Fredericks transition given by [59]

$$E_{th} = \frac{\pi}{d}\left(\frac{K}{\Delta\varepsilon}\right)^{1/2} \tag{3.28}$$

where d is the distance between the electrodes and K is the elastic constant describing the deformation. In both the homogeneous and the homeotropic cells the deformation is a mixture of splay and bend; however, just above the threshold, one can consider the deformation as pure splay ($K = K_{11}$) in the homogeneous case and as pure bend ($K = K_{33}$) in the homeotropic case [59], as illustrated in Fig. 3.12.

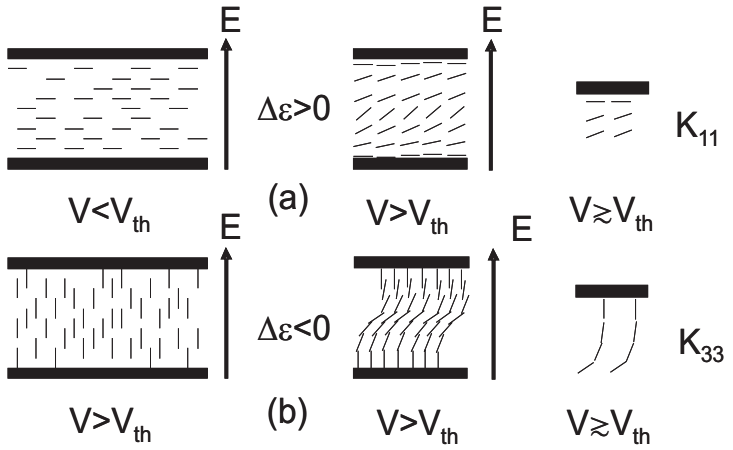

Figure 3.12: Homogeneous (a) and homeotropic (b) alignment. Just above the Fredericks threshold the elastic constant is pure bend (a) or pure splay (b).

3.8 Alignment of liquid crystals in silica capillaries

3.8.1 Polarization optical microscopy

A common way to determine the alignment of LCs is to use Polarized Optical Microscopy (POM) - a microscope technique that utilizes polarized light. This technique is not suitable for Photonic Crystal Fibers (PCFs) filled with LCs, because of scattering of the many capillaries present in the PCF. Instead, with this technique, the alignment of a single capillary can be determined very accurately. Therefore, capillaries of the same material (fused silica) and with approximately the same diameter as the capillaries in the PCF structure were used in order to investigate the alignment. The chosen capillary tube needs to be stripped using a lighter to flare off the coating and is then filled with LC. The experimental setup used for these measurements

is illustrated in Fig. 3.13. The sample is placed on a rotary turntable and illuminated from the bottom with unpolarized white light. The capillary sample is placed between two linear crossed polarizers, called respectively polarizer and analyzer. When no sample is present, no light (black color) is transmitted through the analyzer, because the direction of the analyzer is perpendicular to the polarizer. The same happens if the sample is isotropic. But, if the sample is birefringent (LC in its nematic state), the linearly polarized light after the polarizer can rotate while going through the sample and the component that is parallel to the analyzer can pass through. When this happens, other colors than black are observed. The colors are related to the optical path difference $\Delta n \cdot d$, where Δn is the optical birefringence of the sample and d the sample thickness, and to the angle between the crossed polarizers and the optical axis of the sample. By observing the colors after the analyzer, it is possible to determine the alignment of the LC. Normally, three pictures at three different angles $(0°, 22.5°, 45°)$ of the sample with respect to the polarizer are sufficient to determine the alignment.

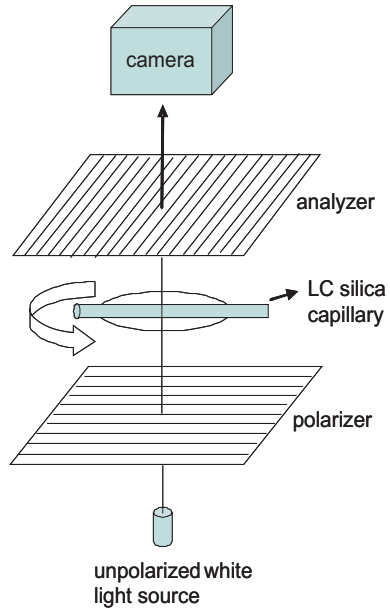

Figure 3.13: Schematic of a polarization optical microscope used for the investigation of alignment of LCs.

An example of the observed alignment at different angles is given in

Fig. 3.14(a),(b) and (c), which show the polarized micrograph of an LC with negative $\Delta\varepsilon$, named MLC-6884. This LC presents a splayed configuration, with an alignment at the surface of about 45° and with this angle opening up towards the opposite direction than the direction of filling. Fig. 3.14(d) explains how to determine the alignment by the analysis of the pictures. For the 0° micrograph, we see black in the middle of the capillary and bright around: this is because only the polarized light passing through the middle of the LC capillary keeps the linear polarization. By observing the 45° micrograph, now the molecules at the boundaries have the optical axis perpendicular or parallel to the polarizer and therefore the polarization is kept linear and no light goes through the analyzer. Therefore, the colors we see are black at the boundaries and bright in the center.

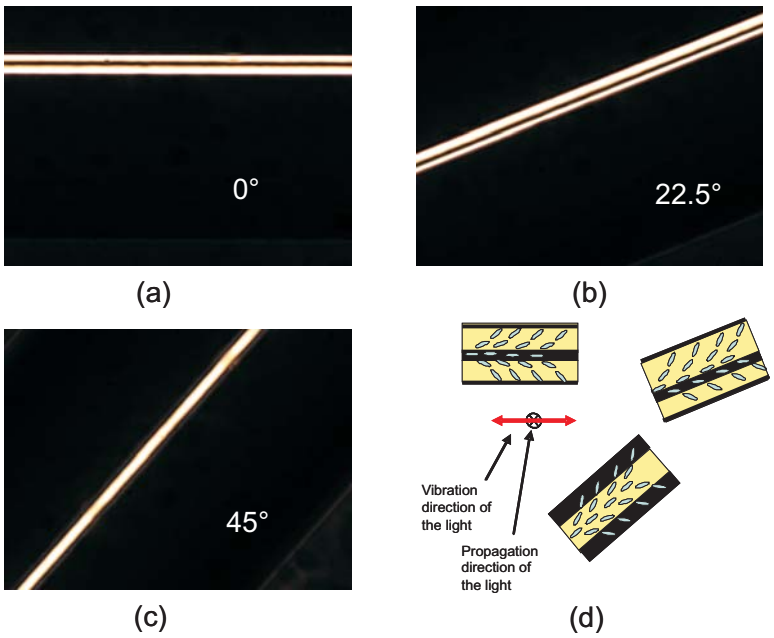

Figure 3.14: Polarization micrograph of a single silica capillary filled with MLC-6884 with an angle between capillary axis and polarizer of a) 0°, (b) 22.5° and (c) 45°. (d) Determination of the alignment.

3.8.2 Alignment study

The alignment of LCs is determined by many factors, such as smoothness, presence of defects and cleaning process of the glass substrate, surface tension of both LCs and glass, LC elastic constants, solid-LC contact angle, LC dielectric anisotropy, dipole and rigidity of the LC molecules [68]. In general, smooth layers of glasses orient the nematic director parallel to the substrate but do not induce an uniform and reproducible alignment. For these reasons, the glass surface is always coated with appropriate surfactants, which can give parallel, perpendicular or tilted alignments of the LC surface layer [68]. However, it was demonstrated that glass cylindrical cavities of dimension $2 - 6\mu m$ infiltrated with LCs present a good alignment without the use of coating and that, on the contrary, the presence of coating induces defects and local disorder in the alignment [69].

The alignment of all the LCs used in this thesis was determined in a $5\mu m$ silica capillary. Fig. 3.15 shows the alignment of LCs (in red) which were used in the fabrication of components in this thesis together with other LCs (in black) that were not used here. LCs with positive $\Delta\varepsilon$, such as E7 from Merck, MDA-00-1444 from Merck, UCF-1 (custom LC synthesized by Sebastian Gauza, University of Central Florida) and a single molecule LC (custom LC synthesized by Sebastian Gauza, University of Central Florida) presented planar alignment along the axis of the capillary. Negative $\Delta\varepsilon$ LCs, such as MLC-6884 from Merck and MLC-6608 from Merck presented a splayed alignment with, respectively, 45° and 90° at the boundaries. The dual-frequency LC named MDA-00-3969 from Merck had a splayed alignment with 45° at the boundaries. ZLI-3086 from Merck has $\Delta\varepsilon \approx 0$ and the alignment was 90° splayed in certain areas of the capillary and planar in others. The same happened for MLC-6682, but in this case the alignment alternated from being 45° splayed to be planar. The main difference between a splayed and a planar configuration is that, as discussed in section 3.7, planar aligned LCs present a Fredericks threshold, while splayed do not. Therefore, a LC device with a splayed aligned LC will respond to values of the electric field below the Fredericks threshold. Splayed aligned LCs are very good candidates for polarization controllers, because they reorient slowly with respect to the electric field amplitude, while planar LCs present a sudden change in the alignment, and therefore a different birefringence, as soon as the voltage is above the Fredericks threshold. Planar aligned LCs, on the other hand, are very good candidates for the fabrication of

polarimeters because, when the field is on, the director will orient towards the electric field and, therefore, one polarization experiences n_e, while the orthogonal one experiences n_o, leading to a high Polarization Extinction Ratio (PER). All these LC devices will be discussed in more detail in the next chapters.

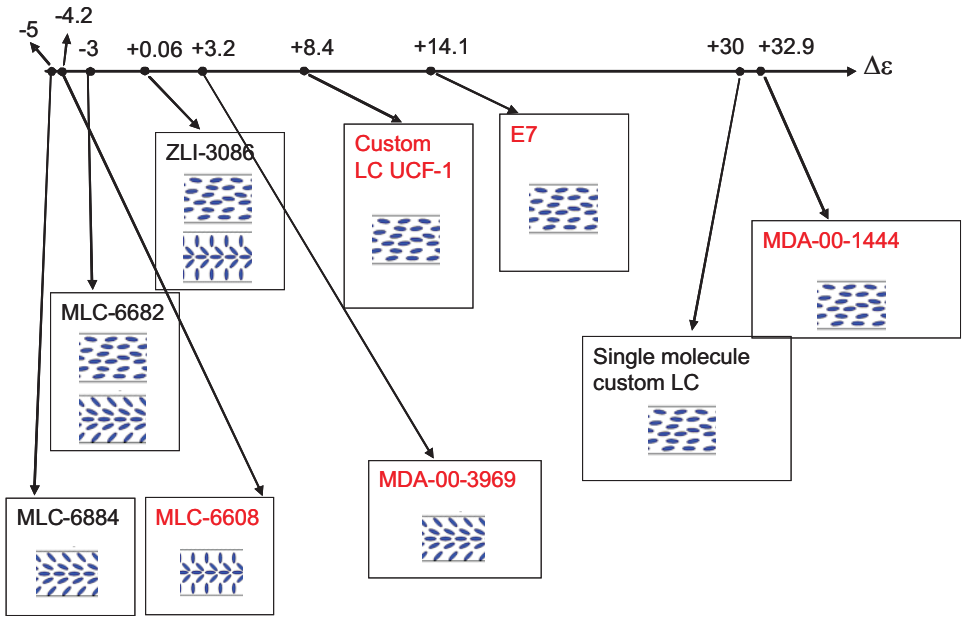

Figure 3.15: Alignment of various LCs in a $5\mu m$ capillary as a function of $\Delta\varepsilon$.

3.9 Summary

In this chapter, a brief introduction to the physical properties of LCs was given. An overview of various LC types and a description of the phases they may exhibit was provided. Dispersion, thermo-optical and electro-optical properties of LCs were discussed, together with the alignment that they exhibit in micro-size silica capillaries. In particular, a technique for the investigation of the alignment was presented and various LCs analyzed and compared.

Chapter 4

Liquid crystal photonic bandgap fibers

Liquid Crystal Photonic Bandgap (LCPBG) fiber devices represent a very interesting option for the fabrication of all-in-fiber tunable devices for tuning, scrambling and controlling, for example, attenuation, polarization or dispersion. Tunability of these devices can be achieved thermally [14, 15], electrically [16–18] or optically [19]. The advantage of using such devices is that they are small, compact and they can easily be coupled to fibers, therefore avoiding alignment issues. Furthermore, being based on fibers, they exhibit circular symmetry and, therefore, polarization sensitivity, such as Polarization Dependent Loss (PDL) and Polarization Mode Dispersion (PMD) can be reduced compared to planar-based components.

This chapter gives a description of the fabrication and characterization of an LCPBG fiber device. In section 4.1 the filling procedure of the fiber is described, in section 4.2 the setup for the measurement of the transmission spectrum is presented, and the transmission properties of a Large-Mode-Area (LMA)-13 fiber infiltrated with MDA-00-3969 are discussed. Section 4.3 presents thermal and electrical tunability of the device, while finite element simulations are discussed in section 4.4 and the simulated transmission is compared to the experimental results. Finally, section 4.5 presents the measured dynamics of an LCPBG fiber device. A short summary is given at the end of the chapter.

4.1 Filling procedure

Liquid Crystals (LCs) are infiltrated in Photonic Crystal Fibers (PCFs) by capillary forces. This method is very simple and it can be used if the filling length is short ($< 50mm$). A drop of LC is positioned on a clean glass plate and the tip of the PCF is dipped into the drop. Red light from a $635nm$ laser diode is coupled into the opposite end of the fiber, as shown in Fig. 4.1. The red light is scattered in the filled section, therefore indicating the length of the filling. LCs can also be infiltrated by using pressure or

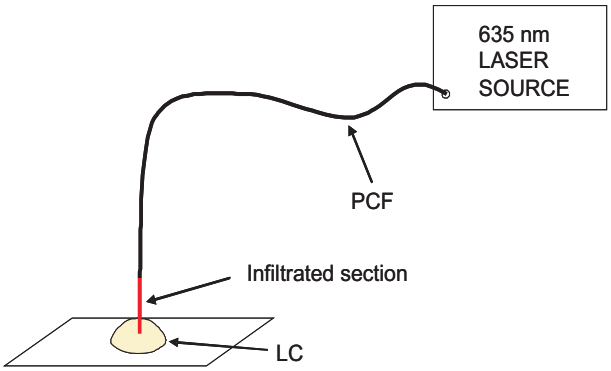

Figure 4.1: Schematic of the filling procedure. If the LC needs to be infiltrated at its isotropic temperature, the glass plate hosting the LC drop is positioned on a thermal plate.

vacuum. This requires that the fiber end, together with the clean glass and the LC drop, are placed inside a pressure or vacuum chamber. With this method the LC is pushed into the holes faster than with capillary forces and is therefore useful if a long section of PCF needs to be infiltrated or if the LC needs to be moved along the fiber. The major problem caused by this method is that, as the LC moves along the fiber, a thin layer is deposited at the wall of the capillaries of the fiber, therefore causing high scattering by the section in which the LC has passed. Also, pressure or vacuum filling can cause orientational defects in the LC, which introduce scattering points in the capillaries of the fiber [70] and, therefore, extra losses in the transmission spectrum of the LCPBG fiber device.

In this thesis, a filling technique based on capillary forces was used in order to minimize deformations of the LC alignment and because a filling

length less than $25mm$ was sufficient for our purposes.

4.1.1 Filling temperature

The temperature at which the LC is filled into the PCF is an important parameter since it affects the filling time but also the final alignment of the LC and the loss of the LCPBG fiber device. For nematic planar aligned LCs, such as E7 or MDA-00-1444, it was found that, in order to stabilize the alignment, the LC needs to be filled into the fiber at its isotropic phase, cooled down slowly and then heated again to the isotropic temperature and finally cooled down. This process provides low insertion losses of the device [19]. For nematic splayed aligned LCs, such as MDA-00-3969, MLC-6884 or MLC-6608, on the contrary, it was observed that the alignment was deteriorated if they were filled at isotropic temperature [18, 71] and that lower losses were reported if these LCs were infiltrated at room temperature.

4.1.2 Filling length versus filling time

When the end-facet of a PCF is immersed in a liquid, the liquid will contact the inside walls of the PCF capillaries. The contact angle θ is defined as the angle between the rim of the liquid that is inside the capillary and the capillary tube wall (see Fig. 4.2). This angle determines if the capillary forces will pull the liquid into ($\theta < 90°$) the capillary or push it out ($\theta > 90°$). A model for the calculation of the time necessary to fill the holes in a PCF has been developed for water and experimentally verified [72]. In this model four forces were considered to act on the water column inside the capillary tube: the capillary force, the friction force (related to the viscosity of the liquid), the force that arises from the application of an overhead pressure and the gravitational force. By solving a differential equation that takes all these forces into consideration, the filling length versus filling time was obtained and showed a decaying exponential behavior as function of time [72]. In the case of LCs, the contact angle is less than 90° and the LCs are pulled into the fiber by capillary forces. The filling length versus filling time was experimentally determined for two LCs, E7 (filled at the isotropic temperature) and MDA-00-3969 (filled at room temperature) infiltrated into an LMA-13 PCF with a hole size of $4.3\mu m$. Fig. 4.3 and Fig. 4.4 shows the filling length as a function of time (up to 3 hours) for these two LCs, by using capillary forces to push the LCs into the holes. The filling speed was higher for E7 since its viscosity was lowered by the fact that the LC was filled at

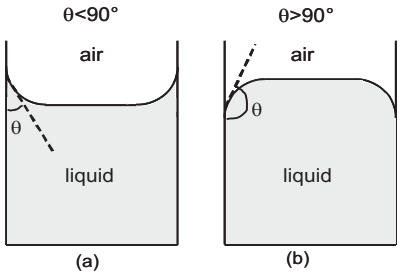

Figure 4.2: Contact angle of two different liquids in contact with a solid surface. (a) The capillary forces will pull the liquid into the capillary. (b) The capillary forces will push the liquid out of the capillary.

its isotropic phase. After 3 hours, the filling length was 11.2cm for E7 and 5.1cm for MDA-00-3969. The two experimental figures also show a decaying exponential behavior of the filling length as a function of time.

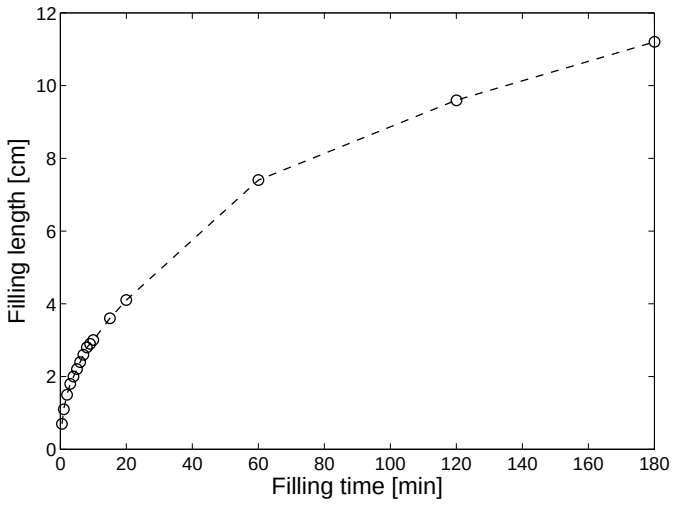

Figure 4.3: Filling length versus filling time for E7 infiltrated into an LMA-13.

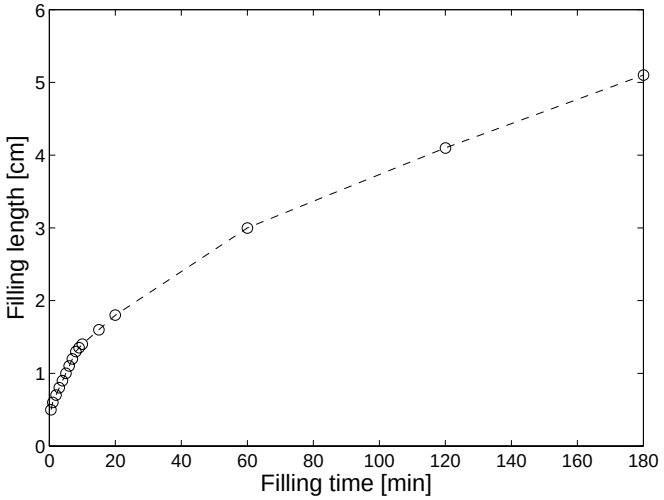

Figure 4.4: Filling length versus filling time for MDA-00-3969 infiltrated into an LMA-13.

4.2 Bandgaps of a liquid crystal photonic bandgap fiber

4.2.1 Setup

The setup shown in Fig. 4.5 is used throughout this thesis to characterize the transmission of LCPBG fiber devices and their tunability due to variation in temperature and applied electric fields. Light from a Halogen-Tungsten light source was coupled to a Single Mode Fiber (SMF), which was butt-coupled to the LCPBG fiber device using a xyz-translation stage. The section filled with LC was positioned on a thermal plate (Linkam MC60) with a temperature accuracy of 0.1°. The opposite end of the PCF was coupled into an optical spectrum analyzer set to a resolution of 10nm. The transmission spectrum was determined by normalizing the spectrum of the LCPBG fiber device to the spectrum of the unfilled fiber. The LCPBG fiber device was thermally coupled to the thermal plate through an aluminium block. In order to apply an electric field to the LCPBG fiber device, a metal bar was mounted on the top of the fiber and the voltage applied across the two metal bars (electrodes). Two uncoated sections of PCF were also placed between the

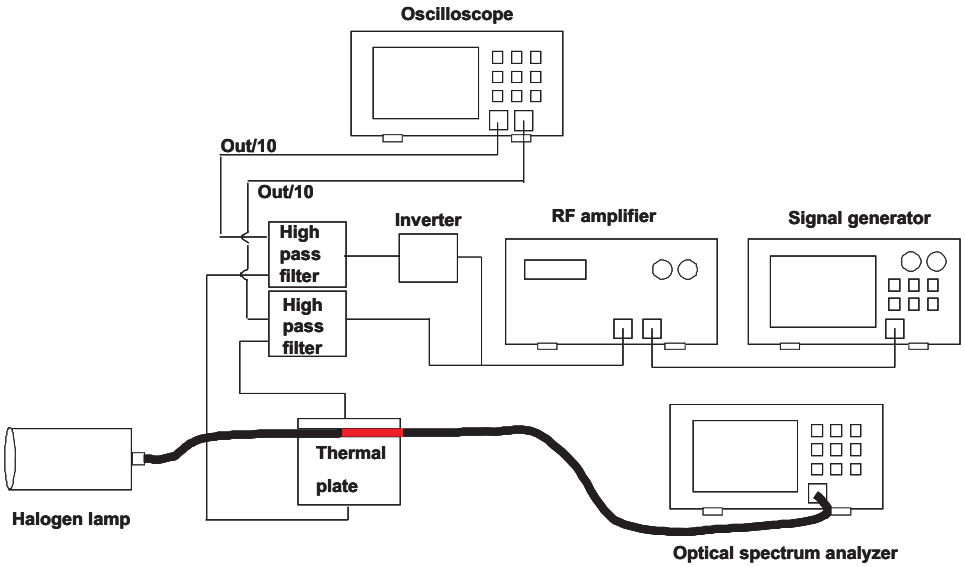

Figure 4.5: Schematic of the setup used to measure the transmission spectrum and to characterize the temperature and electrical tunability of the LCPBG fiber device.

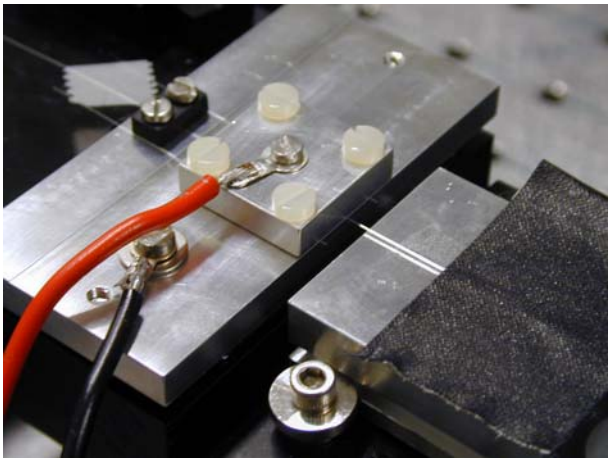

Figure 4.6: Photograph of the LCPBG fiber device positioned between the electrodes.

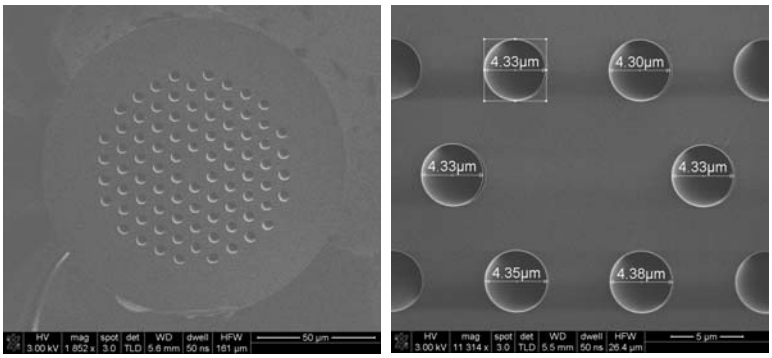

(a) Micrograph of LMA-13

(b) Micrograph of LMA-13, first ring

Figure 4.7: SEM of the end facet of LMA-13. The hole size d, inter-hole distance Λ and fiber outer diameter D are $4.3\mu m$, $8.5\mu m$ and $125\mu m$, respectively.

electrodes in order to control the spacing and three groves on the bottom electrode kept the three fibers in position. This part of the setup is shown in Fig. 4.6. The device was driven in bipolar mode by using two driving signals Vs, -Vs. The 1kHz sine wave driving voltage Vs was generated by a signal generator and amplified by using a high-voltage amplifier. The phase-shifted signal -Vs was generated by using an inverter. The DC components of Vs and -Vs were removed by two 80Hz high-pass filters in order to avoid impurity ion migration that could cause degradation of the electro-optical properties of the LC device [73].

4.2.2 Transmission spectrum and losses

By using the setup of Fig. 4.5 and the filling technique described above, the transmission spectrum of an LMA-13 fiber from Crystal Fibre A/S (hole size d=4.3μm, inter-hole distance Λ=8.5μm and outer diameter D=125μm) infiltrated with MDA-00-3969 was recorded. The filling length was $11mm$ and the spectrum was measured at room temperature. Two Scanning Electron Micrographs (SEMs) of the LMA-13 used in this experiment are shown in Fig. 4.7. The transmission spectrum is shown in Fig. 4.8, where bandgaps clearly appear. The extinction ratio between the maxima and the minima of the transmission is about 30 dB, which is promising for the use of these kinds of devices as optical filters. The insertion loss of the bandgap centered around 1550nm is 2dB. This loss is caused by different factors: scattering

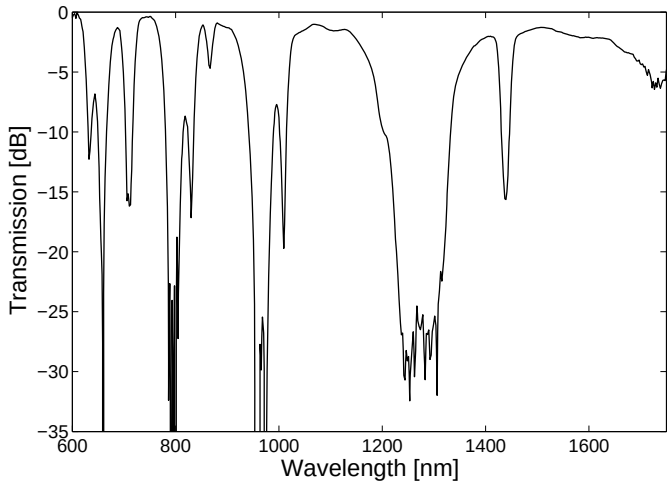

Figure 4.8: Transmission spectrum of a LMA-13 filled with MDA-00-3969.

and absorption from LCs and silica, coupling loss between the Total-Internal-Reflection (TIR) mode of the unfilled fiber and the Photonic BandGap (PBG) mode of the filled fiber, and propagation loss, caused by the fact that the structure is finite and therefore the guided mode may penetrate into the microstructured cladding and leak into the outer cladding region. However, absorption and scattering losses of LCs are much higher than those from silica, therefore the losses from silica can be neglected over the filling length. Furthermore, the LC scattering losses are much larger (two orders of magnitude) than the LC absorption losses and, therefore the absorption losses can be neglected [74]. Scattering losses were measured to be 15-40dB/cm in a LC bulk waveguide [74], but it was also shown that they can be drastically reduced (to 1-3 dB/cm) if the LC was confined in small capillaries with an inner diameter of $2 - 8\mu$m [70]. Since the field energy of the guided mode is mainly concentrated in the silica region of the infiltrated LMA, the scattering losses from the LC are further reduced. On short fiber pieces ($\sim$ 1cm) the propagation losses were shown to be insignificant compared with coupling losses [75] and, therefore, by comparing numerical results with experimental ones, it was found that the insertion losses of the infiltrated PCF were mainly determined by the coupling losses originated from a mismatch in mode profiles [21].

4.3 Tunability

4.3.1 Thermal tunability

The presence of bandgaps in the LCPBG spectrum suggests that the device can be used as a spectral filter, having both broad and narrow transmission windows. These windows can be shifted to other wavelengths by

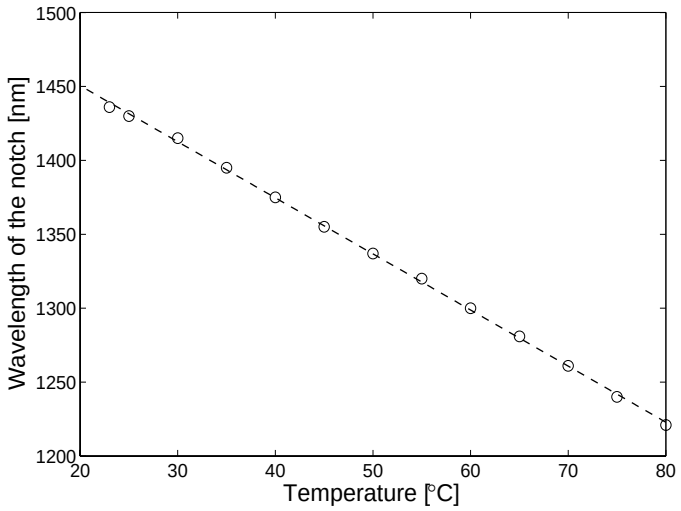

Figure 4.9: Temperature tuning of LMA-13 infiltrated with MDA-00-3969. The spectral position of the notch in the 1300-1800nm bandgap is plotted versus temperature. The notch moves $-3.6nm/°C$.

changing the temperature, therefore allowing the fabrication of tunable all-in-fibre spectral filters. Fig. 4.9 shows the tunability of LMA-13 filled with MDA-00-3969. The bandgaps move towards shorter wavelengths when the LC is heated up. The temperature tuning is linear, with a sensitivity of $-3.6nm/°C$ at infrared wavelengths. The linearity of the tunability comes from the fact that the refractive indices decrease linearly as a function of temperature. Fig. 4.10 shows the measured refractive indices for MDA-00-3969 at $\lambda = 565nm$ and in the temperature range $15 - 55°C$. The extraordinary refractive index decreases linearly as a function of increasing temperature, while the ordinary one is almost constant. The "average" LC refractive index is therefore deceasing and, from Eq. (2.2) it is easy to notice that a decrease

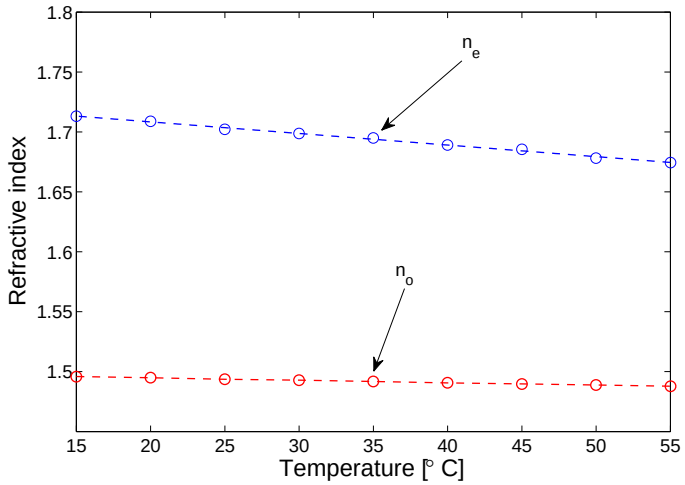

Figure 4.10: Temperature dependence of the extraordinary and ordinary refractive indices of MDA-00-3969 at $\lambda = 656nm$. The circles represent the measured data, the lines the fitted functions.

of the LC refractive indices leads to a shift of the bandgaps toward shorter wavelengths.

4.3.2 Electrical tunability

As discussed in chapter 3, the LC reorients when an electric field is applied and this causes the LC refractive indices to change. Therefore, tunability can also be obtained by applying an electric field to the LC. MDA-00-3969 belongs to a special class of so-called dual frequency LCs, as discusses in chapter 3. At low frequencies ($f < 15kHz$), $\varepsilon_{\parallel} > \varepsilon_{\perp}$ and, therefore, $\Delta\varepsilon$ is positive. At high frequencies, $\varepsilon_{\parallel} < \varepsilon_{\perp}$, giving a negative $\Delta\varepsilon$. If an electrical field is applied to a positive $\Delta\varepsilon$ LC, a dielectric torque will pull the director parallel to the field direction, as shown in Fig. 4.11(a). The MDA-00-3969 molecules will move for small voltage values since they are pre-tilted, except for the central molecules which will not be reoriented until the Frederick transition is reached. For negative $\Delta\varepsilon$ LC, the dielectric torque will pull the director perpendicular to the field, as shown in Fig. 4.11(b). In this case the MDA-00-3969 non-central molecules will reorient perpendicular to the field, while the central ones will not move because they are already perpendicular

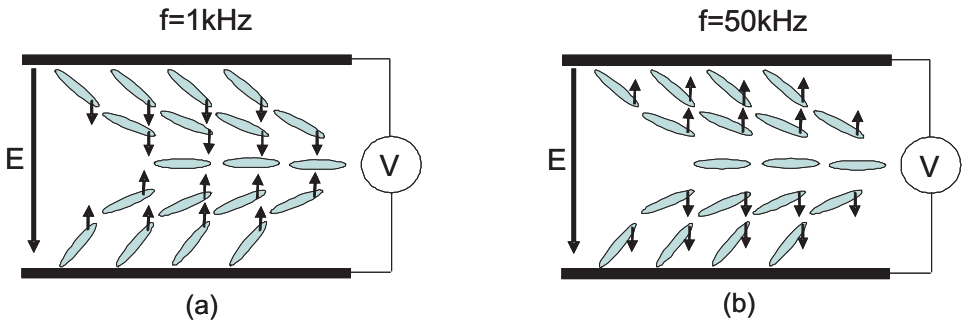

Figure 4.11: Schematic of the alignment and reorientation of MDA-00-3969 in a capillary when an electrical field with f=1kHz (a) or f=50kHz (b) is applied.

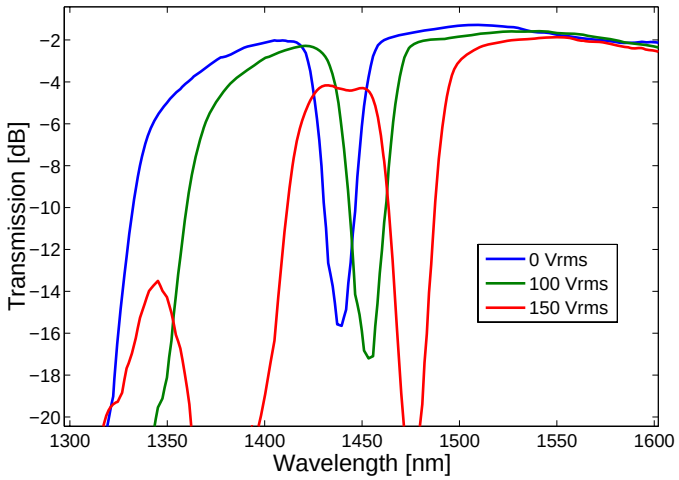

Figure 4.12: Transmission spectrum of LMA-13 filled with MDA-00-3969 in the range 1300-1600nm when a voltage of 0, 100 and 150V_{rms} is applied. The frequency of the applied electric field is 1kHz.

to the field. Applying a 1kHz field across the fiber causes the refractive index in the transverse plane to increase, which shift the bandgaps towards longer wavelengths (red shift). On the contrary, it was shown in [18] that if a 50kHz field was applied, then the refractive index in the transverse plane decreased, therefore causing a blue-shift of the bandgaps. Fig. 4.12 shows the electrical

tunability when 1kHz electric field was applied to the LCPBG fiber device. The bandgap shift at the short wavelength edge is 28nm with $100V_{rms}$ and 80nm with $150V_{rms}$. The spectrum was recorded at room temperature. The notch appearing in the transmission spectrum is caused by a cladding mode crossing a bandgap, forming a so-called "avoided-crossing" with the core mode of the bandgap [76]. This notch splits the whole bandgap into two parts.

4.4 Finite element simulations

Simulations based on a Finite Element Method (FEM) of LMA-13 infiltrated with MDA-00-3969 were carried out and the simulated transmission spectrum was compared to the experimental one [24]. It is, in fact, important to be able to simulate the LC alignment and the transmission spectrum of the LCPBG fiber devices, since the complexity of the problem makes analytical approaches to the problem difficult or even impossible. Moreover, a tool which can simulate LCPBG fiber devices can be very useful in the design phase. This tool has not been used to design devices throughout this thesis, since the tool was "up and running" when this thesis was almost finished.

The simulations consist of two different steps. First, the orientation of the LC in a capillary subject to an external applied field was calculated. Then, the orientation of the LC was transformed into a refractive index structure for all the capillaries in the fiber and the core mode of the biased LC infiltrated fiber, together with the coupling losses with respect to a PCF without LC, were calculated. Finally, the obtained simulated transmission spectra were compared to the experimental ones for three different voltages: $0V_{rms}$, $100V_{rms}$ and $150V_{rms}$.

The alignment of the LC under the application of an external electric field was obtained by solving the Partial Differential Equations (PDEs) that follow from minimizing the LC's free-energy [53] subject to some boundary conditions. Only two contributions were considered here, the

elastic free-energy and the electric free-energy

$$\begin{aligned} F[\vec{n}] &= F_0 + F_{el} = \\ &= \int_\Omega d\Omega \left(\frac{K_{11}}{2}(\nabla \cdot \vec{n})^2 + \frac{K_{22}}{2}(\vec{n} \cdot \nabla \times \vec{n})^2 + \frac{K_{33}}{2}(\vec{n} \times \nabla \times \vec{n})^2 \right) \\ &- \int_\Omega d\Omega \left(\frac{1}{2}\vec{D} \cdot \vec{E} \right) \end{aligned} \tag{4.1}$$

where the former term is the elastic free-energy, while the latter is the electric free-energy, with $\vec{D} = \overline{\overline{\varepsilon}}\vec{E}$. The use of only these two contributions corresponds to assuming fixed boundary conditions, which is reasonable for PCFs with relatively large capillaries with respect to the rod size of the LC [77]. A more stringent simulation would demand to add boundary terms in Eq. (4.1) [78].

Particular attention has to be paid to the electric field in Eq. (4.1). In fact, a change of the director structure, due to the application of an external electric field, causes a change of the dielectric structure, which in turn yields a new electric field distribution. Therefore, a coupled system of PDEs had to be considered, one for the minimization of the free-energy, and one with Poisson's equation

$$\nabla \cdot \vec{D} = -\nabla \cdot \overline{\overline{\varepsilon}} \nabla \Phi = 0 \tag{4.2}$$

where Φ is the electrostatic potential. The static dielectric tensor $\overline{\overline{\varepsilon}}$ can be written in terms of the director vector as

$$\varepsilon_{ij} = \varepsilon_\perp \delta_{ij} + \Delta\varepsilon n_i n_j \quad (i,j = 1,2,3) \tag{4.3}$$

where n_i is the i-th component of the director vector.

This complex system was solved with an iterative approach, illustrated in Fig. 4.13. First, the LC's free-energy was minimized without an applied electric field and the local director vector was determined for all the capillaries. The static dielectric tensor was calculated by using Eq. (4.3) and then used as a constant in Poisson's equation. From Poisson's equation the electric field $\vec{E}$ was obtained and then used as a constant in the free-energy F. The free-energy was then minimized again and the iterative process was continued until the change in the electric field from the previous to the next simulation was below a certain threshold. After

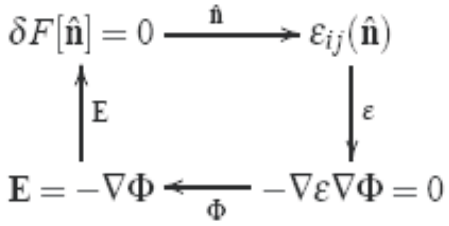

Figure 4.13: Iterative solution process for solving the system of coupled PDEs.

the determination of the LC alignment under the application of an external electric field, FEM simulations were carried out in order to determine the transmission spectrum. The dielectric permittivity tensor was calculated by using Eq. (4.3) and replacing $\varepsilon_\perp$ and $\varepsilon_\parallel$ with their optical equivalent $\varepsilon_o = n_o^2$ and $\varepsilon_e = n_e^2$. For the material dispersion, the Cauchy equations (Eq. (3.11) and Eq. (3.12)) were used, where the Cauchy coefficients $A_{e,o}$, $B_{e,o}$ and $C_{e,o}$ were extrapolated with the technique already discussed in chapter 3. The values of these coefficients at room temperature are listed in Table 4.1. For silica dispersion, the Sellmeier equation [79] was used. Then

A_e	B_e	C_e	A_o	B_o	C_o
1.6681	0.01116	0.00192	1.47935	0.00513	0.00042

Table 4.1: Cauchy's coefficients for MDA-00-3969 at room temperature.

the geometry was constructed and the dielectric structure was assigned. The whole structure was then put on a grid, which had a small element size for the fiber core and the capillaries and a more coarse mesh elsewhere. The FEM system matrices were based on second order vector elements and the domain was truncated using Perfect Matching Layers (PML) boundary conditions.

The FEM code was used to solve the generalized eigenvalue equation deriving from Maxwells equations, and the transmission spectrum for wavelengths between 1200 and 1500nm was simulated by calculating the coupling losses from the interfaces between empty and LC-filled sections of the PCF, equivalent to the experimental situation where an LC infiltrated PCF was coupled to a PCF without LC. The obtained transmission spectra

for 0V, 100V and 150V applied voltage are shown in Fig. 4.14. While in the experiments an AC electric field was used, a DC field was used in the FEM simulations in order to keep RAM consumption and computational time low. This is a reasonable approximation since the values of the elastic and dielectric constants of the LC at 1kHz are very close to the ones for a static electric field. The relevant AC-voltage for the comparison is then the root mean square (rms). With a voltage of 100V and 150V, bandgap shifts of 36nm and 94nm at the short bandgap edge were obtained, respectively. The short wavelength bandgap edge is at 1240nm, 1276nm and 1334nm for the 0V, 100V and 150V, respectively. These values were, therefore, compared with the ones obtained experimentally and shown in Fig. 4.12. The bandgap shift is 28nm for $100V_{rms}$ and 80nm for $150V_{rms}$ at the short

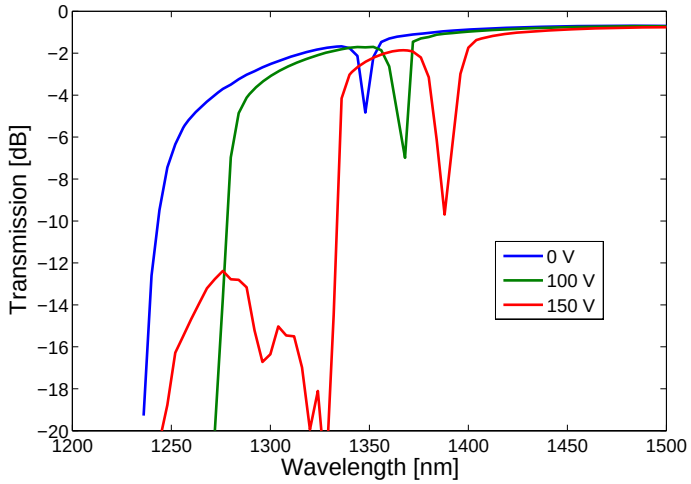

Figure 4.14: Simulated transmission spectrum of LMA-13 filled with MDA-00-3969 in the range 1300-1600nm when a voltage of 0, 100 and 150V is applied.

wavelength edge. The short wavelength bandgap edge is at 1330nm in the unbiased case and at 1358nm and 1410nm for $100V_{rms}$ and $150V_{rms}$ respectively. All these data referring to simulation and experimental spectra were measured at -12dB transmission. It can be noticed that the width and the depth of the notch in the experimental spectrum are larger than the ones observed in the simulated spectrum. This is believed to be caused by a slightly varying hole size of the experimental fiber with respect to the ideal

simulated one, supporting more modes in the capillaries and resulting in a wider wavelength range for which the core mode couples to the cladding modes. Nevertheless, the simulated bandgap shift, the bandgap width and transmission shape are in quite good agreement with the experimental ones. The simulated transmission spectrum is shifted about 100nm with respect to the experimental case. This can be attributed to small variations of the PCF hole size caused by the fabrication process and by the fact that the refractive indices of MDA-00-3969 in the infrared are extrapolated from measurements carried out in the visible.

4.5 Dynamics

When an electric field is applied to an LCPBG fiber device, the LC responds with a rise time that can be calculated by balancing the dielectric torque and the viscous torque. The rise time was expressed in Eq. (3.25). When

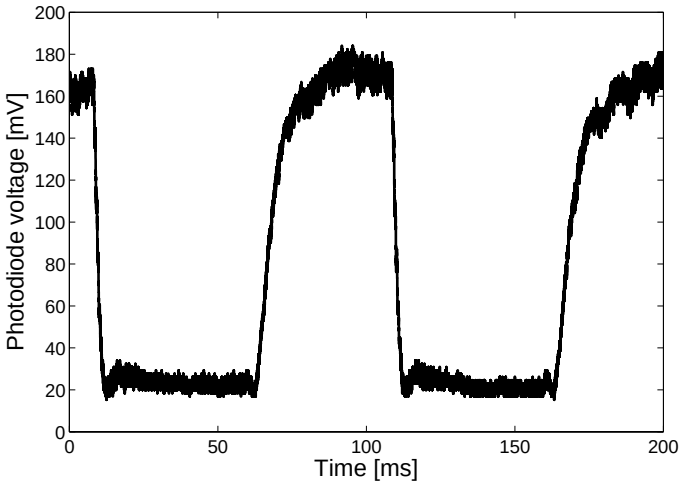

Figure 4.15: Photodiode voltage when a 1kHz sine wave with a $96V_{rms}$ voltage and amplitude modulated by a 10Hz square signal is applied to the electrodes of the LCPBG device.

the applied voltage is removed, the LCs molecules relax back to the previous alignment. In this case, the dynamics is described with a balance of the restoring elastic torque and the viscous torque. The decay time was given

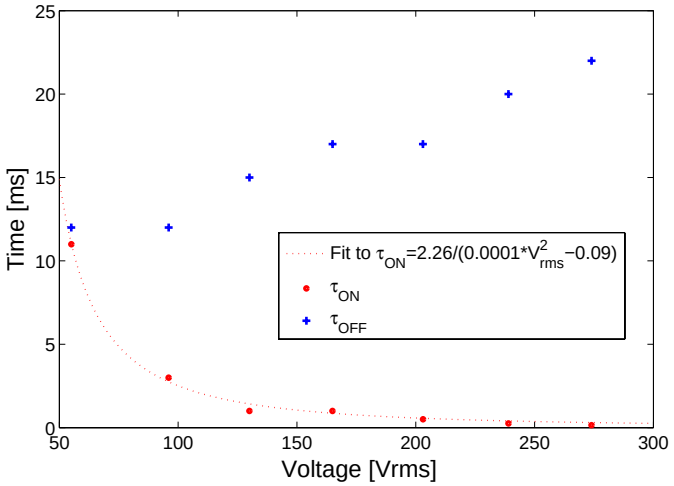

Figure 4.16: Measured response times, τ_{ON} and τ_{OFF} as function of the applied voltage. The fit to (3.25) is also shown.

in Eq. (3.27).

The dynamic properties of an LMA-15 (d=5μm, Λ=10μm and D=125μm) filled with MDA-00-3969 were investigated in [18] as a function of the applied voltage by coupling polarized light at 1551nm into the LCPBG fiber device. The chosen wavelength was located on the short-wavelength edge of the bandgap which was centered around 1600nm. This was done in order to have maximum sensitivity to the shift caused by an applied electric field. For measuring the dynamics, a 1kHz sine wave was amplitude modulated with a 50% duty-cycle 10Hz square wave signal and applied to the electrodes. When the electric field was off, there was high transmission at 1551nm. When the electric field was on, the bandgaps shifted towards longer wavelengths and low transmission was detected at 1551 nm. A photodiode was used to detect the intensity of the light at the output of the LCPBG fiber device and an oscilloscope displayed the photodiode voltage. Fig. 4.15 shows the amplitude modulation of the polarized light at 1551nm.

The rise and decay time τ_{ON} and τ_{OFF} were measured, respectively, from 90% to 10% and from 10% to 90% amplitude modulation and they are

shown in Fig. 4.16 as function of the applied voltage. As one can observe, the response time is limited by the decay time when the electric field is removed from the device. The decay time is expected to be reduced and comparable with the rise time by using a frequency modulation scheme, which switches between 1kHz and 50kHz. In this way, a dielectric torque would assist the LC molecules back into equilibrium, effectively reducing the decay time.

4.6 Summary

In this chapter a detailed description of the fabrication and characterization of an LCPBG fiber device was given. Techniques for infiltrating LCs into PCFs were discussed and the PCF filling length versus filling time by using capillary forces was measured for two LCs. The transmission spectrum of an LCPBG fiber device was obtained and its thermal and electrical tunability presented. FEM simulations were carried out and the simulated transmission spectrum was compared to the experimental results. Finally, the dynamics of a similar device was measured.

Chapter 5

Gaussian filters with LCPBG and oil-based PBG fibers

In this chapter filters with Gaussian spectral response realized using Liquid Crystal Photonic Bandgap (LCPBG) fibers are described. This kind of filters is becoming more and more important as they can find application in Optical Coherence Tomography (OCT), which is a high-resolution ($1 - 15\mu m$) optical imaging technique [80]. In the past two decades, OCT has been established as an adjunct noninvasive diagnostic technique for a variety of medical fields. It has been widely used to probe the eyes and other biological tissues and, in the last few years, the high-resolution achieved has allowed even cellular and subcellular imaging [80, 81]. An OCT system is based on an interferometer illuminated by a broad band light source. The shape and width of the emission spectrum of this light source are important variables because of their influence on the sensitivity of the interferometer. In particular, the broad band source is required to have a broad spectrum (100-300nm) and should possess a shape that is as close as possible to a Gaussian [80–83]. For ophtalmic images, the optimal wavelengths to use are around 800nm, while for tissues, 1300nm illumination is preferred [81]. Many different sources have been used, for example, mode-locked $Ti : Al_2O_3$ and Cr^{4+} :forsterite lasers [81], femtosecond mode-locked lasers [83] and supercontinuum sources [84, 85]. Wavelength-Division Multiplexing (WDM) couplers [84] or programmable spectral processors [86] can be used to shape the output spectrum of these sources in order to obtain a Gaussian profile. These devices are not wavelength-tunable; furthermore, couplers are delicate to handle and spectral processors are expensive and bulky.

Here a new alternative to the fabrication of Gaussian filters is proposed by using tapered Photonic Crystal Fibers (PCFs) filled with Liquid Crystals (LCs) or oils. Gaussian filters centered around 1300nm and 1000nm are presented, with a tunability of more than 100nm. These filters open up the possibility to be integrated in an OCT system, allowing for the optimization of the system because of their shape and tunability.

The following chapter discusses the fabrication techniques of Gaussian filters and compares the various filters achieved. This is supported by simulations using a Beam Propagation Method (BPM) code. Section 5.1 explains the working principle behind the realization of these filters and in section 5.2 a criterion for the adiabaticity of tapers is presented. In section 5.3 the fabrication process is discussed more in detail, with a focus on the equipment used for making tapers. Sections 5.4 and 5.5 present filters achieved by using LCs, while section 5.6 presents a filter fabricated by using oils. Finally, in section 5.7 a comparison among the filters in terms of central wavelength, bandwidth, losses, tunability and deviation with respect to a Gaussian function is presented. A short summary is given at the end of the chapter.

5.1 Working principle

Tapering an LCPBG fiber gives a further degree of freedom in the fabrication of LC all-in-fiber devices. In fact, it allows to shape the transmission spectrum and to eliminate undesired bandgaps.

A schematic of a tapered LCPBG fiber is illustrated in Fig. 5.1. The taper is fabricated and, afterwards, infiltrated with LC. The working principle for the fabrication of Gaussian filters is the following. Along the down-taper section, the PCF hole diameter decreases and, therefore, the cut-offs of the LC modes in the capillaries shift towards shorter wavelengths and so does the transmission spectrum. If the LC is also infiltrated inside the capillaries of the up-taper section, the bandgaps will move back to their original position since the hole diameter increases along the up-taper region. The central part of the resulting transmission spectrum corresponds to the transmission that is in common to the untapered section and the tapered section at the waist. The edges of the resulting spectrum will be

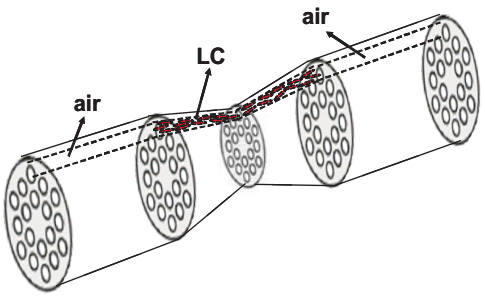

Figure 5.1: Schematic of a tapered LCPBG fiber. All the capillaries along the tapered section are infiltrated with LC.

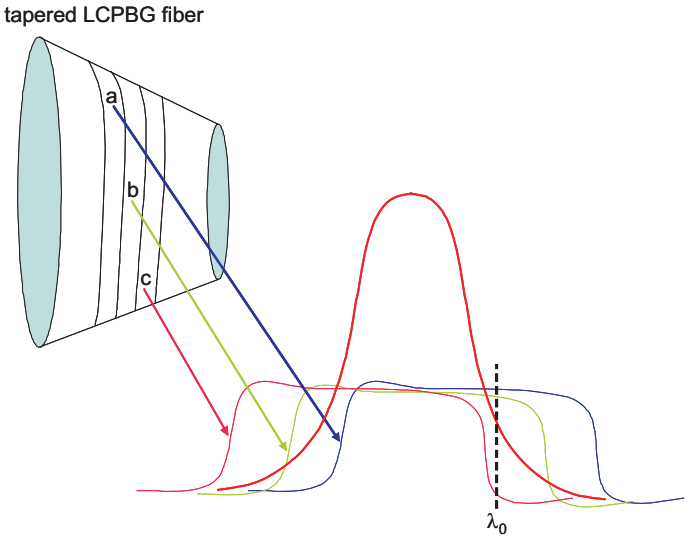

Figure 5.2: Working principle behind the fabrication of an LCPBG fiber-based Gaussian filter. Each section gives rise to different bandgaps (with colors blue, green and pink in the above figure), slightly shifted one respect to the other. The final spectrum (red) results from the overlap of these different spectra and coupling along the taper of the core mode with cladding modes.

smoothed since coupling between the core mode and the cladding modes occurs along the taper section.

In other words, the fiber structure scales continuously along the down-taper and each infinitesimal decrease of the hole size leads to an infinitesimal blue-shift of the LC modes bands intersecting the silica line, as one can observe from Eq. (2.2). The coupling between the core mode and the cladding modes along the taper is not as strong as for an untapered filled-fiber, since the wavelengths at which it happens vary continuously along the taper. If the taper is divided into small sections, as illustrated in Fig. 5.2, each section will give rise to different bandgaps. The bandgaps of the following sections along the down-taper are slightly blue-shifted with respect to the previous ones. For example, light at the wavelength λ_0 is guided in section b, but not in section c. Nevertheless, the power at this wavelength will not be completely suppressed in the final transmission spectrum (red curve in Fig. 5.2) since the coupling is weak as the wavelengths at which it happens vary continuously along the taper. This phenomenon causes the resulting transmission spectrum to be smoothed at the edges and to assume a shape close to Gaussian.

5.2 Adiabaticity criterion

An important issue concerning tapers is adibaticity. Tapering of a Single Mode Fiber (SMF) can lead to loss of power from the fundamental mode because of the departure of the longitudinal invariance of the fiber. If, while propagating along the taper, the electromagnetic field is unable to change its distribution rapidly enough to keep up with the variation of the fundamental local mode, coupling of the fundamental mode with cladding modes occurs. Power is lost from the fundamental mode and the taper becomes lossy. Therefore, a taper is considered to be approximately adiabatic if the taper angle is small enough everywhere to ensure that there is negligible loss of power from the fundamental core mode as it propagates along the taper [87].

In order to have adiabaticity, the following relation has to be fulfilled

$$\Omega(z) = \tan^{-1}\left|\frac{d\rho}{dz}\right| \approx \left|\frac{d\rho}{dz}\right| \leq \frac{\rho(\beta_1 - \beta_2)}{2\pi} \tag{5.1}$$

where Ω is the local taper angle, illustrated in Fig. 5.3 and $\rho{=}\rho(z)$ is the local core radius. β_1 is the propagation constant of the fundamental mode and β_2 is the propagation constant of the higher order mode with a propagation constant closest to that of the fundamental mode. The same

criterion holds for PCFs, provided that the PCF cross-sectional structure is preserved when tapered [88–91]. In this case β_2 is substituted with β_{FSM}, where FSM stands for Fundamental Space-Filling Mode (FSM). The FSM mode of a PCF is defined as the mode with the largest effective index of the infinite two-dimensional photonic crystal that constitutes the PCF cladding [92]. For a PCF with $\frac{d}{\Lambda} = 0.4$, $\Lambda = 7\mu m$ and $n_{SiO_2} = 1.445$, the

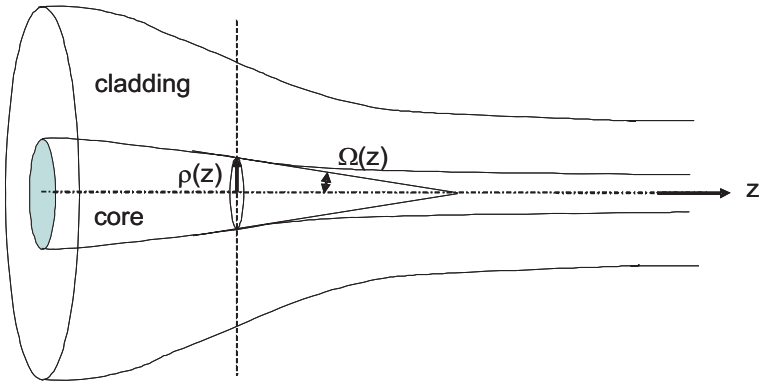

Figure 5.3: Schematic of a tapered SMF.

effective indices of the core mode and the FSM at $1.5\mu m$ are 1.443 and 1.439, respectively [46]. Let us consider a PCF with an outer diameter of $125\mu m$ and a core size of $10\mu m$ tapered down to $100\mu m$. The core size at the taper waist is $8\mu m$. In order to calculate the adiabaticity criterion, the taper profile $\rho(z)$ should be known and β_1 and β_2 should be calculated along the taper. In our specific case, the exact taper shape is not known with accuracy and the lowest taper ratio of the fabricated tapers is $100\mu m/125\mu m = 0.8$. If we assume that the propagation constants of the core and the cladding modes will not change drastically along the taper (that is reasonable because the taper ratio is high), then we can substitute the values of the taper in Eq. (5.1) and have a rough estimate for the adiabaticity condition for our specific case, that is $\mid \frac{d\rho}{dz} \mid \leq 10\mu m/mm$. This is not rigorous, since β_1 and β_2 should be recalculated along the taper profile, but accurate simulations were not considered to be necessary since the taper ratio is very high and, therefore, it does not represent a threat for adiabaticity.

Throughout this thesis, during the fabrication of PCF tapers, the criterion $\mid \frac{d\rho}{dz} \mid \leq 10\mu m/mm$ is always respected.

5.3 Fabrication process

Normally a fiber is tapered by heating a portion of it to its softening point and applying a tensile force. As the fiber elongates, its cross sectional area is reduced accordingly. Various tapering techniques have been developed, which include brushing flames [40], CO_2 lasers [93], and sapphire pieces for temperature stabilization [94, 95], leading to low-loss ($< 0.1dB/mm$) tapers with submicron dimensions [94, 96]. For PCFs, the cross-sectional structure needs to be preserved along the taper, i.e. the hole size and the inter-hole distance have to be scaled proportionally to the outer diameter. If the heating and pulling parameters provide insufficient tension in the axial direction of the fiber, surface tension dominates the flow dynamics and the material flows in the transverse direction, causing a collapse of the air-holes. However, this can be avoided by using a "fast and cold" technique [96], which consist of using maximal tension (which does not break the fiber) together with minimum heat (sufficient to make the glass flowing).

All the PCF tapers realized throughout this thesis were fabricated by using a Vytran LDS-1250 tapering station. A picture of this machine is shown in Fig. 5.4. Two mobile holding blocks hold the fiber in place. They move in opposite directions, with the same speed, or in the same direction, but with different speeds, in order to apply tension to the fiber. In between these stages, a furnace provides the heat necessary to soften the fiber. The furnace consists of an Omega-shaped iridium filament, capable of achieving the necessary temperature required to soften silica fibers.

The fiber was placed inside the Omega grove of the filament, such that the heat was distributed homogeneously. Argon gas flowed in the furnace in order to avoid breaking the filament, to keep the fibers clean and to dispel the heat. The "fast and cold" technique was used with this machine. The temperature of the filament was chosen to be just enough to soften the fiber and the tension was chosen to be maximum, being careful not to break the fiber. The machine was equipped with a taper macro generator that automatically generated the macro code for the fabrication of the taper. A taper macro generator window allowed the user to enter the desired characteristics of the taper, i.e. final diameter, down taper length, up taper length etc., together with the fabrication parameters, i.e. maximum power of the filament, gas flow, constant pull velocity etc. After

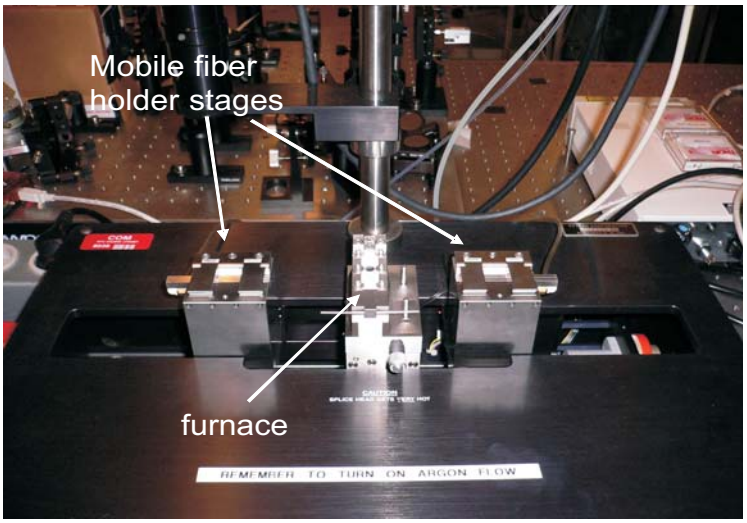

Figure 5.4: Picture of the Vytran LDS-1250 used for the fabrication of PCF tapers.

the fabrication of the taper, the diameter of the taper waist and the length of the taper were always measured with the help of a microscope in order to have a further verification.

Many problems have been encountered during the first year of use of this machine: high loss of the tapers (1-10dB), no repeatability and macro-bending along the taper (visible with the naked eye), with consequent oscillations in the transmission spectrum of the tapered fiber. The reason was that the motors were not aligned, pulling the fiber in two slightly different directions with respect to the axis of the fiber, and therefore causing bending of the fiber and loss. The first two Gaussian filters described in this chapter were fabricated when the machine was misaligned and, in fact, they showed a loss of 1-2dB. Later, the tapering station was aligned with the help of Vytran staff and tapers with an insertion loss of 0-0.02dB were fabricated. All the filters presented in the last section of this chapter were fabricated when the machine was aligned and, therefore, their insertion loss was substantially reduced.

5.4 First liquid crystal Gaussian filter without tunability

The first Gaussian filter was fabricated by using a Large-Mode-Area (LMA)-10 fiber from Crystal Fibre A/S filled with E7. This LMA fiber has a hole diameter of $3.3\mu m$, inter-hole distance of $7.2\mu m$ and outer diameter of $125\mu m$. The ordinary and extraordinary refractive indices of the LC used are $n_o = 1.52$ and $n_e = 1.75$, respectively, both measured at $589.3nm$ and $T = 20°C$. The alignment was planar, with the director parallel to the fiber axis. The PCF was tapered down to $100\mu m$ and the total length of the taper was 14mm. The LC was infiltrated along the whole length of the taper (down- and up-taper sections).

Fig. 5.5 shows the transmission spectrum of the untapered LMA-10 filled with E7. If the LC infiltrated section is tapered before the infiltration, the transmission shown in Fig. 5.5 can be modified and the bandgaps can be shaped. In fact, the PCF structure scales down along the down

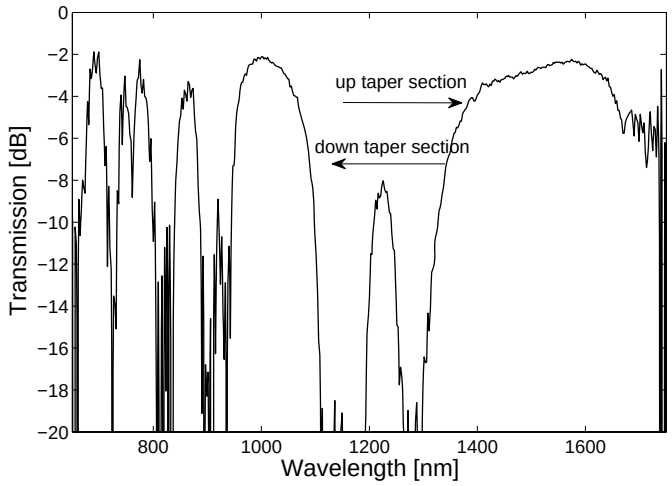

Figure 5.5: Transmission spectrum obtained at room temperature by filling 10 mm of an untapered LMA-10 with E7. The bandgaps shift towards shorter wavelengths along the down taper length and they return to the previous position along the up taper length.

taper section and, therefore, the bandgaps move towards shorter wavelengths. They move back to their original position along the up taper length.

An estimated shift of 200nm was calculated in order to delete almost all the higher order bandgaps and have a Gaussian filter around 1400nm. A small residual of the bandgap in the range 900-1130nm was expected to appear. A bigger shift was required to completely eliminate it, but this would have increased the loss of the spectrum. Eq. (2.2) was again used for the estimation of the hole size at the taper waist and, therefore, for the estimation of the taper waist itself. A shift of 200nm was estimated to occur with a taper waist of $100\mu m$. The wavelengths which are within the infrared bandgap of both the tapered and the untapered filled-LMA propagate through the taper, without being subjected to any extra loss in addition to the already known losses (coupling, scattering and absorption losses from the LC, propagation loss etc.). The wavelengths close to the bandgap edge experience losses caused by the coupling of the core mode with cladding modes, as explained in section 5.1. Therefore the bandgap in the range 1300-1800nm is expected to change its wavelength range and its shape and the higher order bandgaps are expected to disappear. The peak of the new spectrum is expected to shift about 100nm with respect to the central wavelength of the bandgap of the untapered fiber.

In order to measure the transmission spectrum of the tapered LMA filled with E7, the infiltrated section was butt-coupled to a 1 meter long LMA-10. White light was coupled to one end and collected to the other end by using an optical spectrum analyzer. Fig. 5.6 shows the measured transmission spectrum, normalized to the spectrum of the untapered fiber, in the range 700-1700nm and in linear units, together with the Gaussian that best fits the experimental data. The transmission has a Gaussian shape and its peak is around 1400nm and it is 100nm shifted with respect to the central wavelength of the bandgap of the untapered fiber, as expected. The higher order bandgaps are completely removed by the taper, except a residual of the bandgap in the range 900-1130nm, also expected by the theory. This residual bandgap can be observed in Fig. 5.6 at 910nm.

The 3dB-bandwidth of the filter is 180nm. The amplitude, mean and standard deviation of the Gaussian fitting function are 0.2265, 1388nm and 67.42, respectively. The loss is high: 6 dB. A way to reduce the loss is to

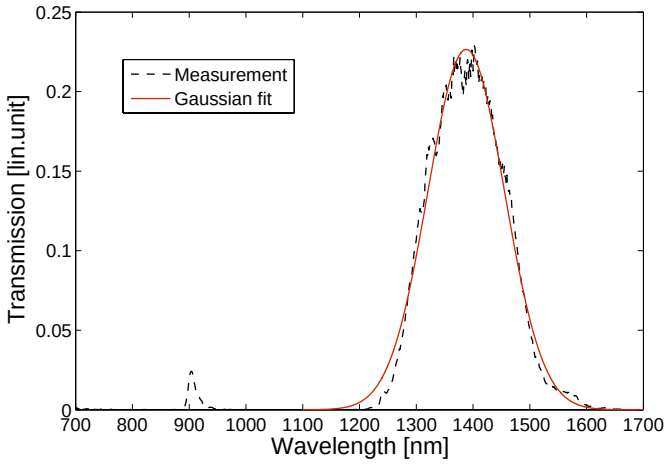

Figure 5.6: Measured transmission spectrum at room temperature of a tapered LMA-10 filled with E7. The amplitude of the Gaussian fit is 0.22, the mean value is 1388nm and the standard deviation is 67.42nm.

fill a shorter section and to improve the tapering process.

The tunability was also measured by increasing the temperature, but a very small, insignificant tunability was observed. This is because the LC E7 does not present a particularly broad tunability. Other LCs can be used to improve the thermal tunability.

5.5 Tunable liquid crystal Gaussian filter

The fiber used in this experiment is an LMA-10 fiber from Crystal Fibre A/S with a hole diameter of $2.9\mu m$, inter-hole distance of $6.6\mu m$ and outer diameter of $125\mu m$. A Scanning Electron Micrograph (SEM) of this fiber is shown in the inset of Fig. 5.7. The fiber was tapered down and then up again to an outer diameter of $115\mu m$, as illustrated in Fig. 5.7. The total length of the tapered region was 14mm. In order to diminish the losses caused by the LC, only the down tapered section was infiltrated with a nematic LC called MDA-00-1444. A visual inspection technique was used in order to infiltrate the desired section of the fiber. Later, it was observed that

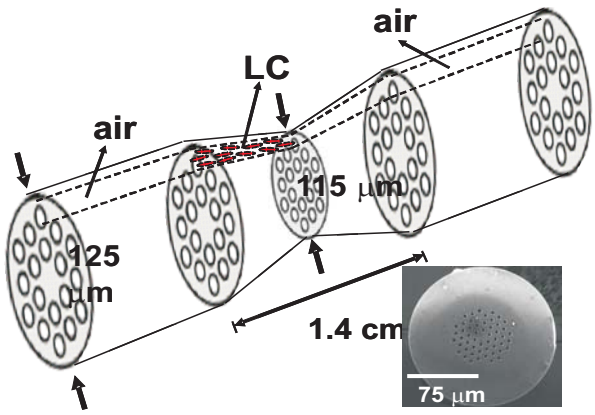

Figure 5.7: Schematic illustration of the tapered LCPBG fiber. Only half of the tapered section is filled. Inset: SEM of the end facet of the LMA-10 used in the experiment. The hole size d, inter-hole distance Λ and fiber outer diameter D are $2.9\mu m$, $6.6\mu m$ and $125\mu m$, respectively.

this configuration was not stable, since the capillary forces dragged the LC in the middle of the taper, such that the LC was symmetrically distributed around the taper waist. The ordinary and extraordinary refractive indices of this LC are $n_o = 1.5070$ and $n_e = 1.6844$, respectively, both measured at $589.3nm$ and $T = 20°C$. The alignment of the LC was planar, with the director parallel to the fiber axis. Eq. (2.2) was again useful in order to estimate the desired hole size at the taper waist and, therefore, to estimate the taper waist itself. A taper waist of $115\mu m$ was calculated to be optimal. In fact, if the fiber was tapered down to less that $110\mu m$, the bandgap shift would have been too large and the resulting Gaussian filter lossy. A taper of $100\mu m$ was fabricated and filled with this LC and a loss of 8dB was measured.

Fig. 5.8 shows the transmission spectrum of the untapered LMA-10 filled for 9mm with MDA-00-1444. The working principle is analogous to the previously explained one: if the fiber is tapered and then infiltrated, the bandgaps will move towards shorter wavelengths along the down taper length and coupling of the core mode to the cladding modes will occur and introduce a smoothing of the transmission spectrum, giving rise to a Gaussian-like spectrum.

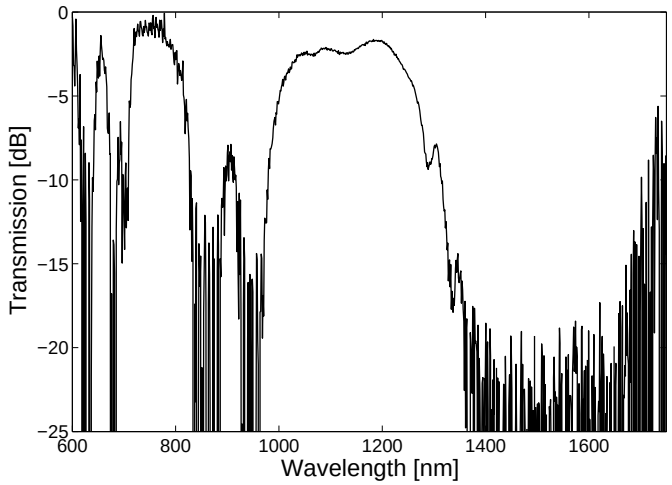

Figure 5.8: Transmission spectrum measured at $30°C$ obtained by filling 9 mm of an untapered LMA-10 with MDA-00-1444.

The taper was fabricated and the LC infiltrated for a length of 8mm. White light was coupled to one end of the device and the transmission spectrum was recorded by using an optical spectrum analyzer. Fig. 5.9 shows the measured transmission spectrum in linear units, normalized to the spectrum of the tapered unfilled fiber. The central wavelength of the resulting Gaussian-like spectrum is 1062nm, shifted about 90nm with respect to the central wavelength of the bandgap of the untapered fiber of Fig. 5.8. The device has a 3dB-bandwidth of 150nm. The amplitude, mean and standard deviation of the Gaussian fitting are 0.49, 1062nm and 62.25nm, respectively. The filter could have been made narrower by using a smaller taper waist, but this would have led to higher losses. The insertion loss is 4dB; 3dB caused by the LC and 1dB from the taper. The loss from the taper is shown to be reduced in the next section by aligning the tapering station.

In order to measure the temperature tunability, the taper section was placed on a hotplate controlled by a temperature controller LINKAM MC-60. The spectrum was recorded as the temperature was increased from $30°C$ to $80°C$ in steps of $10°C$. The spectrum shifted towards shorter

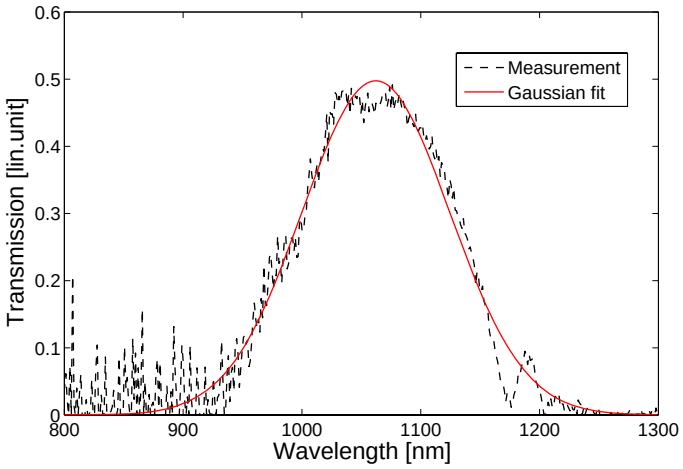

Figure 5.9: Measured transmission spectrum at $30°C$ of the tapered LMA-10 filled with MDA-00-1444. The amplitude of the Gaussian fit is 0.49, the mean value is 1062nm and the standard deviation is 62.25nm.

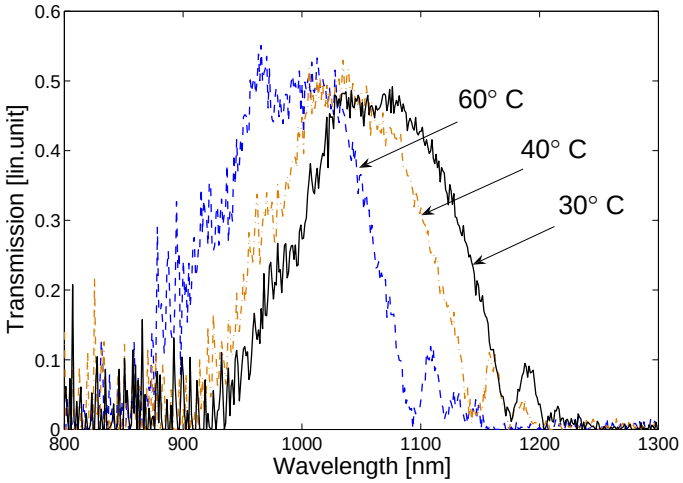

Figure 5.10: Tapered LMA-10 with MDA-00-1444 at various temperature.

wavelengths by increasing the LC temperature. In particular, by increasing the temperature from $30°C$ to $80°C$, a shift of 110nm was observed. The Gaussian shape was preserved for temperatures varying between $30°C$ and $60°C$, while a deviation from the Gaussian shape was observed at $70°C$ and $80°C$, caused by a change of the transmission spectrum from its original shape since the LC was close to its isotropic temperature ($98.5°C$). Fig. 5.10 shows the temperature tuning of the Gaussian filter at $30°C$, $40°C$ and $60°C$.

5.6 Tunable oil-based Gaussian filter

Gaussian filters infiltrated with isotropic oils were also fabricated and compared with the LC-based Gaussian filters. This study is interesting because it allows one to investigate if losses can be reduced and if a good degree of tunability can be reached with the use of oils. Moreover, a vectorial BPM code developed by the University of Bologna, Italy was available. This code, based on a finite difference algorithm with Padè approximation and Perfect Matching Layers (PML) absorbing boundary conditions, can simulate the evolution of all the field components along a taper, provided that the propagation medium is isotropic [97]. It allows one to compare the transmission spectrum of an oil-filled PCF with the correspondent simulated one.

The oil used was from Cargille Laboratory (Cedar Grove, NJ, USA) and had a refractive index of 1.53920 measured at 589.3nm and $25°C$. Its thermal gradient was -0.000393dn/dT in the range $15 - 35°C$. This oil was chosen among many others available because its refractive index was very close to the ordinary refractive index of the LC E7 ($n_o = 1.52$ measured at $589.3nm$ and $T = 20°C$) and it, therefore, allowed a direct comparison between the properties of the LC-filled fiber and the oil-filled fiber. The fiber used in this experiment was an LMA-10 fiber with a hole diameter of $2.9\mu m$, an inter-hole distance of $6.6\mu m$ and an outer diameter of $125\mu m$. The diameter of the taper waist was $107\mu m$, the down-taper section was 0.35mm long, the straight central part was 6mm long and the up-taper was again 0.35mm, as illustrated in Fig. 5.11. The taper respected the adiabaticity criterion. The taper was infiltrated with oil for 1cm.

The transmission spectrum was measured by coupling white light into

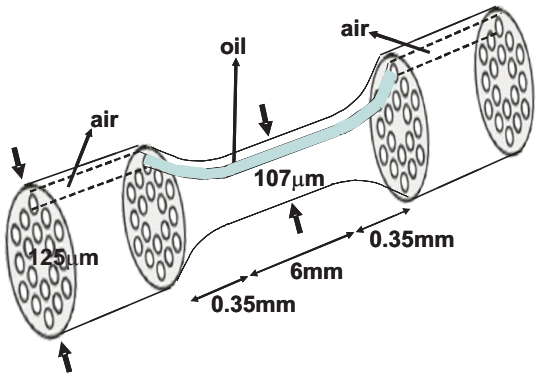

Figure 5.11: Schematic illustration of the tapered PCF fiber infiltrated with a oil with a refractive index of 1.53920 from Cargille Laboratory.

one PCF end, butt-coupling the other end with a SMF and collecting the light with an optical spectrum analyzer. The spectrum was Gaussian, but ripples were observed. These ripples were caused by coupling of the core mode with lossy cladding modes, which were not attenuated because the PCF was uncoated and, therefore, coupled back to the core mode. This problem can be solved by coating the tapered fiber, such that these cladding modes are attenuated in the coating. The adopted solution is illustrated in Fig. 5.12. A silica ferrule, i.e. a silica cylinder with a cylindrical cavity of $126\mu m$ in the middle, such that two fibers can be inserted into it, was used. The tapered PCF and SMF were positioned inside the cavity. The butt-coupling loss was 0.2-0.3dB. A few drops of UV curable polymer were poured on the ferrule and the polymer was cured with UV-light, to provide mechanical stability. In this way, besides providing a coating to the fiber, the ferrule held the PCF and SMF together. The transmission spectrum was measured by coupling white light to one end of the device and collecting it with an optical spectrum analyzer. The obtained spectrum is shown in Fig. 5.13. The shape was Gaussian, the insertion loss was 0.5dB and the 3-dB bandwidth 250nm. The amplitude, mean and standard deviation of the Gaussian fitting function were 0.94, 1361nm and 101.81nm, respectively.

The thermal tunability of this filter was measured by positioning the filter on a hotplate controlled by a temperature controller LINKAM MC-60. The transmission spectrum was measured from $25°C$ to $100°C$, in steps of

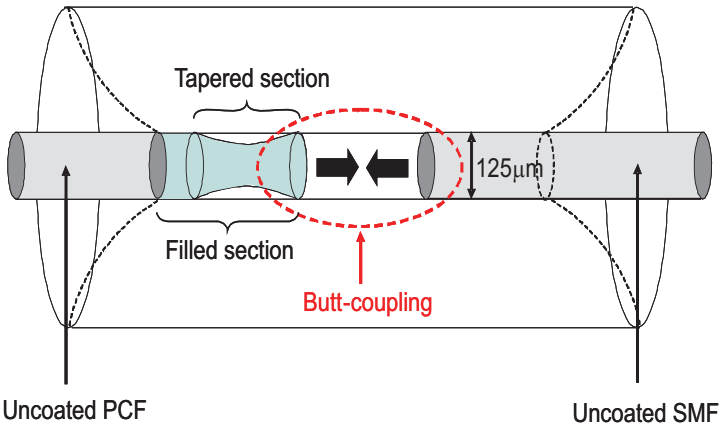

Figure 5.12: Illustration of the mechanical splice of the oil infiltrated PCF with the SMF. UV curable polymer is positioned on top and cured in order to give mechanical stability to the device.

$5°C$. A blue-shift of 210nm was observed by increasing the temperature in this range. A deviation from the Gaussian shape was noticed for temperatures above $60°C$. However, in the range $25°C$ to $60°C$, the central wavelength shift was 117nm.

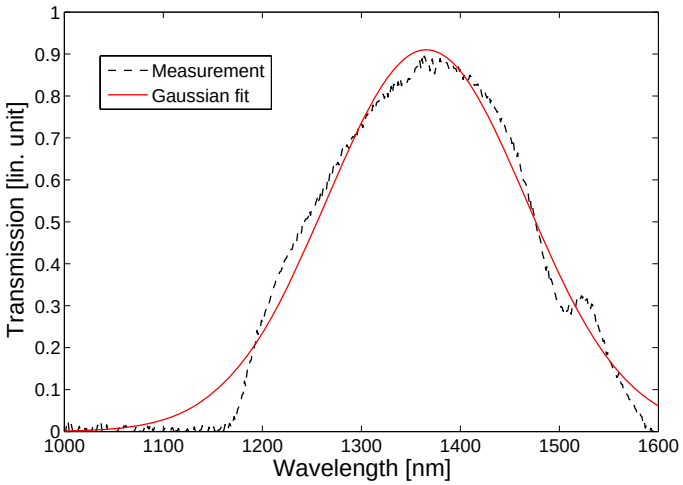

Figure 5.13: Measured transmission spectrum at $25°C$ of the tapered LMA-10 filled with oil. The amplitude of the Gaussian fit is 0.94, the mean value is 1361nm and the standard deviation is 101.81nm.

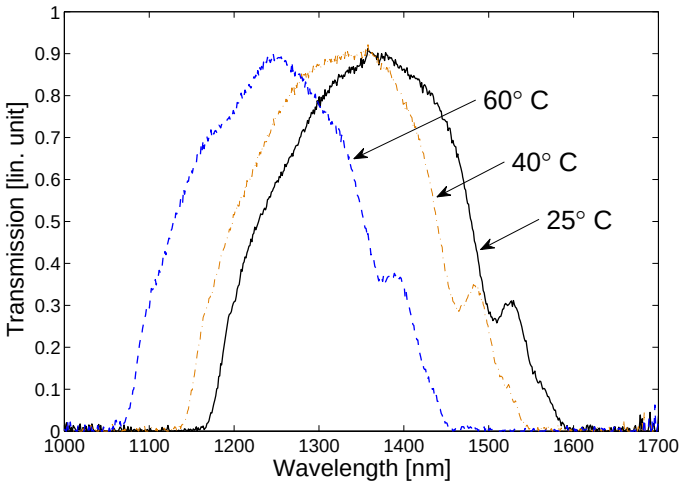

Figure 5.14: Thermal tunability of the tapered LMA-10 filled with oil. Transmission spectra at $25°C$, $40°C$ and $60°C$ are shown.

5.6.1 Beam Propagation Method simulations

Simulations of the oil-filled tapered PCF were carried out with a vectorial BPM code developed by the University of Bologna, Italy. This code can simulate the propagation of a field along a tapered isotropic Photonic BandGap (PBG) fiber. Considering that the taper shape cannot be exactly known, for the simplicity of the code setup, the taper shape was assumed to be linear. The refractive index of the oil at $25°C$ was calculated in the wavelength range 1000-1600nm through the Cauchy parameters given by the producer of the oil (Cargille). The wavelength dependence of the silica substrate was considered by using the Sellmeier equation [79]. The discretization step was chosen to be 25nm. About 4 hours per wavelength were necessary to draw the figure shown later on, running the code on standard PC. A Gaussian field with a power of 10W was used to excite the PCF. The simulated PCF taper was the same as the one described in this section: diameter of the taper waist $107\mu m$, down-taper length 0.35mm long, central part 6mm long and up-taper length 0.35mm long. The simulated transmission spectrum is shown in Fig. 5.15. If compared with Fig. 5.13, it can be observed that the

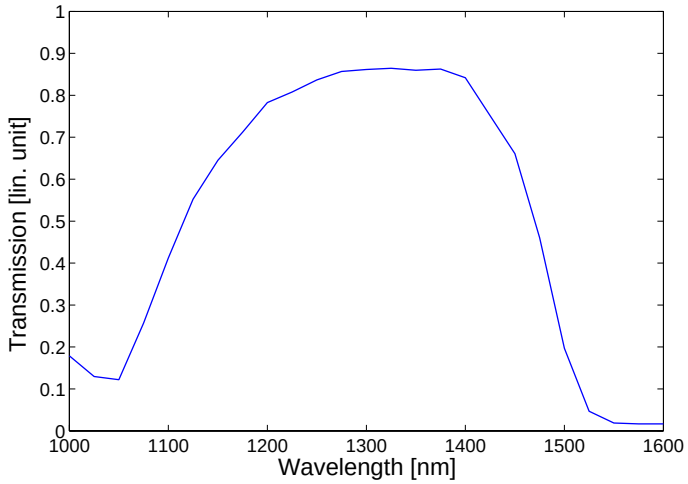

Figure 5.15: Simulated transmission spectrum of an LMA-10 filled with oil and tapered down to $107\mu m$.

3dB-bandwidth of the simulated spectrum (374nm) is larger than the one

of the experimental spectrum (250nm). This may be due to spurious effects related to the radiation in the decreasing section of the taper, i.e. power which is lost in the real device, but which is coupled back to the core mode, in the simulated one. The central wavelength of the simulated spectrum is 1325nm and it is quite in accordance with the measured one (1361nm). It is useful to have a simulation tool capable of simulating the propagation of the field along a taper, since it allows a more accurate design of LCPBG fiber devices based on tapered fibers. Unfortunately this code can work only if the structure is isotropic and, therefore, cannot be used for LCs.

5.7 Comparison between the fabricated Gaussian filters

Fig. 5.16 shows the transmission spectra of an LMA-10 ($d = 2.9\mu m$, $\Lambda = 6.6\mu m$ and $D = 125\mu m$) infiltrated with E7 and the same LMA-10 infiltrated with oil. Both liquids were filled for 1cm. It can be noticed that the loss in the middle of the bandgap is higher for the E7 spectrum (1.9dB) with respect to the oil spectrum (0.5dB). This is because of higher scattering of LCs with respect to oils and because coupling losses are higher as the LC is anisotropic. The oil spectrum also exhibits a broader bandgap with respect to E7, caused by different cut-offs of the cladding modes in the filled capillaries. After the tapering and the filling, since the diameter of the taper waist is $107\mu m$ for both, the oil-based Gaussian spectrum exhibits a broader bandwidth than the one exhibited by the E7-based one. In Fig. 5.17 the two Gaussian spectra are illustrated together. For the E7 Gaussian spectrum, the insertion loss and the 3dB-bandwidth are 2.2dB and 145nm, while for the oil Gaussian spectrum a loss of 0.5dB and a 3dB-bandwidth of 250nm were measured.

A comparison of the filters presented in this chapter can be done by determining how close they are to a perfect Gaussian function. This can be achieved by calculating the average deviation of the experimental data from the Gaussian function that best fits the experimental data. First, the amplitudes of all the experimental data were normalized to 1. Then the average deviation $\sum |(\vec{y}_{data} - \vec{y}_{fit})|/N$ was calculated, where $\vec{y}_{data}$ is a vector of length N containing the amplitude of the normalized experimental data, and $\vec{y}_{fit}$ is a vector of length N containing the amplitude of the Gaussian function which best fits the data. The experimental data and

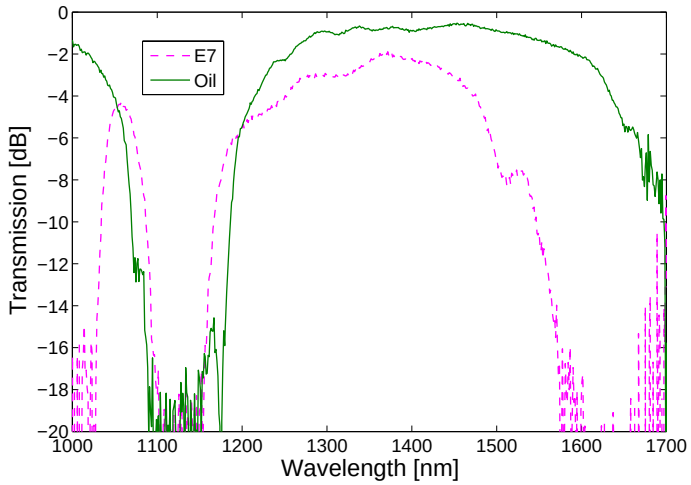

Figure 5.16: Comparison between the transmission spectra of a untapered E7-LMA-10 and a untapered oil LMA-10.

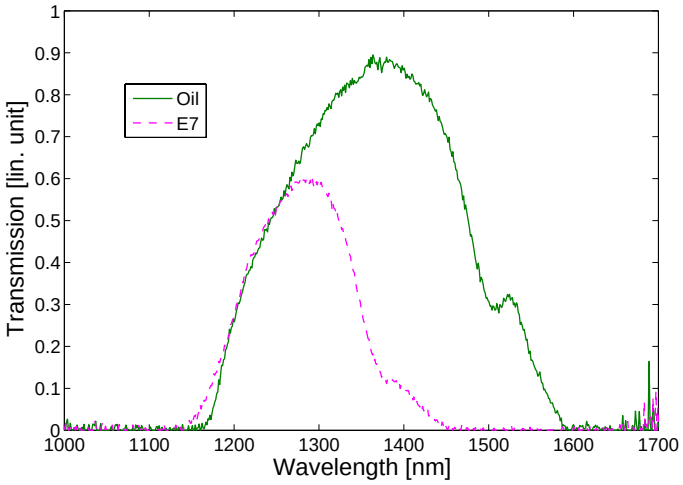

Figure 5.17: Comparison between the transmission spectra of a tapered E7-LMA-10 and a tapered oil LMA-10.

the Gaussian fits refer to the measurements plotted in Fig. 5.6, Fig. 5.9, Fig. 5.13 and Fig. 5.17. The average deviation was calculated for all the four filters described in this chapter. Table 5.1 summarizes the characteristics of these filters, with all the relevant parameters: central wavelength λ_0, 3dB-bandwidth, insertion loss, tunability and average deviation from a Gaussian function.

fiber and LC	λ_0	3dB-b.	loss	tunab.	dev.
LMA-$10^{(1)}$, $E7$	1388nm	180nm	6dB	none	0.03540
LMA-$10^{(2)}$, MDA-00-1444	1062nm	150nm	4dB	80nm	0.05021
LMA-$10^{(2)}$, oil	1361nm	250nm	0.5dB	117nm	0.04973
LMA-$10^{(2)}$, E7	1279nm	145nm	2.2dB	none	0.03729

Table 5.1: Properties of the fabricated Gaussian filters. LMA-$10^{(1)}$ has $d = 3.3\mu m$ and $\Lambda = 7.2\mu m$, LMA-$10^{(2)}$ has $d = 2.9\mu m$ and $\Lambda = 6.6\mu m$. The tunability is expressed for the temperature range in which the shape of the transmission is still Gaussian.

We can, therefore, conclude that, for OCT applications, Gaussian filters fabricated with oils are extremely promising since they exhibit low losses (0.5dB), broad bandwidth (250nm) and high tunability (117nm shift in the temperature range $25°C$-$60°C$). The use of oils is suggested if the thermal tunability, which is a slow process (about 30 seconds for a $10°C$ variation of temperature) can be tolerated in the used system. On the other hand, the deviation from a Gaussian function is higher for oil-based devices than for LC-based devices. In particular, E7 seems to be a good candidate if a filter with high "ideality" is needed, although it shows almost no tunability.

5.8 Summary

In this chapter the fabrication of PCF-based Gaussian filters was presented. The working principle behind the realization of these filters was explained, together with a description of the equipment used. These filters were achieved by infiltrating LCs or oils into tapered PCFs. Simulations using an isotropic BPM code were carried out in order to calculate the transmission spectrum of the oil-infiltrated PCF. A comparison among the fabricated

filters in terms of central wavelength, bandwidth, losses, tunability and deviation with respect to a Gaussian function was also given.

Chapter 6

Devices based on LCPBG fibers

In the previous chapter, Gaussian filters based on Liquid Crystal Photonic Bandgap (LCPBG) fibers have been illustrated.

In this chapter other devices based on LCPBG technology will be presented. These devices may find use in optical signal processing and optical networks.

As seen before, all-in-fiber LCPBG devices present many advantages compared to planar devices and free-space optics. For example, they are fiber compatible and alignment issues can, therefore, be avoided. The very high electro-optic and thermo-optic effects of Liquid Crystals (LCs) lead to remarkably high thermal and electrical tunability. Moreover, LCPBG fiber devices present low coupling losses (1.5-2dB depending on the LC used) and are very tolerant to dirt and dust if the LC does not enter in contact with the surrounding environment. This can, for example, be avoided by mechanically splicing the infiltrated Photonic Crystal Fiber (PCF) with a Single Mode Fiber (SMF), therefore sealing the holes in which the LC is contained. LCPBG fiber devices are very compact and the presence of bandgaps in the transmission spectrum opens up the possibility to use them as broadband components, for example as broadband tunable waveplates, broadband tunable couplers etc. Finally, the lifetime of these devices (not tested yet) has the potentiality to be very long, since Liquid Crystal Display (LCD) TV screens can last more than 20 years.

All-in-fiber LCPBG devices may be useful in optical networks, for example as high-pass or low-pass filters, for gain equalization, for mode conversion, or for polarization control. They may also find applications in bio-sensing, being easier to handle with respect to conventional free-space optics. Moreover, they are cheaper with respect to traditional optics. The possibility of tailoring the PCF microstructure geometry may also improve detection efficiency over standard optical fibers.

In this chapter various fabricated LCPBG fiber devices together with their properties are presented. In section 6.1 and section 6.2 a tunable bandwidth bandpass filter and a Polarization Maintaining (PM) filter are illustrated, respectively. A gain equalization filter fabricated with nanoparticle-doped LCs is proposed in section 6.3. Tunable waveplates fabricated with dual-frequency and negative LCs are discussed in section 6.4. Finally, 6.5 describes the fabrication and analysis of Long-Period Gratings (LPGs) in LCPBG fibers. A short summary is given at the end of the chapter.

6.1 Tunable bandwidth bandpass filters

A filter having transmission bands which are continuously variable in width is demonstrated.

All-in-fiber tunable bandpass filters had been previously demonstrated by applying a thermal gradient to a solid-core PCF filled with an isotropic fluid [98]. However, the setup was quite complicated. A resistive wire was used as heating element and the distance between the wire and the fiber needed to be varied, in order to induce a thermal gradient in the fiber. Furthermore, the temperature profile was characterized by inserting Bragg gratings and measuring the shift in Bragg wavelength as a function of the applied voltage.

Here, an all-in-fiber tunable bandpass filter is demonstrated without the use of a thermal gradient, but by uniformly controlling the temperature of an LC. A schematics representing the working principle of the filter is illustrated in Fig. 6.1. The fiber we used was a LMA-10 (hole diameter d=2.9μm, inter-hole distance Λ=6.6μm and outer diameter D=125μm, 4 rings). This fiber was cut in two pieces and one of the two end-facets of each piece was infiltrated with a different LC. The first end-facet was infiltrated

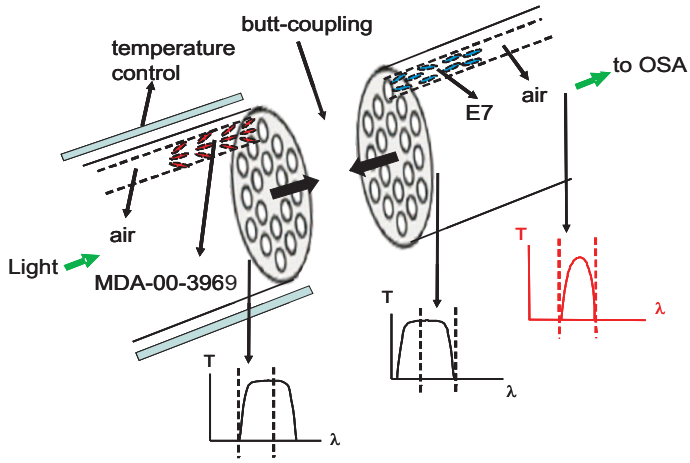

Figure 6.1: Schematic illustration of the device together with its working principle.

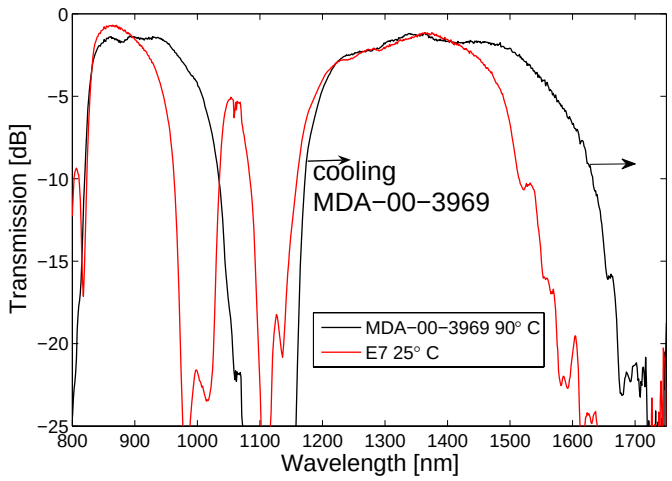

Figure 6.2: Transmission spectrum of LMA-10 filled with MDA-00-3969, 90°C (black curve), together with the transmission spectrum of LMA-10 filled with E7, 25°C (red curve). By decreasing the temperature of MDA-00-3969, the common transmission bands are narrowed.

for 9mm with MDA-00-3969, while the second one was infiltrated for the same length with E7. The two end-facets were butt-coupled together. The transmission spectra of the two filled sections are different and the light transmitted through this device falls within the common transmission bands of the E7-filled section and the MDA-filled section (see Fig. 6.1) . The total transmission through the device is then the product of the two local transmission bands. In order to have bandwidth tunability, the two local transmission spectra need to be moved with respect to each other in wavelength. This is achieved by uniformly changing the temperature of one of the two LCs. Fig. 6.2 shows the transmission spectra of E7 at $25°C$ and MDA-00-3969 at $90°C$. When the temperature of MDA-00-3969 is decreased, its spectrum shifts toward longer wavelengths and, therefore, the bandwidth of the filter is reduced.

6.1.1 Thermal tunability

In order to measure the thermal tunability of the filter, light from a supercontinuum source (SuperK, Koheras A/S, Birkerød, Denmark) was coupled into the device and the transmission spectrum was measured with an optical spectrum analyzer. If MDA-00-3969 is heated to $90°C$ and E7 is at room

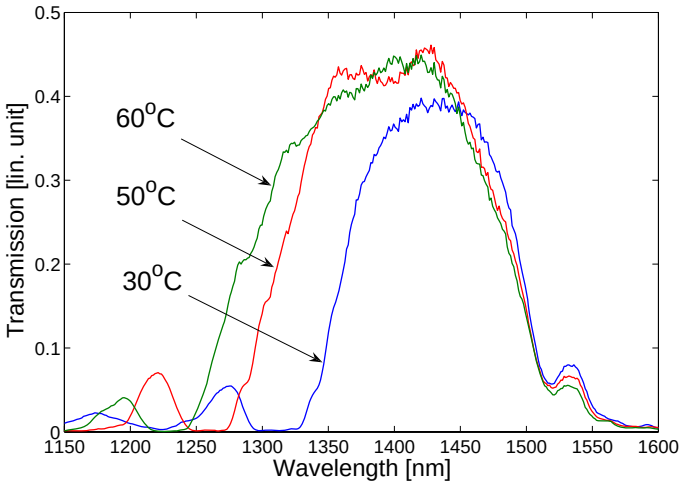

Figure 6.3: Transmission spectrum in linear unit of the fabricated LCPBG fiber device for different temperatures of MDA-00-3969.

temperature, the overlap of the two spectra covers the region 1170-1600nm. If MDA-00-3969 is cooled, the bandgaps caused by this LC move towards longer wavelengths and, consequently, the overlap is narrowed, reduced to 1300-1600 when MDA-00-3969 is at $30°C$. A bandwidth tunability of 130nm is therefore achieved by varying the temperature of one LC. Fig. 6.3 shows the transmission spectrum in linear units of this LCPBG fiber device for three different temperatures. The insertion loss at the central wavelength of the filter is 4dB.

6.1.2 Finite element simulations

The experimental results were validated with a finite element solver, able to study anisotropic waveguides both in guided and leaky regimes [99–102]. This code has been developed at the University of Bologna and utilizes a particular kind of radiation boundary conditions which have proved to give optimal results in the determination of the complex propagation constant $\beta_c = \beta - j\alpha$ of leaky modes, where β is the phase constant of the mode and α is the term accounting for radiation losses. A particularly interesting feature of this modeling tool is that it can solve structures exhibiting an arbitrary dielectric tensor $\overline{\overline{\varepsilon}}$, and it is therefore appropriate for the study of this device, where MDA-00-3969 is used. In fact, MDA-00-3969 is splayed aligned in the capillaries of the PCF and it is, therefore, necessary to consider all the 9 components of $\overline{\overline{\varepsilon}}$.

Coupling losses generated from mode mismatch at the various interfaces of the device (air-MDA-00-3969, MDA-00-3969-E7, E7-air) were calculated and added to the simulated propagation losses. Fig. 6.4 shows the simulated transmission spectrum for the device, with E7 at room temperature and MDA-00-3969 at $30°C$, $50°C$ and $60°C$. If Fig. 6.3 and Fig. 6.4 are compared, one can notice a shift of about 40nm between the central wavelength of the experimental and the simulated data. This is due to the fact that the simulations are made for a perfect uniform structure, without taking into account small non-uniformities present in a real structure. Moreover, the LC refractive indices are measured in the visible range and extrapolated to infrared wavelengths. The insertion loss is lower for the simulated spectra with respect to the experimental ones. This may be due to the fact that the air gap present between the two different LC sections is not considered in the simulations. Also, the lower transmission at $30°C$ with respect to the other temperatures, in both the

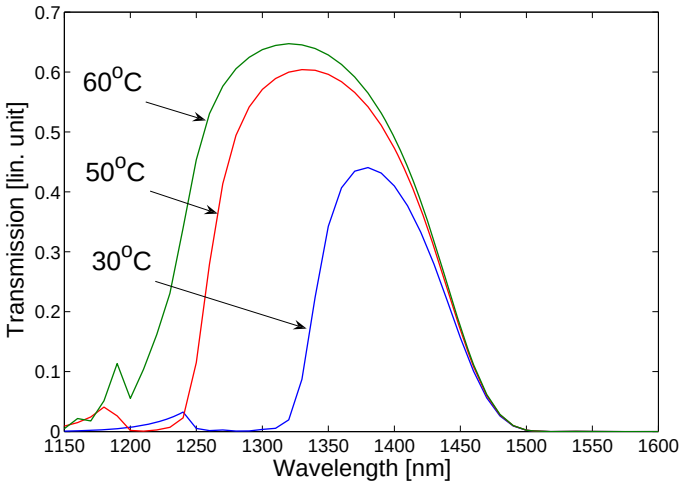

Figure 6.4: Simulated transmission spectrum (coupling losses and propagation losses) for various temperatures of MDA-00-3969.

experimental and simulated spectra, is given by the fact that at $30°C$ the bandgaps of MDA-00-3969 are pushed so much towards longer wavelengths that the overlap of the E7 spectrum and the MDA-00-3969 spectrum is at the bandgap edge and, therefore, it becomes more lossy.

6.2 Polarization maintaining filters

A tunable PM filter with a Polarization Extinction Ratio (PER) of 14dB is fabricated by using a PM fiber infiltrated with LC.

PM filters can find applications in all-PM modelocked fiber lasers, for example they can be used for spectral shaping in the cavity [103], Amplified Spontaneous Emission (ASE) filtering in the amplifiers, and for tunable dispersion control both inside and outside the cavity. Tunability gives a further degree of freedom in the above mentioned applications.

The filter was fabricated by using an LMA PM fiber with a core size of $15\mu m$ (LMA-PM-15, d=$4.7\mu m$, Λ=$9.8\mu m$ and D=$230\mu m$) from Crystal Fibre A/S. A cross section of this fiber is shown in Fig. 6.5. Boron rods

were inserted on opposite sides of the core at the preform stage in order to obtain stress-induced birefringence that facilitates the PM properties of the fiber. LMA-PM-15 has a birefringence $\geq 8 \times 10^{-5}$ in the spectral range 900-1700nm and a PER of $\geq 20dB$ at 1550nm. The LC MDA-00-3969 is infiltrated in this fiber for 1.2cm in order to induce a filtering effect in the fiber. The setup for the characterization of the PM LCPBG fiber device is illustrated in Fig. 6.5. The PER measurement at room temperature was

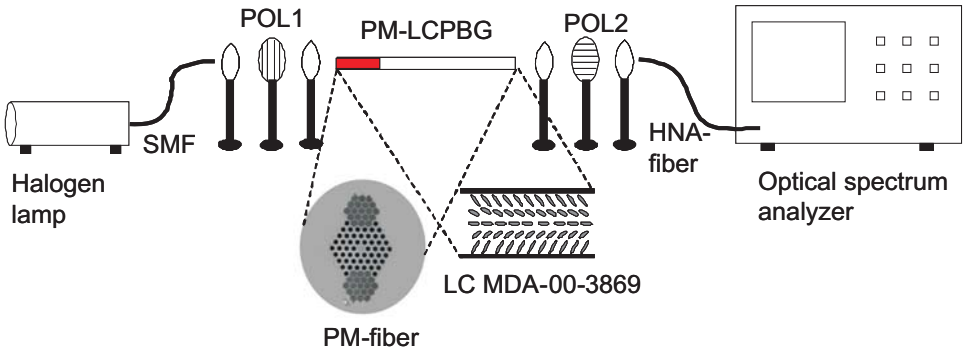

Figure 6.5: Schematic of the setup together with a micrograph of the LMA-PM-15 (Courtesy of Crystal Fibre A/S).

performed by positioning the filled fiber between two polarizers. Lenses with a magnification of 20x and a Numerical Aperture (NA) of 0.5 were used to couple white light from a halogen lamp into the PM LCPBG fiber device. The light was collected by an optical spectrum analyzer through a High Numerical Aperture (HNA) optical fibre. The first polarizer was aligned along the slow or the fast axis of the fibre. The second polarizer was added, and the two polarizers were iteratively rotated to minimize the transmission in the bandgaps. The resulting spectrum was recorded and corresponds to curve a) in Fig. 6.6. Then the second polarizer was rotated 90°, in order to be co-aligned with polarizer 1. The corresponding transmission spectrum is shown in curve b) of Fig. 6.6. The PER is the ratio between the power measured in these two cases - the polarizers in-line and the polarizers crossed - in dB units. In order to verify that polarizer 1 was in fact aligned along one of the two PM axes, polarizer 1 was rotated 90° and the same measurements as above were repeated (curves c) and d) of Fig. 6.6). The transmission spectra for these two cases were expected to be the same if polarizer 1 was aligned along one of the two PM axes. In Fig. 6.6

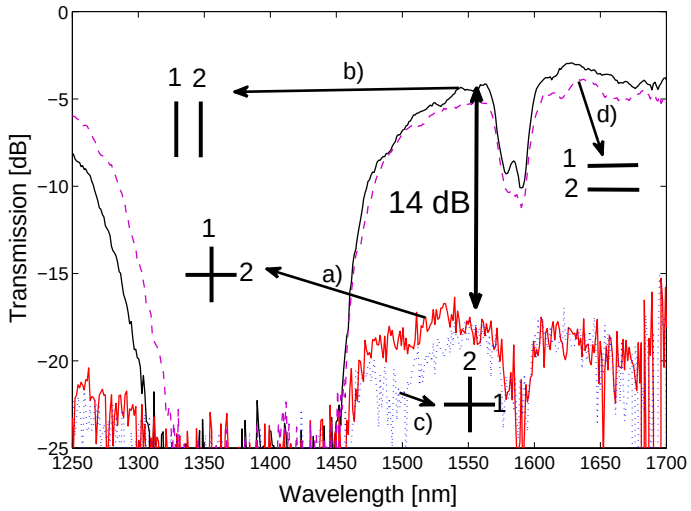

Figure 6.6: Transmission spectrum of the PM LCPBG fiber device measured with crossed (minimum transmission) and inline polarizers (maximum transmission) at room temperature.

we notice a small difference between the two spectra. We expect this to be caused by the LC alignment which does not have a perfect cylindrical symmetry in the holes of the fibre. This causes the two linear polarizations propagating in the fiber to experience a slightly different refractive index while propagating. A PER of 14 dB is measured at 1550nm and a PER of 17 dB is measured at 1200nm.

6.2.1 Thermal tunability

The thermal tunability of the PM LCPBG fiber filter is investigated by positioning the LC filled section on a thermal plate. An SMF connected to a white light source is butt-coupled to the filter and the transmission spectrum is measured using an optical spectrum analyzer. The temperature of the thermal plate is varied from $30°C$ to $70°C$ and the transmission spectrum is recorded every $10°C$. Fig. 6.7 shows the wavelength of the notch as a function of temperature. A tunability range of 250nm is achieved in this temperature range. The shift of the bandgaps as a function of temperature is almost linear. If a different operating wavelength range is necessary,

then a different LC can be used in order to shift the bandgaps to specific wavelengths required by the specific application.

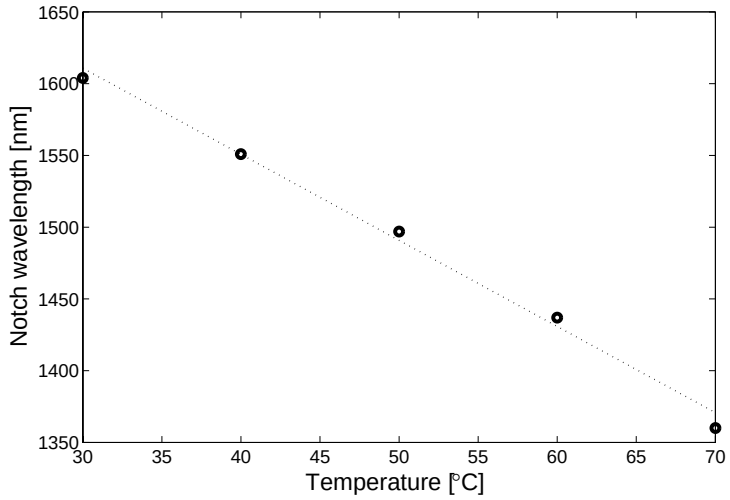

Figure 6.7: Thermal tunability of the PM LCPBG fiber device.

6.2.2 Finite element simulations

Finite element simulations were also carried out in order to obtain the transmission spectrum of the PM LCPBG fiber device and compare it to the experimental one. The modeling tool is a commercial software that can solve structures exhibiting arbitrary dielectric tensors.

Coupling losses generated from the mismatch of the Total-Internal-Reflection (TIR) mode with the Photonic BandGap (PBG) mode are calculated. Reasonable agreement between the measurements and the simulations is observed. By comparing Fig. 6.6 with Fig. 6.8 a shift of 20nm between the two spectra is observed for the notch in the 1450-1700nm bandgap and a shift of 50nm is observed for the bandgap at lower wavelengths. We believe this difference is due to varying hole size of the fiber used in the experiments compared to the simulated one, which is an ideal fiber with perfectly cylindrical capillaries, not varying in size. Moreover, the LC refractive indices were measured with an Abbe refractometer at

visible wavelengths and extrapolated to the infrared by using the Cauchy parameters, therefore introducing an error on the extrapolated values.

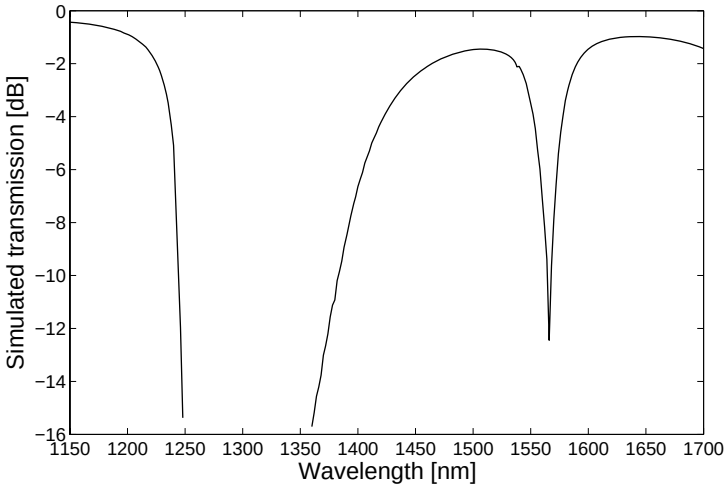

Figure 6.8: Simulated transmission spectrum of the PM LCPBG fiber device at room temperature.

6.3 Gain equalization filters with nanoparticle-doped LCs

In the last decade, considerable research has been devoted to the fabrication and study of nanomaterials [104, 105] which can be used for electro-optic device technology such as LCDs. Ferroelectric nanoparticles can be used in order to align the LCs and to increase the contrast ratio of LC cells [106] or can be dispersed in the LC directly in order to increase birefringence and dielectric anisotropy [107] or induce frequency modulation response [108, 109].

Here we investigate the properties of a PCF infiltrated with LCs doped with barium titanate ($BaTiO_3$) nanoparticles. The frequency dependent behavior of the nanoparticles influences the frequency dependent behavior of the LCs in which they are dispersed. This results in the possibility of tuning the transmission spectrum by varying the frequency of the applied electric field.

Moreover, the fabricated device presented here has a transmission spectrum with an interesting feature on the short wavelength side of the bandgap edge. For voltages below $160V_{rms}$, in fact, only the short wavelength side of the bandgap is influenced by the application of an external field and the slope of this edge is adjustable by changing frequency and amplitude of the applied voltage. This characteristic makes the device particularly attractive as a telecommunication device and, in particular, as a tunable all-in-fiber gain equalization filter. The voltage threshold and its frequency dependent behavior were also measured and compared for both undoped and doped LCs infiltrated in a silica capillary and, successively, in a glass cell.

An LMA-10 (d=3.1μm, Λ=7.2μm and D=125μm) from Crystal Fibre A/S was used in this experiment. The mixture used to infiltrate the fiber is the LC E7, in which $BaTiO_3$ nanoparticles were dispersed. The measured dielectric anisotropy of this mixture at 1kHz is 13.4, the splay elastic constant K_{11} is 7.34pN and the bend elastic constant K_{33} is 9.3pN. $BaTiO_3$ nanoparticle dispersion in E7 was prepared as follows: 50mg of nanoparticles were suspended in 20mL of dimethyl sulfoxide (DMSO) together with 50mg of a 4'-n-pentyl-4-cyano-biphenyl (5CB) LC as a dispersant by sonification for 4 hours. 0.25mL of this suspension was added to 1g of E7 using sonification for 1 hour. Then the mixture was held under vacuum (0.1 torr) for 48 hours in order to remove the DMSO. The final concentration of nanoparticles was estimated to be around 0.01% by weight. The problem of mixture stability is a sensitive topic and was reported by several research groups. In [110] a LC mixture with $Sn_2P_2S_6$ was found to be stable for at least 6 months and in [111] a LC mixture with $BaTiO_3$ nanoparticle was found to be stable for at least one year. In case of our experiment, sedimentation of nanoparticles was observed during the first step of the dispersing process. Therefore, the concentration of the nanoparticles in the LC host was further decreased until no sedimentation was observed. The experiments with infiltrated fiber were repeated after 3 months and showed the same results.

Polarized Optical Microscopy (POM) observations of a 5μm silica capillary tube infiltrated with this mixture indicated that the LC directors exhibited planar alignment along the axis of the fiber, like pure E7. Since the alignment was planar, the procedure used in [19] for pure E7 was also applied here: in order to stabilize the molecular alignment, the mixture was

heated up to the isotropic phase and then cooled down slowly.
The setup is the same as the one already presented in Fig. 4.5. The infiltrated fiber was positioned on an xyz Thorlabs stage equipped with a thermal plate and electrodes. The transmission of the fiber device was measured using a white light from a Tungsten-Halogen light. Light from the source was guided by a LMA fiber and coupled into the LCPBG fiber by aligning the two fibers on the xyz-stage. The transmission was then measured by an optical spectrum analyzer and normalized to that of the unfilled fiber. Later, in order to apply an external electric field to the device, a function generator and an amplifier were added to the setup.

6.3.1 Spectral properties and frequency tunability

First, the transmission spectrum was measured without applying any external electric field. Fig. 6.9 shows the transmission spectrum at three different temperatures. The loss in the middle of the widest bandgap was

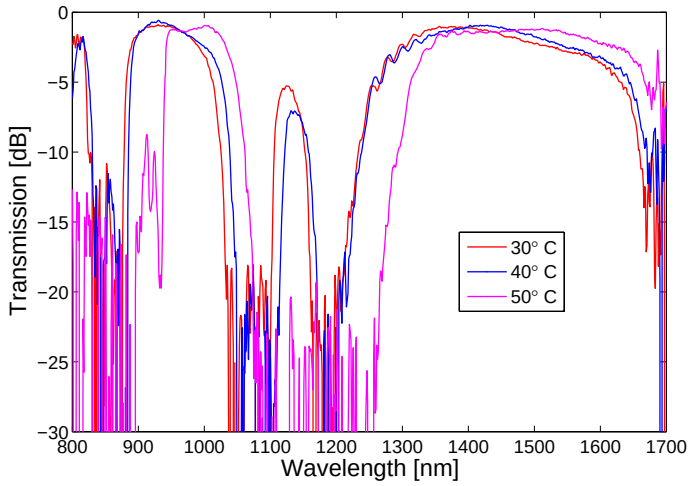

Figure 6.9: Transmission spectrum of LMA-10 infiltrated with E7 doped with $BaTiO_3$ nanoparticles at three different temperatures.

measured to be 1.5dB, comparable to the one achieved with undoped E7 [19], indicating that the presence of nanoparticles did not induce extra scattering and, therefore, any extra loss. The thermal tunability was also

comparable to pure E7 [19].

In order to investigate the frequency dependence induced by the nanoparticles, a sinusoidal voltage at different frequencies (100Hz, 500Hz, 1kHz, 10kHz, 30kHz and 100kHz) was applied to the infiltrated section and the transmission spectrum was recorder for each frequency. For each frequency, the amplitude of the voltage was varied from 0 to $200V_{rms}$ in steps of $40V_{rms}$. In order to study the effect of the nanoparticles added to the LC, the same measurements were carried out for pure E7 and the two results were compared. Fig. 6.10 shows the transmission spectra of doped-E7 (a) and pure E7 (b) when the frequency of the applied electric field is 100Hz. Fig. 6.11 shows the transmission spectra of doped-E7 (a) and pure E7 (b) when the frequency of the applied electric field is 500kHz. Fig. 6.12 shows the same, but with a frequency of 1kHz. One can note that, while the behavior of E7 is not affected by the frequency of the applied field, the behavior of E7 doped with nanoparticles is strongly influenced by the frequency chosen. In particular, it can be observed from Fig. 6.10 that, at 100 Hz, there is almost no change of the bandgaps for the nanoparticle-doped E7 with a voltage in the range $0 - 200V_{rms}$, while pure E7 responds at the same frequency if a voltage $> 100V_{rms}$ is applied. By stepwise increasing the frequency of the ac field, we notice that the intensity of the response to the field increases towards 30kHz, to become lower again at 100kHz (see Fig. 6.13). In fact, while the E7 response is almost the same in the range 100Hz-100kHz, this does not apply to E7 doped with $BaTiO_3$ nanoparticles. In this case, at high frequencies the response is lower because the nanoparticles cannot follow the ac field, therefore 'blocking' also the reorientation of the LC molecules in contact with the nanoparticles. For the low frequency case, the ionic impurities that might exist in the E7 host or have been introduced during dispersion of nanoparticles can cause shielding of the low frequency field. Therefore, in both cases, a higher voltage with respect to pure E7 was needed to observe a change of the bandgaps.

Another interesting characteristic of the transmission spectrum of LMA-10 infiltrated with nanoparticle-doped E7 is that, for voltages below $160V_{rms}$, only the short wavelength side of the bandgap is influenced by the application of an external field. In the case of nanoparticle-doped E7 it seems that the EH_{11} mode (which determines the short bandgap edge) is pushed more into the bandgap with respect to the pure E7 case. Fig. 6.13

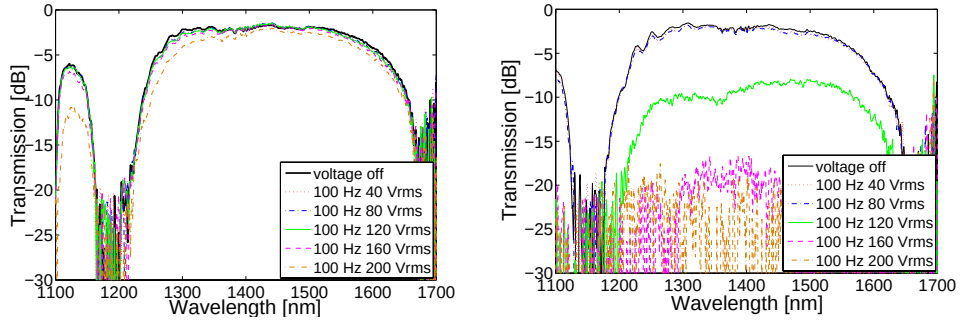

(a) $BaTiO_3$-doped-E7 and LMA-10 (b) Pure E7 and LMA-10

Figure 6.10: Transmission spectra for various amplitudes of the applied field at a frequency of 100Hz.

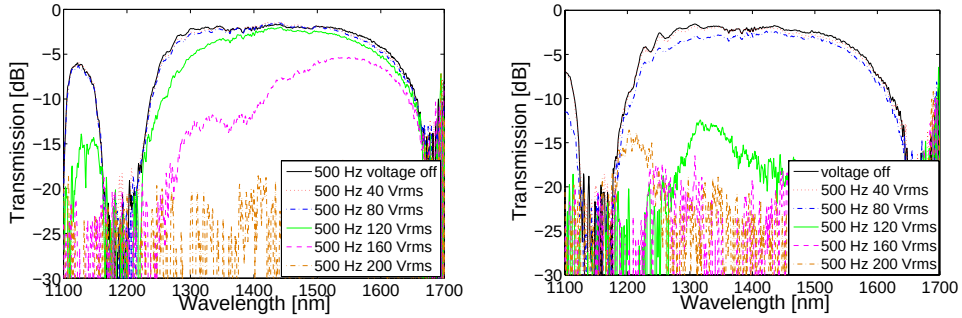

(a) $BaTiO_3$-doped-E7 and LMA-10 (b) Pure E7 and LMA-10

Figure 6.11: Transmission spectra for various amplitudes of the applied field at a frequency of 500Hz.

shows this effect, together with the bandgap frequency tunability. One can note that the effect of the field is only on the short side of the bandgap and that its slope can be adjusted by varying the frequency of the applied field. This effect can be potentially used as a gain equalization filter or as a tunable filter which can be dynamically adjusted to meet the requirement of an optical network.

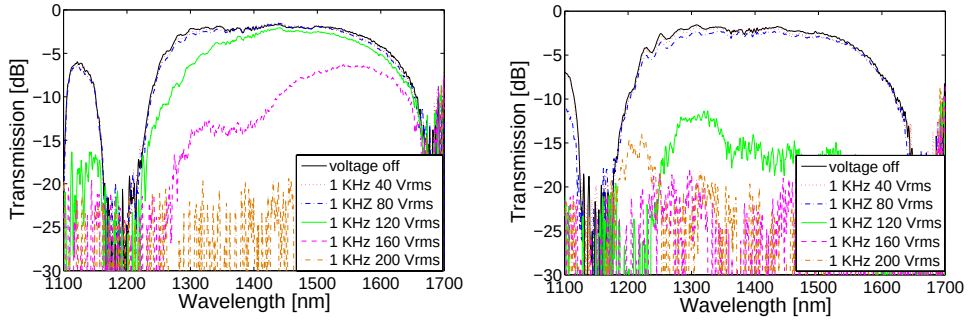

(a) $BaTiO_3$-doped-E7 and LMA-10 (b) Pure E7 and LMA-10

Figure 6.12: Transmission spectra for various amplitudes of the applied field at a frequency of 1kHz.

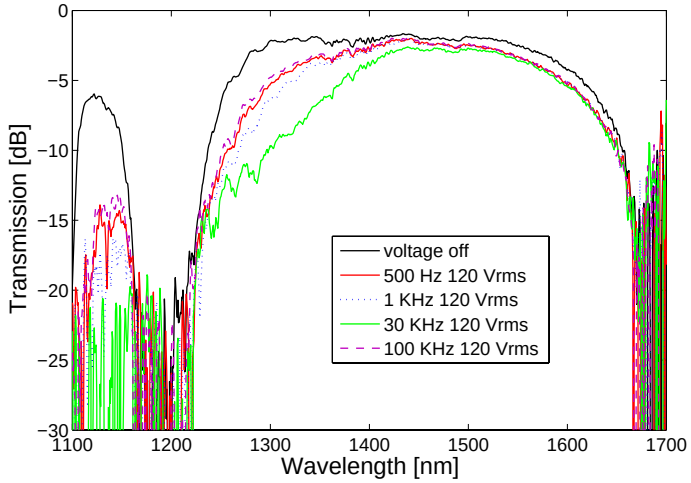

Figure 6.13: Transmission spectrum of LMA-10 infiltrated with nanoparticle-doped E7 as a function of the frequency of the external electric field. The amplitude of the voltage is constant ($120V_{rms}$). The shape of the short wavelength edge can be controlled through adjustment of the frequency.

6.3.2 Threshold voltage for a silica capillary

The LC alignment in a silica capillary under the effect of an external electric field was studied using a POM technique. This allowed to measure the

threshold voltage at different frequencies and, therefore, have a confirmation of what was observed in a PCF in the previous section.

Two silica capillary tubes with an inner diameter of $5\mu m$ and an outer diameter of $150\mu m$ were prepared: one was filled with the nanoparticle-doped E7 mixture and the other was filled with pure E7. The capillaries were sandwiched between two glass plates covered with transparent Indium-Tin-Oxide (ITO); two unfilled capillaries were used as spacers and a few drops of a UV-curable polymer on the electrodes made sure that the filled capillaries did not move while under study. For planar aligned LCs, their molecules move only if the amplitude of the voltage is above the Fredericks transition threshold. As the voltage increases, the first change of color corresponds to the Fredericks transition threshold (see Fig. 6.14). The frequency of

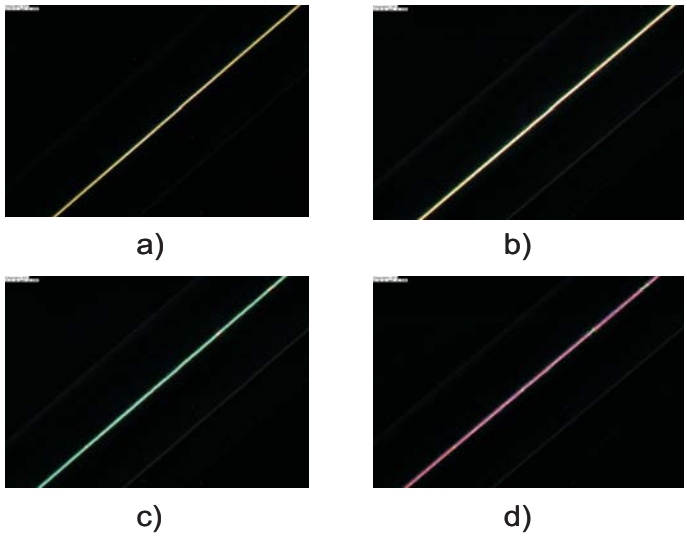

Figure 6.14: Polarization optical micrograph of a $5\mu m$ silica capillary infiltrated with nanoparticle-doped E7 for (a) $V = 0V_{rms}$, f=1kHz, (b) $V = 62V_{rms}$, f=1kHz, (c) $V = 88V_{rms}$, f=1kHz, (d) $V = 116V_{rms}$, f=1kHz.

the ac field was also varied and the same procedure was repeated in order to obtain the threshold for each frequency chosen. It was observed that the threshold was higher than that of pure E7 at low frequencies (100Hz and 500Hz), comparable with E7 at 1kHz, 30kHz and 50kHz and increased again towards 100kHz. This is in agreement with the transmission spectra

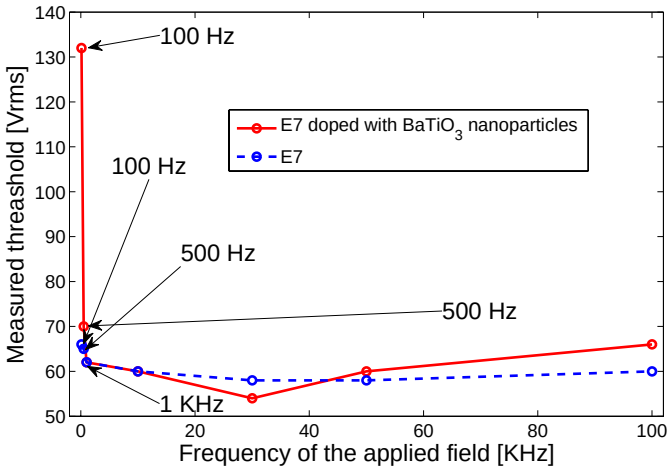

Figure 6.15: Measured Fredericks threshold at different frequencies for nanoparticle-doped E7 and pure E7 in a silica capillary.

shown in Fig. 6.10, Fig. 6.11, Fig. 6.12 and Fig. 6.13. Pure E7, on the other hand, was not strongly influenced by the frequency of the applied field, in accordance with what is shown in Fig. 6.10, Fig. 6.11 and Fig. 6.12. Fig. 6.15 shows the measured Fredericks transition for both pure E7 and nanoparticle-doped E7 as a function of the frequency of the external field. The frequency dependence of the $BaTiO_3$ nanoparticle doped E7 mixture in a silica capillary shows an analogous behavior of the one observed inside a PCF, as expected.

6.3.3 Threshold voltage for a glass cell

The threshold voltage of both doped and undoped E7 were measured in a glass cell, again in order to have a further proof of what was observed inside a PCF. In fact, the frequency dependent behavior is expected to appear also in the case of a cell.

A homogeneous cell, i.e. with planar alignment layer, with a cell gap $d \sim 8\mu m$ was prepared and filled with nanoparticle-doped E7. Later, the same experiment was repeated, but with pure E7. Fig. 6.16 shows the

schematic diagrams of the experimental setup. A He-Ne laser ($\lambda = 632.8nm$)

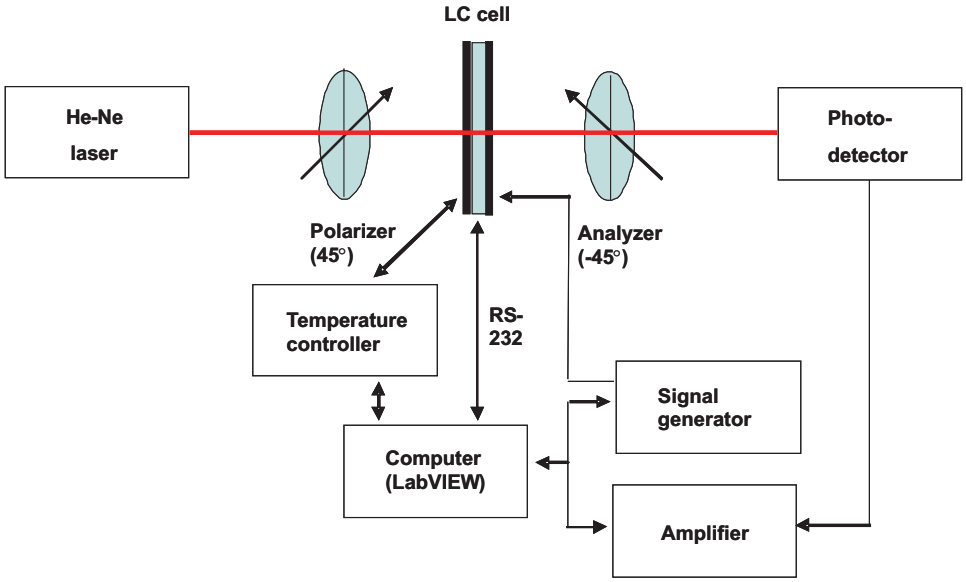

Figure 6.16: Experimental setup for measuring the threshold voltage of a glass cell infiltrated with LC.

was used as light source. The linear polarizer was oriented at 45° with respect to the LC rubbing direction and the analyzer was crossed. This configuration gives the maximum phase retardation of the linearly polarized light impinging upon the cell, due to different propagating speed of the extraordinary and ordinary rays in the LC medium. The phase retardation can be expressed as [112, 113]

$$\delta(V, T, \lambda) = \frac{2\pi d \Delta n(V, T, \lambda)}{\lambda} \tag{6.1}$$

where d is the cell thickness, Δn is the LC birefringence, T the temperature and λ the wavelength. The normalized transmittance Tr is related to δ as following [112, 113]

$$Tr = \sin^2(\frac{\delta}{2}) \tag{6.2}$$

The transmission was measured by using a photodiode detector (New Focus Model 2031) and recorded digitally by a data acquisition system (DAQ,

PCI 6110) using LabVIEW. An AC voltage square wave was used to drive the LC cell whose inner sides were coated with ITO electrodes. On top of the ITO, the substrate was covered with a thin polyimide alignment film. The induced pretilt angle was about 3°.

The transmission was measured at various frequencies of the ac field. It was found that the square shape of the signal was undistorted by the amplifier only for frequencies in the range 10Hz-10kHz, therefore measurements were only carried out at 10Hz, 50Hz, 100Hz, 500Hz, 1kHz, 10kHz, in order to be able to compare the results.

The experiments were carried out at $40°C$. In fact, the threshold voltage change upon frequency was more obvious at elevated temperature than at regular room temperature conditions. This phenomenon can be explained noting that the rotational viscosity of E7 decreases with increasing temperature, making the E7 LC molecules more vulnerable to be affected by driving voltage frequency changes.

The recorded transmissions of the doped LC cell is shown in Fig. 6.17 for different frequencies of the applied electric field (10Hz, 100Hz 500Hz, 10kHz). The phase retardation δ was calculated by inverting Eq. (6.2). In order to calculate the threshold voltage, the phase change $\Delta\phi = \delta_{max} - \delta$ was plotted as a function of voltage and a linear extrapolation was done near the threshold region [113], as shown in Fig. 6.18.

The phase change and the threshold voltage were calculated for 10Hz, 50Hz, 100Hz, 500Hz, 1kHz and 10kHz. Fig. 6.19 shows the threshold voltage as a function of frequency for both doped and undoped E7. Again it was found a behavior of the threshold voltage as a function of frequency (low frequency case) similar to the one found before for a capillary. This confirms that the frequency modulation effect induced by the presence of nanoparticles can be observed in different geometries, such as cylindrical (PCF and capillary) and squared (cell). Unfortunately, it was not possible to explore the high frequency case, because of limitation of the setup used, as explained above.

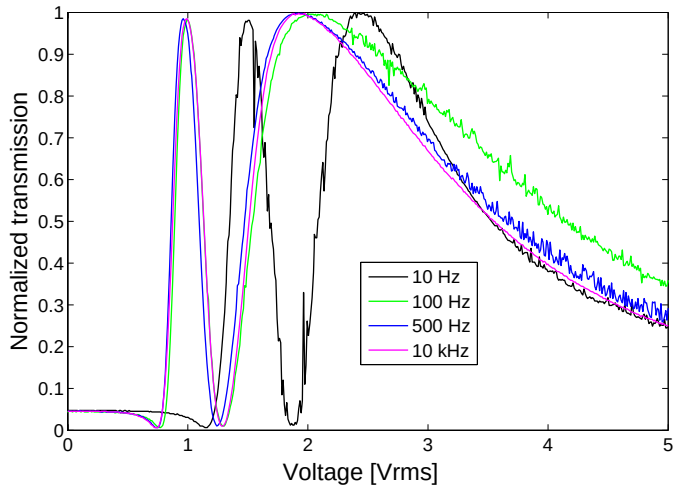

Figure 6.17: Voltage-dependent transmission of a homogeneous $8\mu m$ cell filled with $BaTiO_3$ nanoparticle-doped E7 for different frequencies of the external applied field.

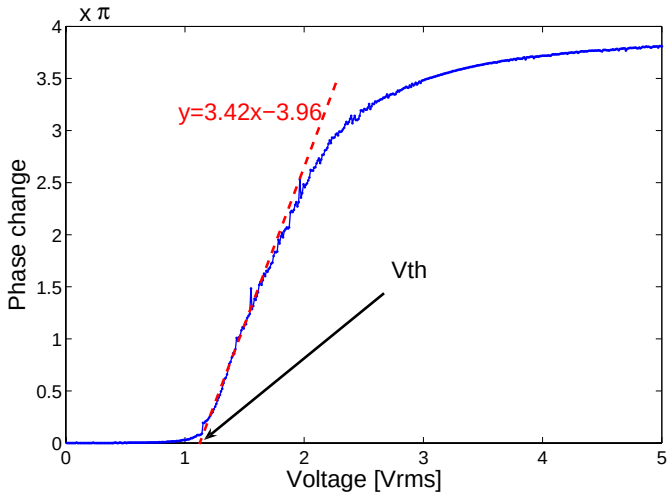

Figure 6.18: Voltage-dependent phase change of the $BaTiO_3$ nanoparticle-doped cell when a 10Hz square wave is applied to the cell.

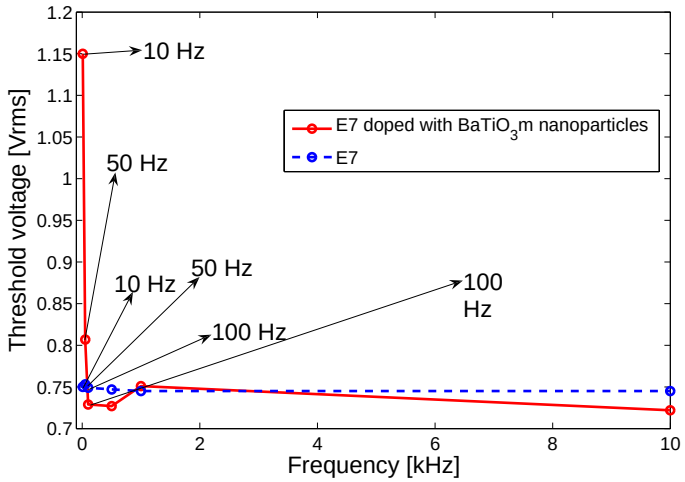

Figure 6.19: Measured Fredericks transition threshold at different frequencies for nanoparticle-doped E7 and pure E7 in a glass cell.

6.4 Tunable waveplates

Under the application of an electric field, because of the reorientation of the LC, the bandgap shift becomes polarization dependent. The guided modes (eigenstates) loose their degeneracy and experience a different phase delay when propagating through the LCPBG fiber. This opens up the possibility of tuning the birefringence of the structure by applying an external electric field, therefore making the realization of all-in-fiber electrically driven tunable waveplates possible.

In literature, birefringence control was demonstrated in [13], where selective filling of the air-holes of a microstructured "grapefruit" fiber induced birefringence, which could be tuned by temperature tuning the polymer infiltrated in the holes. Polarization controllers and polarization switches were also demonstrated by using microstructured fibers equipped with internal electrodes. High voltage applied to the fiber heat and expand the internal electrodes causing a polarization rotation [114, 115].

The advantage of using LCs in PCFs for making polarization controllers is the fabrication process, which is very simple. Among available LCs, the splayed-aligned ones are the most appropriate to be used for the fabrication of tunable waveplates. In fact, these LCs, as previously discussed, do not have a Fredericks transition threshold and do not exhibit reverse tilt domain defects, such as planar aligned LCs. The presence of a Fredericks transition threshold means that the molecules switch from one state to another only if the voltage is higher than a certain threshold. The birefringence, therefore, changes abruptly from one value to another when the voltage reaches the threshold value and its tunability becomes difficult to control. Moreover, in planar aligned LCs, due to thermal fluctuations, the director can tilt in two different directions when an electric field is applied to the LC, causing orientational defects at the border between two reverse tilt domains. Such defects cause a local change of the refractive index which introduces voltage-dependent extra-loss. In tunable waveplates and birefringence controllers, the loss of the device should preferably be constant and not dependent on the voltage applied to the device. Therefore, splayed-aligned LCs are the most useful ones for the fabrication of waveplates and birefringence controllers. Here, two different splayed-aligned LCs were used: a dual-frequency LC (MDA-00-3969) and a negative dielectric anisotropy LC (MLC-6608). Both allowed the realization of tunable waveplates and birefringence controllers.

The setup was the same for both the fabricated devices. A polarized and tunable laser source operating from 1520nm to 1620nm was connected to the LCPBG fiber through a polarization analyzer (HP/Agilent 8509B Polarization Analyzer). A polarization controller was used to find a polarization state with a transmission spectrum between the maximum and minimum states. This ensured that equal power was launched into the two eigenstates. The polarization analyzer was used to launch the light in the LCPBG fiber and to resolve the output light into the Stokes parameters, plotted on the surface of the Poincaré sphere. Any voltage change inducing a phase shift between the orthogonal polarizations in the device results in a rotation on the sphere. The change in birefringence was estimated. When no field is applied, the birefringence (Δn) is related to the phase difference (ϕ) between the two eigenstates

$$\phi = (\beta_x - \beta y)L = \frac{2\pi(n_x - n_y)L}{\lambda} = \frac{2\pi\Delta nL}{\lambda} \tag{6.3}$$

where β_x and β_y are the propagation constants of the two guided modes and n_x and n_y their effective refractive indices. If an electric field is applied to the LCPBG fiber device, an additional phase shift is induced

$$\Delta\phi = \frac{2\pi(\Delta n_U - \Delta n_0)L}{\lambda} \tag{6.4}$$

where Δn_0 is the birefringence when no voltage is applied and Δn_U is the birefringence when a voltage V=U is applied. Therefore from the additional phase shift $\Delta\phi$ (which can be measured on the Poincaré sphere), it is possible to determine the induced birefringence Δn_i caused by the application of an external electric field

$$\Delta n_i = \frac{\Delta\phi\lambda}{2\pi L} \tag{6.5}$$

6.4.1 Tunable waveplates with dual-frequency LCs

In order to fabricate a tunable waveplate, the holes of an LMA-15 (d=5μm, Λ=10μm and D=125μm) were infiltrated for 8mm with the dual-frequency LC MDA-00-3969. The transmission spectrum of this filled fiber is shown in Fig. 6.20. The loss is higher compared to other fibers filled with the same LC because of varying capillary diameter, visible by looking at the end-facet with a fiberscope. The tunable laser source was set to 1600nm and equal power was launched into the two orthogonally modes of the LCPBG fiber. Voltages of $18V_{rms}$, $35V_{rms}$, $55V_{rms}$ and $82V_{rms}$ at a frequency of 1kHz were applied to the device. The rotation of the state of polarization on the Poincaré sphere is shown in Fig. 6.22, while the corresponding induced birefringence is shown in Fig. 6.21. A birefringence of 3×10^{-5} was induced by applying a voltage of $82V_{rms}$, which corresponds to a $\lambda/6$ waveplate at 1600nm. In order to obtain full polarization control, a $\lambda/2$ waveplate must be obtained. This can be achieved by infiltrating the fiber for a longer section.

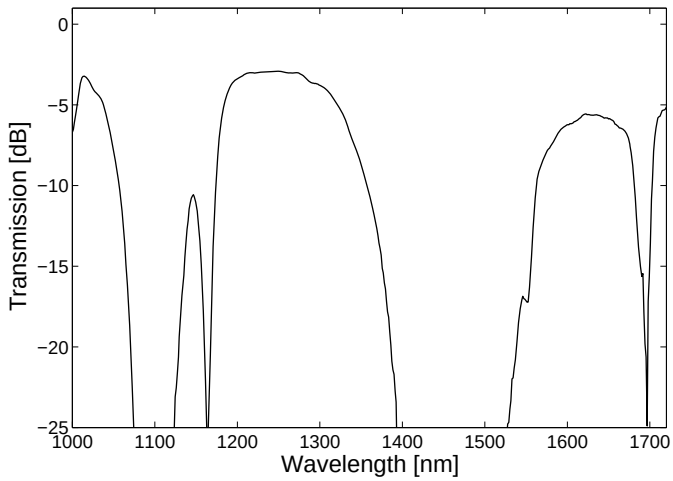

Figure 6.20: Transmission spectrum of LMA-15 infiltrated with MDA-00-3969. The high loss is due to the fabrication process of the fiber.

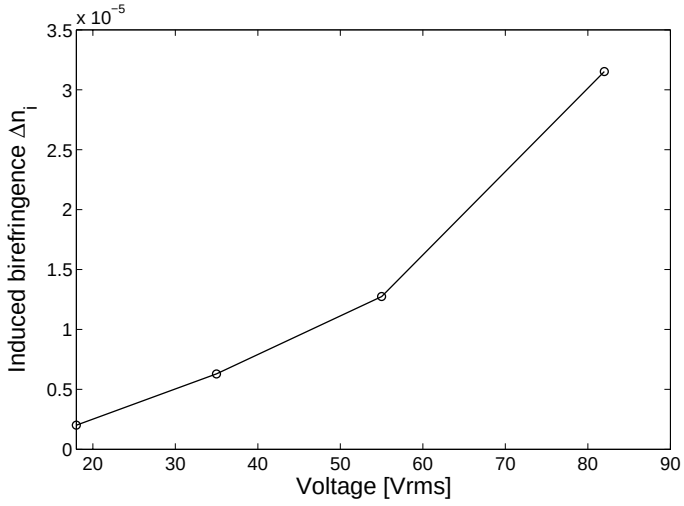

Figure 6.21: Induced birefringence as a function of voltage at $\lambda = 1600nm$ and $25°C$.

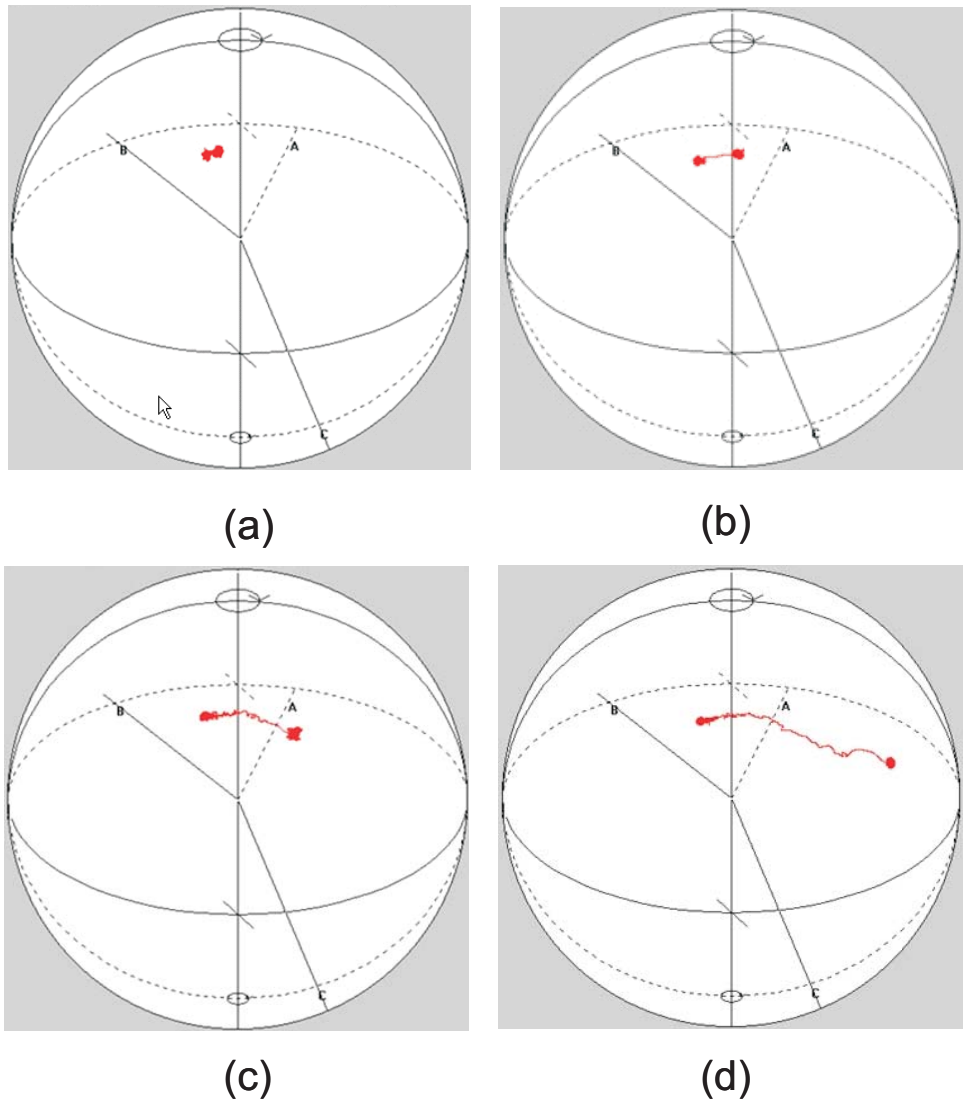

Figure 6.22: Induced phase shift on the Poincaré sphere when (a) $18V_{rms}$, (b) $35V_{rms}$, (c) $55V_{rms}$, (d) $82V_{rms}$ are applied to the LCPBG device.

6.4.2 Tunable waveplates with negative dielectric LCs

The fiber used in the experiments is an LMA-13 (d=4.3μm, Λ=8.5μm and D=125μm, Crystal Fibre A/S, Denmark). The negative dielectric LC is MLC-6608 (Merck, Darmstadt, Germany), which has a wavelength dependent ordinary and extraordinary refractive index of $n_o = 1.4756$ and $n_e = 1.5586$ at 589nm and at 20°C. The dielectric anisotropy at 1kHz and 20°C is -4.2. POM observations on a single LC infiltrated 5μm diameter capillary showed that MLC-6608 was aligned in a 90° splayed alignment. This LC was infiltrated for 20mm of the length of the fiber using capillary forces.

The electrical and thermal tunabilities of this device were investigated first. The LC filled section was sandwiched between two electrodes and a 1kHz sine wave was applied. Fig. 6.23 shows the transmission spectrum with applied voltage from $0V_{rms}$ to $200V_{rms}$ at 30°C. The notch appearing in the transmission spectrum is caused by a cladding mode crossing a bandgap, forming a so-called "avoided-crossing" with the core mode of the bandgap. The same phenomenon was also found by infiltrating PCFs with 45° splayed aligned, such as MDA-00-3969 [76]. Tunable notch filters have a wide range of applications, among others, in optical filtering or gain equalization of optical communication systems.

One can notice from Fig. 6.23 that the long-wavelength edge is shifted towards shorter wavelengths by increasing the voltage, while the short-wavelength edge of the same bandgap centered at 1375nm is almost kept in the original position. This feature is caused by different sensitivity of the PBG modes to the electrically induced alignment of the LC. The shift of the long-wavelength bandgap edge is almost linear in the range $50V_{rms} - 200V_{rms}$, with a tunability of $0.42nm/V_{rms}$, while for voltages in the range $0V_{rms} - 50V_{rms}$, the shift is smaller. This is given by the fact that the change of the elastic free-energy caused by the application of an external electric field $\vec{E}$ is proportional to $|E|^2$ and, therefore, the change in the LC alignment is greater at high voltages. During the tuning process, the notch is also shifted towards shorter wavelengths and the maximum tuning ability of this loss dip is 26.5nm with $200V_{rms}$.

The temperature tunability was also measured by varying the temperature of the infiltrated section from 22°C to 80°C. A remarkably large

shift of 396nm was measured in this range. The tuning process was found to be quite linear with a tuning sensitivity of $6.8nm/°C$. By increasing the temperature, the bandgap was shifted towards shorter wavelengths.

By using the same setup as the one used above for the dual-frequency LC, the phase shift on the Poincaré sphere was measured when a driving voltage of $0V_{rms}$, $60V_{rms}$, $120V_{rms}$ and $180V_{rms}$ was applied to the device and when 1550nm polarized laser light was launched. The induced shift on the Poincaré sphere is shown in Fig. 6.24. Fig. 6.25 plots the electrically

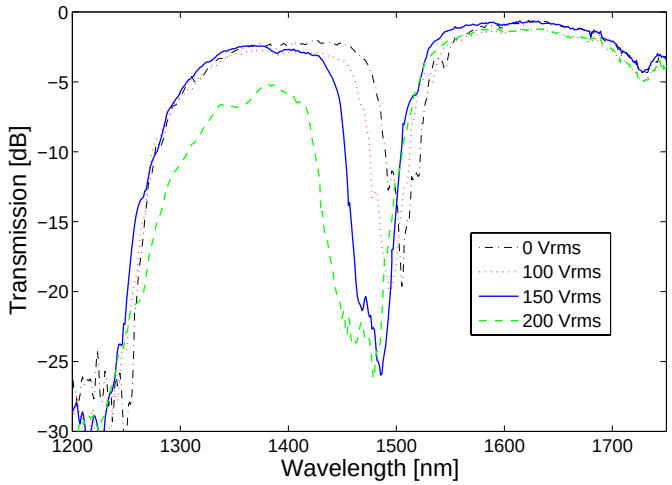

Figure 6.23: Transmission spectrum of LMA-13 filled with 20mm MLC-6608 for different voltages at $30°C$.

induced phase shift and Fig. 6.26 plots the corresponding birefringence change of the LCPBG fiber device as a function of voltage for different wavelengths at $30°C$. A phase shift of 222.5° can be obtained by applying $180V_{rms}$, which corresponds to a birefringence of 4.79×10^{-5} at 1550nm as shown in Fig. 6.26. These results demonstrate that the device can act as a quarter-wave plate with 90° phase shift and a half-wave plate with 180° phase shift by applying different voltages. Full polarization control can be achieved by using three devices of this kind: two quarter-waveplates and one half-waveplate.

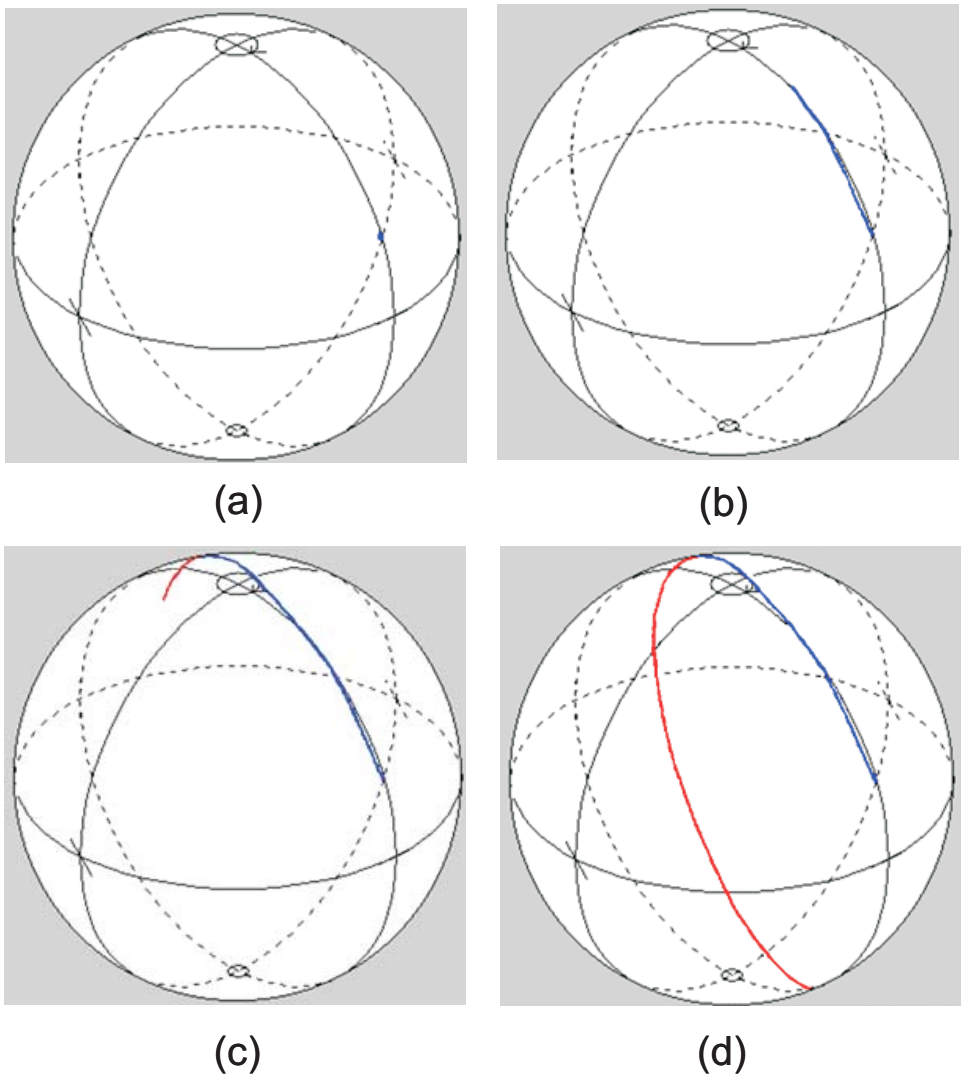

Figure 6.24: Induced phase shift on the Poincaré sphere when (a) $0V_{rms}$, (b) $60V_{rms}$, (c) $120V_{rms}$, (d) $180V_{rms}$ are applied to the LCPBG device.

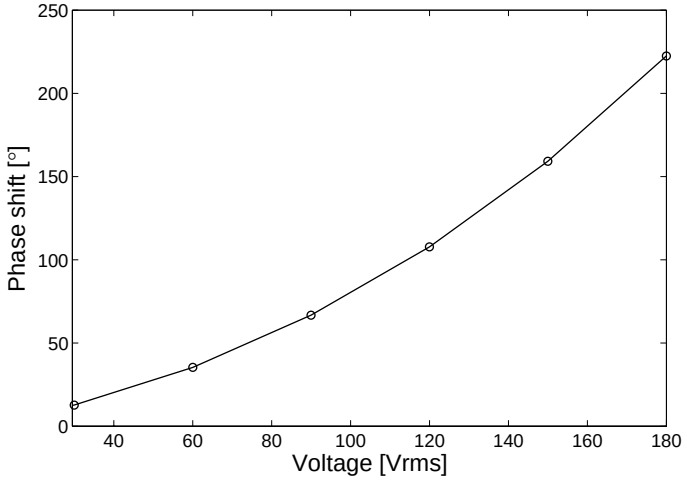

Figure 6.25: Electrically induced phase shift for different voltages at $30°C$.

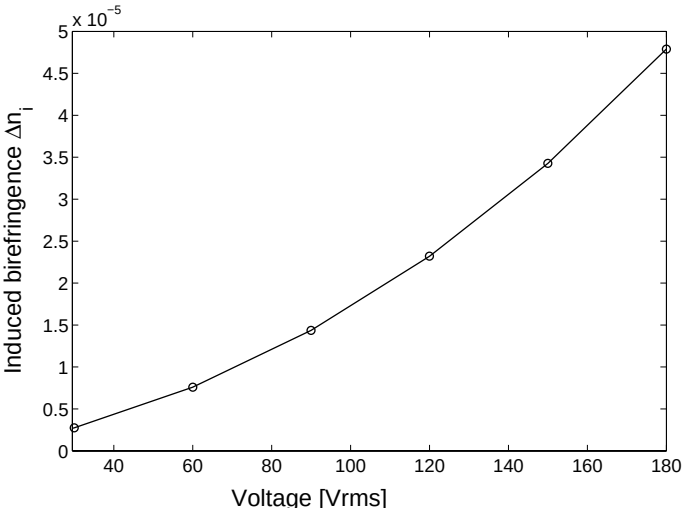

Figure 6.26: Induced birefringence as a function of voltage at $\lambda = 1550nm$.

6.5 Long-period gratings (LPGs) in LCPBG fibers

It is well known that an optical fiber consists of two waveguide structures, one being the high-index core surrounded by the lower-index cladding and the other being the cladding, surrounded by air. The cladding modes can be referred as Higher Order Modes (HOMs); they are weakly guided in the fiber and attenuates over a few centimeters. LPGs inscribed in optical fibers resonantly couple light from the core mode to copropagating HOMs. The coupling occurs at the resonance wavelength at which phase matching occurs between the core mode and the HOM. The resonance wavelength is given by [116]

$$\lambda_{res} = \Lambda_G(n_{eff,core} - n_{eff,HOM}) \tag{6.6}$$

where Λ_G is the period of the grating (pitch), $n_{eff,core}$ is the effective index of the core mode and $n_{eff,HOM}$ is the effective index of the HOM to which the core mode couples. The grating leads to a transfer of power from the core mode to HOMs. This results in a loss of power at the resonance wavelength, since the HOMs have a much higher loss than the fundamental core mode. Therefore, the resulting transmission spectrum present dips at the resonant wavelengths.

LPGs have a wide range of applications, among others optical filtering [117], gain equalization [118], mode conversion [119], temperature or strain sensors [120] and biochemical sensing [121]. LPGs have also been fabricated in index guiding PCFs [122–124] and, recently in PBG fibers [125, 126].

LPGs in PBG fibers were demonstrated by filling the microstructured cladding of a PCF with a high index liquid and inducing the LPG by applying a periodic pressure to the length of the fiber. In this way, narrow and tunable loss dips could be introduced in the transmission bands. Moreover, electrically tunable LPGs were realized in a single light guiding rod of LC [127] and in an index guiding fiber surrounded by an LC [128, 129].

In this section, mechanically and electrically induced LPGs in an LCPBG fiber are demonstrated. Both the mechanical and the electrical gratings have a high degree of tunability and the attenuation of the LPG can be varied by changing either the strength of the applied pressure or the electric field. For the electrical gratings, the advantage is that no mechanical stress is applied to the fiber, therefore enabling the fabrication of small highly

tunable fiber devices, that can easily be integrated into communication or sensor systems.

6.5.1 Mechanically-induced LPGs

The fiber used in this experiment was an LMA-10 (d=3.45μm, $\Lambda = 7.15\mu m$ and D=125μm, Crystal Fibre A/S, Denmark). The LC used was E7. Mechanical LPGs were realized in the LCPBG fiber by using a brass block with 26 periodically cut V-grooves. The spacing between the grooves (also called grating pitch) was $\Lambda_G = 800\mu m$. The LCPBG fiber device was positioned underneath the LPGs and pressure was applied to it, as shown in the schematic illustration of Fig. 6.27. The transmission of the fiber device was measured

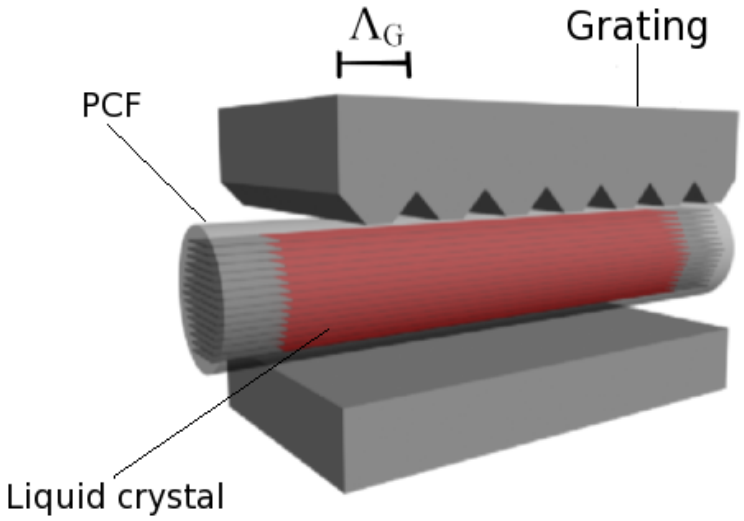

Figure 6.27: Schematic illustration of a LCPBG fiber underneath the brass grating used to induce the LPG in the fiber.

using white light from a Tungsten-Halogen light source coupled to the device through a piece of the same LMA fiber. An xyz-stage was used to couple the unfilled fiber to the filled one and the transmission was then measured with an optical spectrum analyzer, and normalized to that of an unfilled fiber. Fig. 6.28 shows the transmission of the LCPBG fiber when an increasing pressure is applied to the grating. The blue curve shows the transmission of the fiber when no pressure was applied. For an increasing pressure applied to

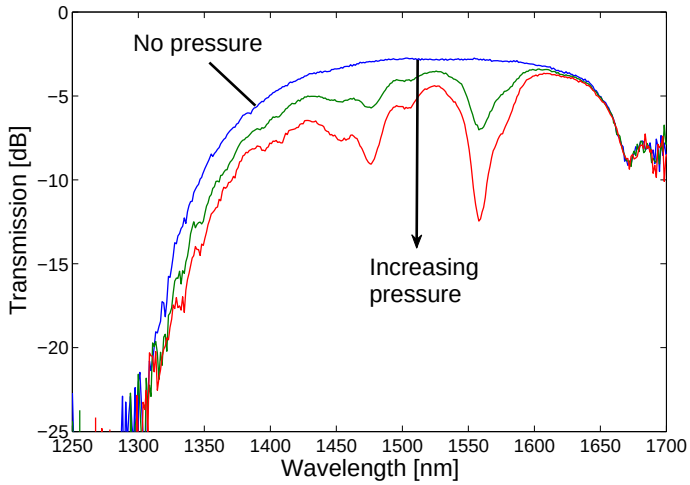

Figure 6.28: Transmission spectrum of the mechanically induced LPG in an LMA-10 filled with E7. The grating pitch is $\Lambda_G = 800\mu m$ and the transmission is measured at a temperature of $25°C$. The dips are caused by resonant coupling of the core mode with HOMs in the cladding.

the LCPBG fiber, loss dips appear in the bandgap centered around 1500nm, as illustrated with the green and red curve. Loss dips were not observed in the higher order bandgaps, except one at 1000nm. This dip (not shown in Fig. 6.28) was not observed when using a mechanical grating with a pitch less than $\Lambda_G = 800\mu m$ and is therefore attributed to a grating resonance. The higher order bandgaps are also slightly attenuated, probably because of stress caused to the fiber when the pressure is applied.

6.5.2 Electrically-induced LPGs

By using comb electrodes, a periodically varying electric field can be induced in the fiber. Since the LC reorients under the application of an electric field, this results in a periodic index variation along the length of the fiber. The principle is schematically illustrated in Fig. 6.29. In the figure, the alignment of the LC inside a single capillary tube placed under a comb electrode can be seen. In Fig. 6.29(a) the field is off and the LCs possess a planar alignment. In Fig. 6.29(b) the electric field is turned on and the LCs between the electrodes realign towards the direction of the electric field. Thereby, a pe-

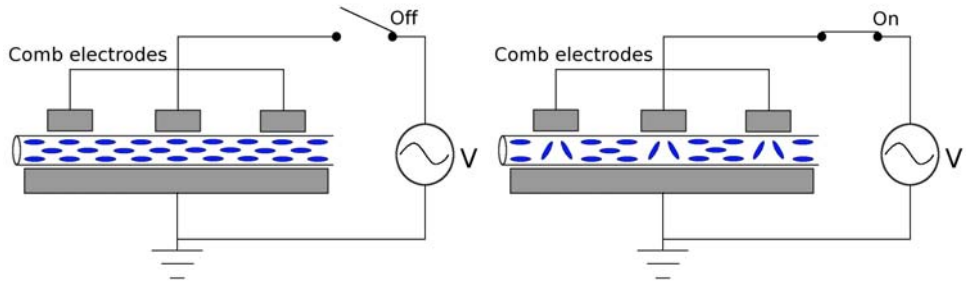

(a) (b)

Figure 6.29: Schematic illustration of a capillary filled with E7 and sandwiched between comb electrodes. In (a) no field is applied to the electrodes and the alignment is planer, while in (b) a voltage higher than the Fredericks transition threshold is applied to the electrodes, inducing a periodic index variation along the capillary.

riodic variation of the refractive index along the fiber is induced. The comb electrodes used in this work were made of a brass block with periodically cut V-grooves, as shown in Fig. 6.27. The electrical signal was generated by a signal generator and amplified by using a high voltage amplifier. In the experiment the coating of the fiber was removed and the frequency of the external field was 1kHz. The DC component of the electrical signal was removed using a high-pass filter and the signal was monitored on an oscilloscope. Fig. 6.30 shows the transmission bandgap around 1500nm, when a voltage is applied to the grating. The temperature was fixed to $25°C$ and no pressure was applied to the grating. Two distinct peaks are visible at a voltage of $43.8V_{rms}$. One at 1565nm and one at 1480nm. When the voltage is increased to $68.9V_{rms}$ two more dips appear, one at 1515nm and a small one at 1440 nm. The spectral positions of the loss dips are in good agreement with the observed transmission of the mechanically induced gratings. No memory effect of the gratings was observed, i.e. when the voltage was turned off, the grating dips completely disappeared. Although the dynamics of the grating device was not measured here, we believe that it is the same as described in [16] for plain electrodes.

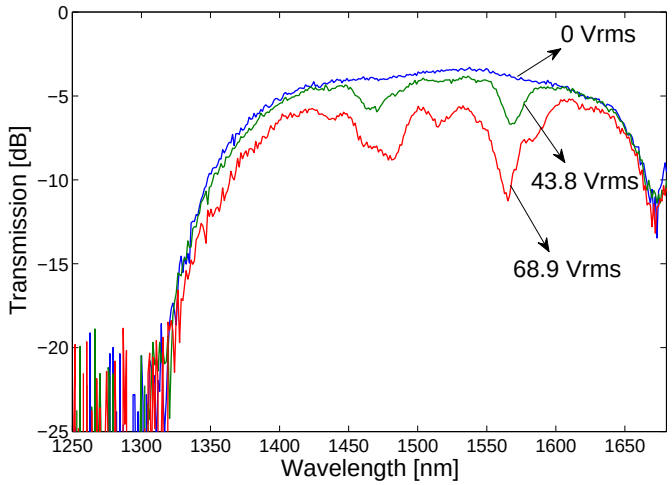

Figure 6.30: Transmission spectrum of the electrically induced LPG in a LMA-10 filled with E7. The grating pitch is $\Lambda_G = 800\mu m$ and the transmission is measured at a temperature of $25°C$. The dips are caused by resonant coupling of the core mode with HOMs in the cladding.

6.5.3 Thermal tunability

The temperature tuning for the E7-filled electrical grating is illustrated in Fig. 6.31, where the position of the dip with the highest loss is shown as a function of temperature. The loss peak moves towards shorter wavelengths when the temperature is changed from $25°C$ to $40°C$, and towards longer wavelengths from $40°C$ to $59°C$. E7 does not present a very high degree of tunability below $55°C$. The different direction of the shift for different temperatures can be explained by the change in the ordinary and extraordinary refractive indices of E7 as a function of temperature. These are shown in Fig. 6.32. The shift of the resonances is mainly determined by the ordinary refractive index, since the LC is planar oriented. Below $40°C$, the gradient of the ordinary index is almost zero, while the extraordinary index decreases as a function of the increase of temperature. Above $40°C$, the ordinary index starts to increase and, since the resonance wavelength is mostly affected by this, the resonances start to shift towards longer wavelengths. When the temperature approaches the clearing temperature of E7 the ordinary index increases rapidly and results in a larger degree of tuning observed in

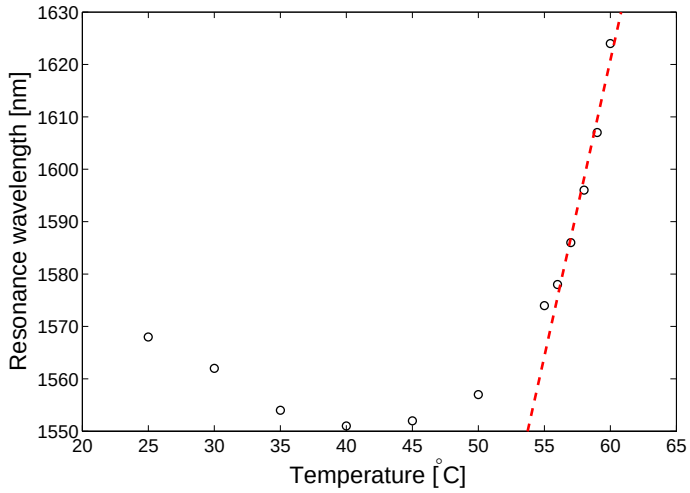

Figure 6.31: Temperature tuning of the electrically induced LPG in a LMA-10 filled with E7. A voltage of $63.6V_{rms}$ was applied to the device. Here the temperature dependence of one of the resonance wavelengths is shown.

Fig. 6.31. Using MDA-00-3969 instead, a linear tuning over a broader temperature interval can be achieved. Such a tuning is shown in Fig. 6.33, where a mechanical grating with a pitch of $\Lambda_G = 800\mu m$ was induced in a LMA-10 fiber filled with MDA-00-3969. A linear tuning of $-2.4nm/°C$ is observed. The linearity of the tuning is because its ordinary index is almost constant, whereas its extraordinary index decreases linearly (see Fig. 4.10).

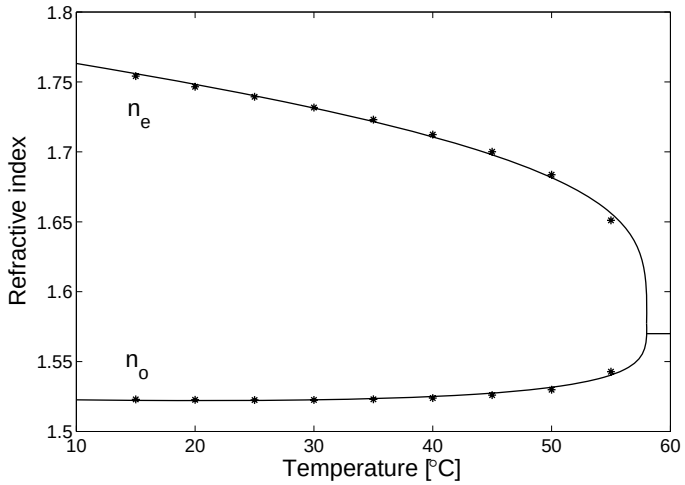

Figure 6.32: Temperature dependence of the extraordinary and ordinary refractive indices of E7 at $\lambda = 589nm$.

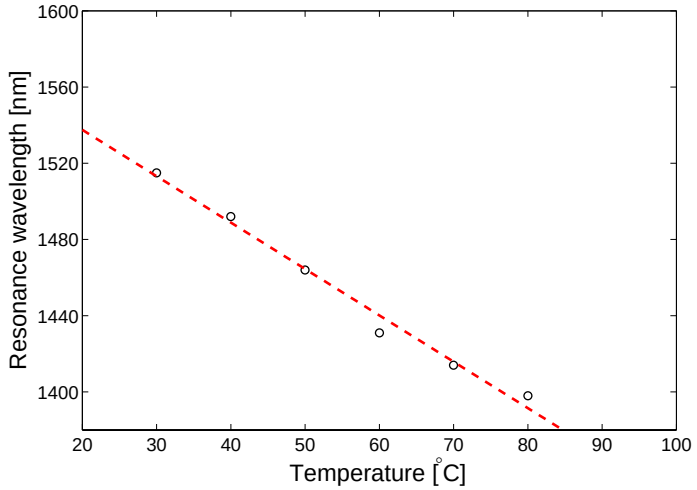

Figure 6.33: Temperature tuning of the mechanically induced LPG in a LMA-10 filled with MDA-00-3969.

6.5.4 Polarization sensitivity

The polarization sensitivity of the induced LPG in the E7-filled LMA-10 was investigated by launching linearly polarized light from a tunable laser source in the device. The wavelength of the laser was tuned to the wavelength of the loss dip induced by the LPG. By tuning the polarization of the input light with a polarization controller, the two polarizations which give the lowest and the highest transmission loss of the dip were found. The wavelength was then swept from 1520nm to 1620nm and the transmission was measured with an optical spectrum analyzer. The polarization dependence of both the electrically and the mechanically induced gratings is shown in Fig. 6.34 and Fig. 6.35, respectively. Both the electrical and mechanical gratings show a high dependence of the transmission with respect to the polarization of the light launched into the grating. For the electrically tunable gratings, with an applied voltage of $68.9V_{rms}$, the difference between the maximum transmission and the minimum at the wavelength of the dip is 12.5dB, as shown in Fig. 6.34. The reason for this is that light polarized in the same direction as the applied electric field will experience a higher perturbation of the refractive index along the LPG, due to the fact that the LC is oriented in this direction. This results in a stronger coupling to the HOM and, therefore, in a higher transmission loss for this polarization. The spectral position of the loss dip is also shifted slightly for the two polarizations. This is because the applied electric field induces a slight birefringence in the fiber, giving rise to a slight shift in the resonance wavelength for the two polarizations. The mechanically induced grating also shows a high degree of polarization dependence. A difference of 5dB between the minimum and the maximum transmission at the dip were observed. The resonance wavelength for the mechanically induced gratings was also slightly shifted for the two polarizations. This is again due to the grating inducing a birefringence in the fiber.

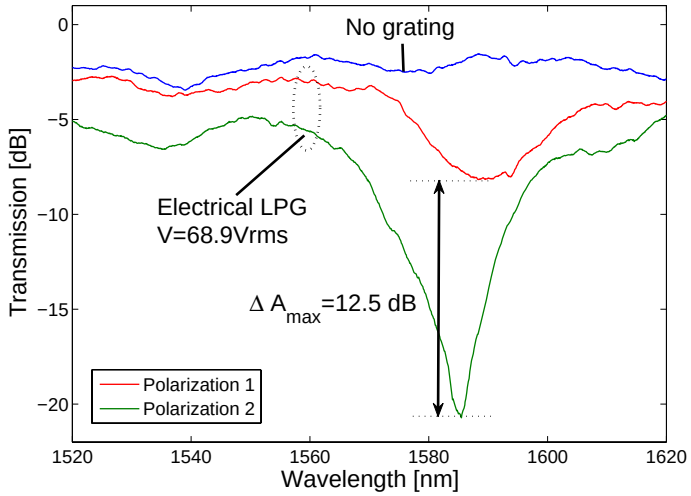

Figure 6.34: Polarization sensitivity of the electrical LPG induced in the E7-filled LMA-10.

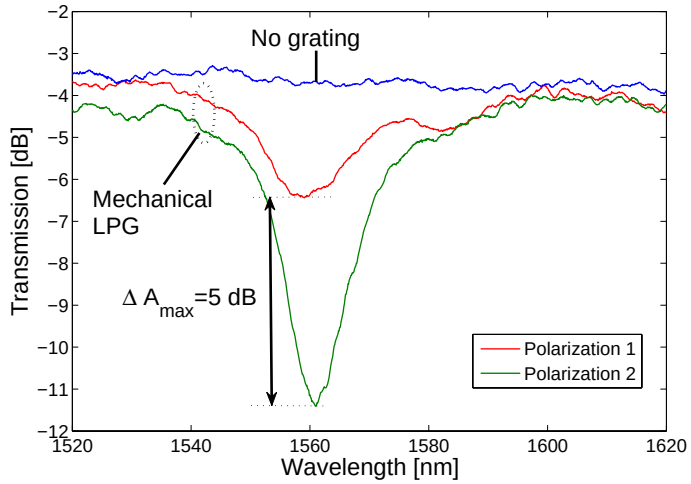

Figure 6.35: Polarization sensitivity of the mechanical LPG induced in the E7-filled LMA-10.

6.6 Summary

In this chapter various devices based on LCPBG fibers were demonstrated. A tunable bandwidth bandpass filter based on two different LCs and a PM filter with a PER of 14dB were illustrated. Finite Element Method (FEM) simulations were carried out in order to support the experimental results. A study about PCFs filled with nanoparticle-doped LC demonstrated frequency tunability and opened up the possibility to use this kind of device as a gain equalization filter. Tunable waveplates were also fabricated by using various types of LCs. Finally, LPGs were realized in LCPBG fibers and the possibility of tuning these gratings was investigated by mechanical, electrical or thermal tuning.

Chapter 7

Applications of LCPBG devices

In the previous chapters, various Liquid Crystal Photonic Bandgap (LCPBG) fiber devices were illustrated and suggestions regarding possible applications were given.

As a conclusion of this work, an experiment that demonstrates the suitability of these new devices to be used in optical communication systems is presented. An LCPBG fiber device which filters the Amplified Spontaneous Emission (ASE) noise caused by Erbium Doped Fiber Amplifiers (EDFAs) is fabricated and inserted in an optical communication system in order to evaluate its performance. The fiber and the Liquid Crystal (LC) are chosen such that the transmission spectrum of the LCPBG fiber device displays a minimum around 1530nm, that is the wavelength at which the ASE noise peak is often observed. Despite a loss of 5dB, the benefits of the filtering are dramatic. In fact, by using the LCPBG filter, the transmission distance was extended by a factor of 4 from 400km to 1600km.

This chapter describes briefly the problem of ASE noise in an optical communication system, discusses about the design and fabrication of the LCPBG filter used in the experiment and gives a detailed description of the setup used to carry out the experiments. Finally the performances of the system in terms of Optical Signal-to-Noise Ratio (OSNR) when no filtering is used and when the LCPBG filter is inserted in the system are obtained and compared. A short summary is given at the end of the chapter.

7.1 Noise filtering in a multi-channel system

7.1.1 ASE noise in a transmission system

In an optical transmission system, there is often the need to transmit information over longer distances while still keeping the signal in the optical domain. This can be done introducing EDFAs in the link to amplify the attenuated signal. The performance improvement introduces also a price to pay. Noise is, in fact, generated in the EDFAs and accumulates in the optical transmission line. Noise in the signal band can embezzle gain from the signal wavelengths and through amplifier cascading the problem increases and eventually leads to the EDFAs being saturated by noise while the channel power decreases below noise level [130, 131]. This problem is generally overcome by using Gain Flattening Filters (GFFs) [132, 133]. Alternatively, the out-of-band noise can be removed in reconfigurable optical add-drop multiplexers. An LCPBG fiber device was used to filter this noise and a study of the performances of this filter was carried out. The LC and the fiber were chosen such that the transmission spectrum displayed a minimum at about 1530nm, which corresponds to the peak of the ASE noise [134].

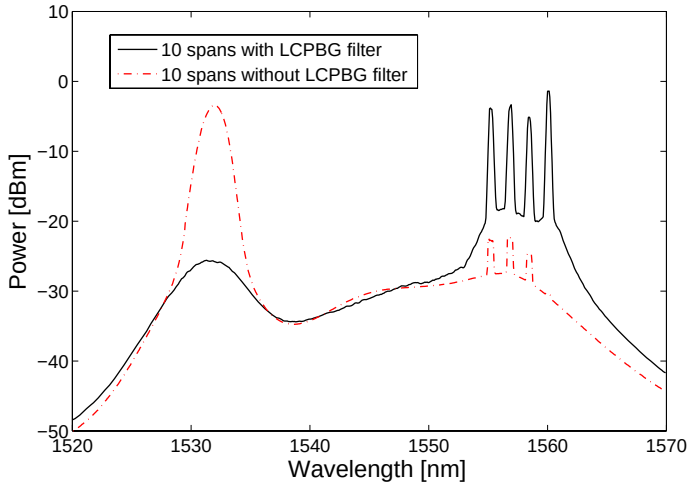

Figure 7.1: Optical power spectrum after 10 spans with and without the LCPBG filter. Without filtering, a large ASE peak was created at 1530nm and the signals drowned in noise.

The buildup of an ASE peak is illustrated in Fig. 7.1 where four channels were transmitted 10 spans of each 65 km and where the signals were amplified after each span using EDFAs. The dotted line illustrates a situation when the signals were amplified after each span without noise filtering. As one can see the OSNR dropped below any acceptable limit and the signals were unrecoverable. In particular, the channel at the longest wavelength completely disappeared below the noise level (Fig. 7.1, red curve). This happened as the EDFAs saturated from the great amount of power concentrated in the noise peak, leaving behind the channels with a highly reduced gain. In the example above, the optical power into each of the amplifiers receiving the signal was -12 dBm. If, instead, an LCPBG filter was inserted at the amplification points, the noise power was reduced considerably (Fig. 7.1, black/full-line curve) and the channels showed an OSNR higher than 15dB after the same distance, which is enough for error free detection assuming that a Forward Error Correction (FEC) scheme is used. In this example, the filter temperature was $11.8°C$. Fig. 7.2 shows the transmission spectrum of the filter in the wavelength range 1520-1620nm and for three different temperatures.

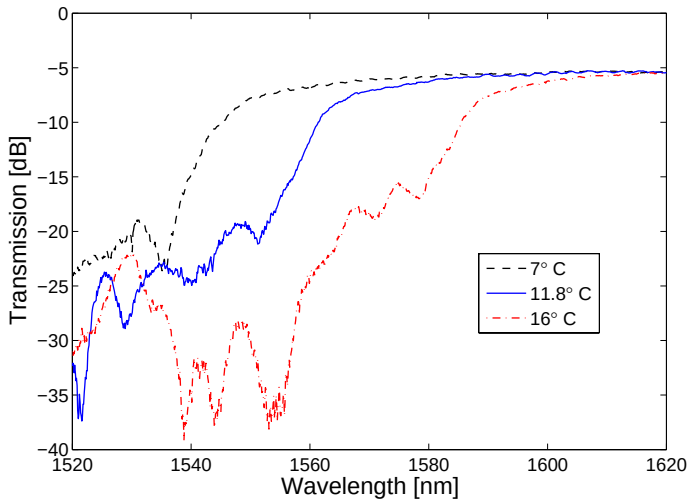

Figure 7.2: Transmission spectrum of the LCPBG filter for three different temperatures. The length of the PCF is 50cm and the LC infiltrated region is 10mm.

7.1.2 Setup

A piece of 50 cm PCF fiber (Large-Mode-Area (LMA)-13, d=4.3μm, Λ=8.5μm and D=125μm) was filled by using capillary forces, for approximately 10mm, with a custom made high birefringence LC designated as UCF1 [62, 135] and mechanically spliced to a standard Single Mode Fiber (SMF) by using a silica ferrule. A few drops of UV curable polymer were poured around the ferrule and UV cured in order to give mechanical stability to the device. At room temperature, the minimum of the lower bandgap was at 1620nm. In order to have this minimum at 1530nm, where the ASE peak is, cooling of the LC was necessary. Therefore, the filter was mounted on a Peltier element in order to decrease the temperature of the LC and provide thermal tunability to the transmission spectrum. Thermal paste was inserted between the Peltier module and the LCPBG fiber device in order to have better thermal conductivity. The filter fabricated for this application allowed full tunability over the C- and L-band. The tunability is useful in both the perspective of assuring maximum suppression of the ASE noise but also to optimize the gain equalization features provided by the filter.

The setup used to experimentally demonstrate the effect of noise filtering and gain equalization using the LCPBG fiber device is shown in Fig. 7.3. Four Laser Diodes (LDs) were used to produce four channels in the spectral range from 1555nm to 1560nm. After amplification the channels were transmitted to the loop controller which filled up a loop consisting of 44km of SMF, two EDFAs amplifiers and the LCPBG filter. The configuration with two amplifiers is common in transmission systems where dispersion compensation is necessary and thus used to overcome the loss in the Dispersion Compensating Fiber (DCF). In this case no DCFs have been inserted in the system as there was no data modulation on the channels. Data modulation is not necessary since we are using OSNR to evaluate the performances of the filter and OSNR is not influenced by chromatic dispersion. Although not using any DCF modules, the double-amplifier configuration was applied in order to have more freedom in terms of power-variation when evaluating the device. Noise, on the other hand, has a direct impact on the OSNR and thus makes it an ideal evaluation parameter for the demonstration of the usability of the LCPBG filter.

The LCPBG filter was inserted between the two EDFAs called A and

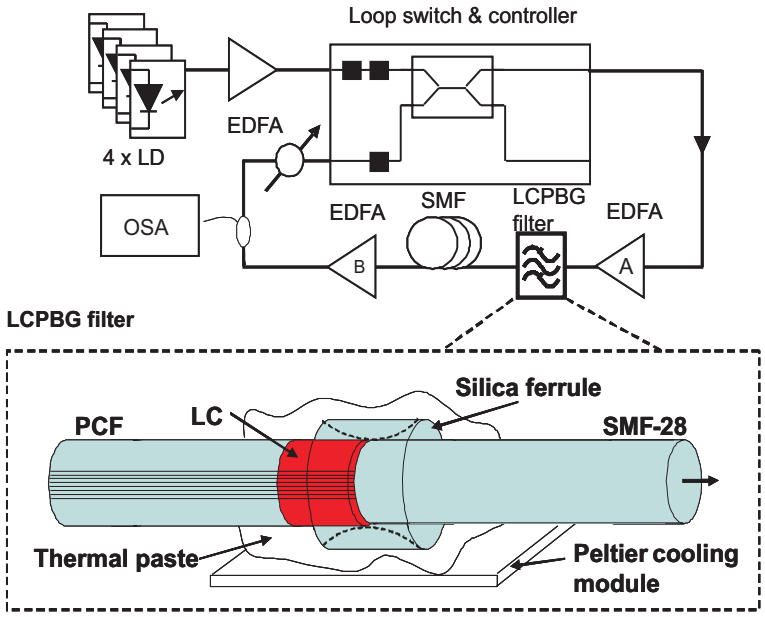

Figure 7.3: Setup used to investigate the benefits of a LCPBG fiber device as a noise filter in an optical transmission system. The enlargement represents the structure of the LCPBG filter.

B, as depicted in Fig. 7.3. With an insertion loss of only 5dB the LCPBG filter does not contribute strongly to the total losses of the system. An optical attenuator was placed after the SMF and used to vary the input power to EDFA A and thus simulate changing lengths of the transmission fiber. An optical spectrum analyzer inserted in the loop is used in order to evaluate the OSNR of the signals after a pre-selected number of round trips (spans) in the loop. By triggering the optical spectrum analyzer with the switching signals from the loop controller any number of round trips can be selected.

7.1.3 Experimental results

A set of experiments was carried out by using this setup in order to experimentally validate the effect of noise filtering using the LCPBG high pass filter.

In the first experiment the number of loops was fixed to 10 spans

while the span-length was varied from 10km to 85km corresponding to a span loss between 3dB and 18dB. This was done for both the case without filtering and with the LCPBG filter at each span. Results are shown in Fig. 7.4 where the two curves represent the average OSNR value of all channels for each case. First of all, one can see from this figure that the filter has little or no positive effect when the span loss becomes less than 8dB (40km). When the span loss is less than 8dB there is not enough noise generated for the LCPBG filter effect to be effective. Instead the use of the filter leads to excess noise due to its insertion loss and this in turn leads to a 3dB OSNR penalty. If the losses exceed 8dB (40km of SMF) the situation changes as the filter now becomes effective in reducing the noise peak at 1530 nm. If a limit at OSNR=10dB is considered (corresponding to a Bit Error Rate (BER) of minimum 1×10^{-9} using a proper FEC coding at a bit rate of 10Gbit/s) the improvement from using the filter is a 7dB increase in maximum span loss. Thus the span length can be increased by 35km compared to the situation without the LCPBG filter. Alternatively, if a fixed span length of, for example, 65km is specified, a system without the filter would have an OSNR of 5dB whereas, using the LCPBG filter, the same system would achieve an OSNR of 15dB.

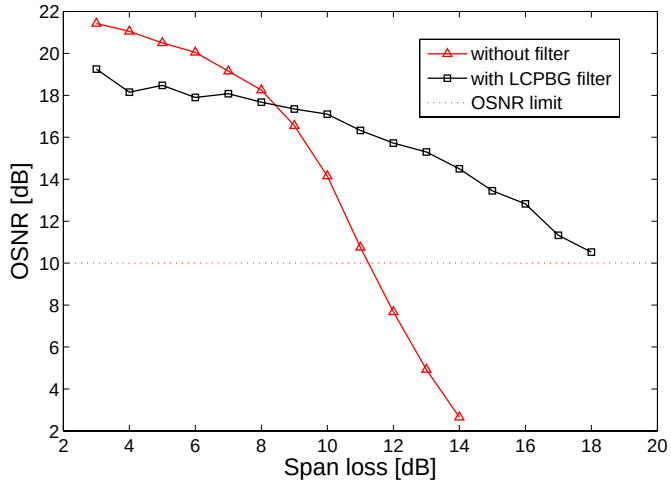

Figure 7.4: OSNR versus span-loss when no filter is inserted in the transmission spectrum and when the LCPBG filter is used. The number of transmitted spans was fixed at 10.

In the second experiment the span length was fixed to 80km corresponding to a span loss of 16dB. While keeping the span loss constant, the number of transmitted spans was increased and the OSNR of all the channels evaluated after each span. This was done for both the case without filtering and with the LCPBG filter inserted at each span. Results are shown in Fig. 7.4 where the two curves again represent the average OSNR value of all channels for each case. One can see from the results that with a fixed span length of 80km, the LCPBG filter has a beneficial effect on the OSNR for any number of spans. Without a filter, the OSNR performance is very poor as the OSNR drops below 10dB already after 5 spans. If the LCPBG filter is inserted, the maximum transmission increases to at least 20 spans, a significant improvement of 15 spans or 1200km. Thus, in this example the LCPBG filter enables transmission distances over four times as long.

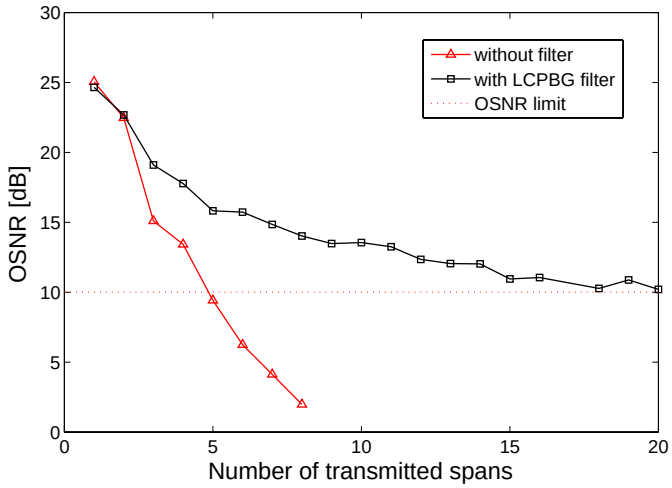

Figure 7.5: OSNR versus number-of-spans when no filter is inserted in the transmission spectrum and when the LCPBG filter is used. Each span has a fixed length of 80km.

7.2 Summary

In this chapter an experiment that demonstrates the suitability of LCPBG fiber devices to be used in optical communication systems was described. An

LCPBG fiber device filtering the ASE noise caused by EDFAs was fabricated and inserted in an optical communication system in order to evaluate its performance. It was demonstrated that, by using this, the transmission distance was extended by a factor of 4 from 400km to 1600km.

Chapter 8

Conclusion

This thesis has demonstrated various devices based on Liquid Crystal Photonic Bandgap (LCPBG) fibers and addressed several applications of them.

Photonic Crystal Fibers (PCFs) are waveguides with a cross-section consisting typically of an air/silica microstructure that is invariant along the fiber axis. The microstructure allows the realization of either the so-called high-index guiding fibers, which guide light in a high-index core similarly to the Total-Internal-Reflection (TIR) principle, or the so-called Photonic BandGap (PBG) fibers, which guide light in a low-index core by means of coherent reflections from the surrounding periodic structure. These fibers have attracted a lot of interest around the world as they possess unique properties. Furthermore, the presence of air holes in the structure gives the possibility to infuse liquids and, therefore, to create tunable devices. *Eggleton et al.* in 2001 was the first to demonstrate that tunable devices, e.g. tunable gratings and tunable birefringence controllers, could be fabricated by infiltrating polymers in a special type of PCFs. Later, in 2002, *Bise et al.* demonstrated that it was possible to transform a high-index core PCF into a PBG fiber by infiltrating a high-index liquid into it. The bandgaps of this fiber could be tuned by tuning the temperature of the liquid. In 2003 *Alkeskjold et al.* proposed to fill index-core PCFs with Liquid Crystals (LCs). Among liquids, LCs represent a very good candidate for the fabrication of tunable all-in-fiber devices because they can exhibit very high electro-optic and thermo-optic effects due to high birefringence (up to $\Delta n = 0.8$) and high dielectric anisotropy (up to $\Delta\varepsilon = 70$). Thermal,

electrical and optical control was achieved.

This thesis has demonstrated various devices based on LCPBG fibers and their feasibility to be used in optical transmission systems.

Gaussian filters which may find application in Optical Coherence Tomography (OCT) have been demonstrated. These filters were fabricated by tapering PCFs and, successively, filling them with LCs, in order to smooth the transmission spectrum. A filter centered at 1400nm with a 3-dB bandwidth of 180nm was presented. This filter had insignificant tunability as the LC adopted was poorly tunable. Another filter centered at 1062nm, with a 3-dB bandwidth of 150nm was achieved. This filter showed a tunability of 80nm in the temperature range $30°C - 60°C$. Gaussian filters based on PCFs infiltrated with oils were also fabricated and showed a higher 3-dB bandwidth of 250nm. The tunability was 117nm in the temperature range $25°C - 60°C$

A bandpass filter with a continuously tunable bandwidth has been demonstrated. The filter has been fabricated by using two different LCs infiltrated in a PCF, offering more flexible bandwidth tunability compared to a fiber infiltrated with one LC. $130nm$ bandwidth tunability has been achieved by tuning the temperature from $30°C$ to $90°C$.

An all-in-fibre Polarization Maintaining (PM) filter has also been demonstrated by infiltrating a PM PCF with LC. A Polarization Extinction Ratio (PER) of 14dB at 1550nm has been measured, opening up the possibility of using this type of devices as PM filters, for example, in the fabrication of fibre lasers. Tunability has also been explored and a wavelength shift of 250nm has been measured in the temperature range $30°C - 70°C$.

Furthermore, nanoparticle-doped LCs have been studied and led to interesting results. A device based on a PCF infiltrated with $BaTiO_3$ nanoparticles has been proposed. Compared to similar devices based on undoped LCs, new interesting features appear, such as a frequency modulation response and a transmission spectrum with tunable attenuation on the short wavelength side of the bandgap. This suggests a potential application of this device as a tunable all-in-fiber gain equalization filter with an adjustable

slope. The frequency dependence of the $BaTiO_3$ nanoparticle-doped LC mixture has also been investigated in a silica capillary and in a glass cell and shows an analogous behavior to the one observed in a PCF.

Tunable waveplates have been fabricated, based on different types of LCs. By using a dual-frequency LC, a birefringence of 3×10^{-5} has been induced by applying a voltage of $82V_{rms}$, which corresponds to a $\lambda/6$ waveplate at 1600nm. By using a negative dielectric anisotropy LC, a phase shift of 222.5° can be obtained by applying $180V_{rms}$, which corresponds to a birefringence of 4.79×10^{-5}. With this LC, $\lambda/4$ and $\lambda/2$ waveplates have been demonstrated.

More exotic components, such as electrically and mechanically induced Long-Period Gratings (LPGs) in LCPBG fibers have also been demonstrated. The strength of the gratings can be tuned by varying the pressure, in case of mechanical gratings, and by varying the strength of the applied electric field, in case of electrical gratings. The resonance wavelengths can be tuned by temperature, and a very high degree of tuning, up to $11nm/°C$, has been demonstrated. A linear tuning of $-2.4nm/°C$ over a broad temperature interval from $30°C$ to $80°C$ has also been demonstrated. Furthermore, the polarization dependence of the induced gratings has been investigated and a strong polarization dependence was observed.

Finally, an LCPBG fiber device has been inserted in a multi-channel transmission system. The transmission spectrum of the LCPBG filter displayed a minimum that was ideal for removing the Amplified Spontaneous Emission (ASE) noise peak at 1530nm caused by Erbium Doped Fiber Amplifiers (EDFAs). Despite an insertion loss of 5dB, the benefit of the LCPBG filter was dramatic. The Optical Signal-to-Noise Ratio (OSNR) improvement resulting from the use of the filter has been measured. Using this filter, the transmission distance has been extended by a factor of 4 from 400km to 1600km. This is the first application, to our knowledge, of an LCPBG fiber device working in an optical transmission system.

The success of the above mentioned experiments shows a promising future of LCPBG fiber devices. These have been shown to have very interesting properties and useful characteristics. This study opens up the possibility for further work focused, amongst other things, on applications

of these LCPBG devices in real systems.

8.1 Future work

This thesis has focused on the development of LCPBG fiber devices which can be used in optical systems.

Work on the packaging of these components is in progress in our group and it is very critical, since arc-fusion splicing can not be achieved due to LC residues on the end facet of the fiber. Instead, other techniques such as self aligning V-grooves equipped with electrodes can be used [136].

A better understanding of the alignment of LCs in silica capillary is required in order to have a more clear picture of the physics behind LCs contained in cylindrical geometries. Many factors, e.g. dielectric anisotropy, elastic constants, rigidity, dipole of the molecules and quality of the glass determine the alignment, but it is difficult to separate the contribution from each term and determine the alignment "a priori", given the characteristics of the LC.

Furthermore, more system experiments need to be conducted, for example gain-equalization filters, PM filters, waveplates and notch filter need to be tested in real systems. Their performances need to be determined. Gaussian filters need also to be tested in an OCT system.

Finally, the long-term stability of these devices needs to be tested.

Acronyms

LC Liquid Crystal

TFT Thin-Film-Transistor

LCD Liquid Crystal Display

POM Polarized Optical Microscopy

PCF Photonic Crystal Fiber

MOF Microstructured Optical Fiber

PER Polarization Extinction Ratio

LCPBG Liquid Crystal Photonic Bandgap

LMA Large-Mode-Area

SMF Single Mode Fiber

TIR Total-Internal-Reflection

M-TIR Modified-Total-Internal-Reflection

PBG Photonic BandGap

HNA High-Numerical-Aperture

HNL Highly-Non-Linear

LIC Low-Index Core

HC Hollow-Core

FEM Finite Element Method

PDE Partial Differential Equation

PML Perfectly Matching Layer

SEM Scanning Electron Micrograph

PDL Polarization Dependent Loss

PMD Polarization Mode Dispersion

FSM Fundamental Space-Filling Mode

BPM Beam Propagation Method

PML Perfect Matching Layers

OCT Optical Coherence Tomography

WDM Wavelength-Division Multiplexing

ASE Amplified Spontaneous Emission

EDFA Erbium Doped Fiber Amplifier

GFF Gain Flattening Filter

OSNR Optical Signal-to-Noise Ratio

LD Laser Diode

DCF Dispersion Compensating Fiber

BER Bit Error Rate

FEC Forward Error Correction

PM Polarization Maintaining

PER Polarization Extinction Ratio

HNA High Numerical Aperture

ITO Indium-Tin-Oxide

LPG Long-Period Grating

HOM Higher Order Mode

NA Numerical Aperture

Bibliography

[1] D. Gloge, "Weakly guiding fibers," Applied Optics **10**(10), 2252–2258 (1971).

[2] D. Marcuse, *Light transmission optics.* (Van Nostrand Reinhold, 1983).

[3] D. Marcuse, *Theory of dielectric optical waveguides.* (Academic Press, 1991).

[4] J. Knight, J. Broeng, T. A. Birks, and P. Russell, "Photonic band gap guidance in optical fibers," Science **282**(5393), 1476–1478 (1998).

[5] J. Knight, T. Birks, P. St.J. Russell, and D. Atkin, "All-silica single-mode optical fiber with photonic crystal cladding," Optics Letters **21**(19), 1547–1549 (1996).

[6] P. Russell, "Photonic crystal fibers," Science **299**(5605), 358–362 (2003).

[7] T. Birks, J. Knight, and P. Russell, "Endlessly single-mode photonic crystal fiber," Optics Letters **22**(13), 961–963 (1997).

[8] J. Ranka, R. Windeler, and A. Stentz, "Visible continuum generation in air-silica microstructure optical fibers with anomalous dispersion at 800 nm," Optics Letters **25**(1), 25–27 (2000).

[9] J. Limpert, T. Schreiber, S. Nolte, H. Zellmer, A. Tunnermann, R. Iliew, F. Lederer, J. Broeng, G. Vienne, A. Petersson, and C. Jakobsen, "High-power air-clad large-mode-area photonic crystal fiber laser," Optics Express **11**(7), 818–823 (2003).

[10] R. Bise, R. Windeler, K. Kranz, C. Kerbage, B. Eggleton, and D. Trevor, "Tunable photonic band gap fiber," Optical Fiber Communication Conference OFC 2002 pp. 466–468 (2002).

[11] P. Westbrook, B. Eggleton, R. Windeler, A. Hale, T. Strasser, and G. Burdge, "Cladding-mode resonances in hybrid polymer-silica microstructured optical fiber gratings," IEEE Photonics Technology Letters **12**(5), 495–497 (2000).

[12] B. Eggleton, C. Kerbage, P. Westbrook, R. Windeler, A. Hale, and B. Eggleton, "Microstructured optical fiber devices," Optics Express **9**(13), 698–713 (2001).

[13] C. Kerbage, B. Eggleton, and B. Eggleton, "Numerical analysis and experimental design of tunable birefringence in microstructured optical fiber," Optics Express **10**(5), 246–255 (2002).

[14] T. Larsen, A. Bjarklev, and D. Hermann, "Optical devices based on liquid crystal photonic bandgap fibers," Optics Express **11**(20) (2003).

[15] T. R. Wolinski, K. Szaniawska, S. Ertman, P. Lesiak, A. W. Domanski, R. Dabrowski, E. Nowinowski-Kruszelnicki, and J. Wojcik, "Influence of temperature and electrical fields on propagation properties of photonic liquid-crystal fibres," Measurement Science and Technology **17**(5), 985–991 (2006).

[16] M. Haakestad, T. Alkeskjold, M. Nielsen, L. Scolari, J. Riishede, H. Engan, and A. Bjarklev, "Electrically tunable photonic bandgap guidance in a liquid-crystal-filled photonic crystal fiber," IEEE Photonics Technology Letters **17**(4), 819–821 (2005).

[17] F. Du, Y.-Q. Lu, and S.-T. Wu, "Electrically tunable liquid-crystal photonic crystal fiber," Applied Physics Letters **85**(12), 2181–2183 (2004).

[18] L. Scolari, T. T. Alkeskjold, J. Riishede, A. Bjarklev, D. S. Hermann, Anawati, M. D. Nielsen, and P. Bassi, "Continuously tunable devices based on electrical control of dual-frequency liquid crystal filled photonic bandgap fibers," Optics Express **13**(19), 7483–7496 (2005).

[19] T. Alkeskjold, J. Laegsgaard, A. Bjarklev, D. Hermann, Anawati, J. Broeng, J. Li, and S.-T. Wu, "All-optical modulation in dye-doped nematic liquid crystal photonic bandgap fibers," Optics Express **12**(24) (2004).

[20] J. Lægsgaard, "Gap formation and guided modes in photonic bandgap fibres with high-index rods," Journal of Optics A: Pure and Applied Optics **6**(8), 798–804 (2004).

[21] J. Lægsgaard and T. Alkeskjold, "Designing a photonic bandgap fiber for thermo-optic switching," Journal of the Optical Society of America B: Optical Physics **23**(5), 951–957 (2006).

[22] J. Sun, C. Chan, and N. Ni, "Analysis of photonic crystal fibers infiltrated with nematic liquid crystal," Optics Communications **278**(1), 66–70 (2007).

[23] D. Zografopoulos, E. Kriezis, and T. Tsiboukis, "Tunable highly birefringent bandgap-guiding liquid-crystal microstructured fibers," Journal of Lightwave Technology **24**(9), 3427–3432 (2006).

[24] J. Weirich, J. Lægsgaard, L. Scolari, L. Wei, T. T. Alkeskjold, and A. Bjarklev, "Biased liquid crystal infiltrated photonic bandgap fiber," Optics Express **17**(6), 4442–4453 (2009).

[25] L. Scolari, T. Alkeskjold, and A. Bjarklev, "Gaussian filtering with tapered liquid crystal photonic bandgap fibers," Proceedings of IEEE Lasers and Electro-Optics Society Annual Meeting LEOS 2006 pp. 829–830 (2006).

[26] L. Scolari, T. Alkeskjold, and A. Bjarklev, "Tunable Gaussian filter based on tapered liquid crystal photonic bandgap fibre," Electronics Letters **42**(22), 1270–1271 (2006).

[27] A. Brunetti, L. Scolari, J. Weirich, L. Eskildsen, G. Bellanca, P. Bassi, and A. Bjarklev, "Gaussian filtering with tapered oil-filled photonic bandgap fibers," Proceedings of 1st Workshop on Specialty Optical Fibers and Their Applications WSOF 2008 pp. 113–116 (2008).

[28] L. Scolari, G. Tartarini, E. Borelli, T. Alkeskjold, H. Hansen Mulvad, P. Bassi, and A. Bjarklev, "Tunable Bandpass Filter based on Photonic Crystal Fiber filled with Multiple Liquid Crystals," Proceedings of

IEEE Lasers and Electro-Optics Society Annual Meeting LEOS 2007 pp. 319–320 (2007).

[29] L. Scolari, C. Olausson, J. Weirich, D. Turchinovich, T. Alkeskjold, A. Bjarklev, and L. Eskildsen, "Tunable polarisation-maintaining filter based on liquid crystal photonic bandgap fibre," Electronics Letters **44**(20), 1189–1190 (2008).

[30] L. Scolari, S. Gauza, H. Xianyu, L. Zhai, L. Eskildsen, T. Alkeskjold, S.-T. Wu, and A. Bjarklev, "Frequency tunability of solid-core photonic crystal fibers filled with nanoparticle-doped liquid crystals," Optics Express **17**(5), 3754–3764 (2009).

[31] L. Wei, L. Eskildsen, J. Weirich, L. Scolari, T. Alkeskjold, and A. Bjarklev, "Continuously tunable all-in-fiber devices based on thermal and electrical control of negative dielectric anisotropy liquid crystal photonic bandgap fibers," Applied Optics **48**(3), 497–503 (2009).

[32] D. Noordegraaf, L. Scolari, J. Lægsgaard, L. Rindorf, and Alkeskjold, "Electrically and mechanically induced long period gratings in liquid crystal photonic bandgap fibers," Optics Express **15**(13), 7901–7912 (2007).

[33] M. Petersen, L. Scolari, T. Tokle, T. Alkeskjold, S. Gauza, S.-T. Wu, and A. Bjarklev, "Noise filtering in a multi-channel system using a tunable liquid crystal photonic bandgap fiber," Optics Express **16**(24), 20,067–20,072 (2008).

[34] E. Yablonovitch, "Inhibited spontaneous emission in solid-state physics and electronics," Physical Review Letters **58**(20), 2059–2062 (1987).

[35] S. John, "Strong localization of photons in certain disordered dielectric superlattices," Physical Review Letters **58**(23), 2486–2489 (1987).

[36] J. Broeng, *Photonic crystal fibers* (PhD thesis, Technical University of Denmark, Denmark, 1999).

[37] S. E. B. Libori, *Photonic crystal fibers -from theory to practice* (PhD thesis, Technical University of Denmark, Denmark, 2002).

[38] T. Monro, P. Bennett, N. Broderick, and D. Richardson, "Holey fibers with random cladding distributions," Optics Letters **25**(4), 206–208 (2000).

[39] A. Snyder and J. Love, *Optical waveguide theory* (Chapman and Hall, 1984).

[40] T. Birks and Y. Li, "The shape of fiber tapers," Journal of Lightwave Technology **10**(4), 432–438 (1992).

[41] J. Broeng, D. Mogilevstev, S. E. Barkou, and A. Bjarklev, "Photonic Crystal Fibers: A New Class of Optical Waveguides," Optical Fiber Technology **5**(3), 305–330 (1999).

[42] http://www.crystal fibre.com/ .

[43] N. Venkataraman, M. Gallagher, C. Smith, D. Muller, J. West, K. Koch, and J. Fajardo, "Low Loss (13 dB/km) Air Core Photonic Band-Gap Fibre," 28th European Conference on Optical Communication ECOC 2002 **5**, 1–2 (2002).

[44] S. G. Johnson and J. Joannopoulos, "Block-iterative frequency-domain methods for Maxwell's equations in a planewave basis," Optics Express **8**(3), 173–190 (2001).

[45] D. Noordegraaf, *Long period gratings in liquid crystal photonic bandgap fibers* (M.Sc. thesis, Technical University of Denmark, Denmark, 2006).

[46] T. Alkeskjold, *Optical devices based in liquid crystal photonic bandgap fibers* (PhD thesis, Technical University of Denmark, Denmark, 2005).

[47] N. Litchinitser, A. Abeeluck, C. Headley, and B. Eggleton, "Antiresonant reflecting photonic crystal optical waveguides," Optics Letters **27**(18), 1592–1594 (2002).

[48] A. Abeeluck, N. Litchinitser, C. Headley, and B. Eggleton, "Analysis of spectral characteristics of photonic bandgap waveguides," Optics Express **10**(23), 1320–1333 (2002).

[49] N. Litchinitser, S. Dunn, B. Usner, B. Eggleton, T. White, R. McPhedran, and C. de Sterke, "Resonances in microstructured optical waveguides," Optics Express **11**(10), 1243–1251 (2003).

[50] N. Litchinitser, S. Dunn, P. Steinvurzel, B. Eggleton, T. White, R. McPhedran, and C. de Sterke, "Application of an ARROW model for designing tunable photonic devices," Optics Express **12**(8), 1540–1550 (2004).

[51] K. Okamoto, *Fundamentals of optical waveguides* (Academic Press, 2005).

[52] V. G. Chigrinov, *Liquid Crystal Devices* (Artech House, 1999).

[53] P. G. deGennes and J. Prost, *The Physics of liquid crystals* (Clarendon Press, 1993).

[54] I. C. Khoo, *Liquid Crystals: Physical properties and nonlinear optical phenomena* (Wiley Interscience, 1995).

[55] D. K. Yang and S. T. Wu, *Fundamentals of Liquid Crystal Devices* (John Wiley and Sons, Ltd, 2006).

[56] A. Fratalocchi and G. Assanto, "Discrete propagation and spatial solitons in nematic liquid crystals," Optics Letters **29**(13), 1530–1532 (2004).

[57] A. Piccardi, G. Assanto, L. Lucchetti, and F. Simoni, "All-optical steering of soliton waveguides in dye-doped liquid crystals," Applied Physics Letters **93**(17), 171,104–171,106 (2008).

[58] S. Kumar, *Liquid Crystals: Experimental Study of Physical Properties and Phase Transitions* (Cambridge University Press, 2001).

[59] S. Lagerwall, P. Rudqvist, and D. S. Hermann, *Liquid Crystals - Optical Properties and Basic Devices* (Marcel Dekker, 2003).

[60] S. S. Sun and L. R. Dalton, *Introduction to Organic Electronic and Optoelectronic Materials and Devices -Ch. 27 by S. Gauza* (CRC Press, 2008).

[61] I. Haller, "Thermodynamic and static properties of liquid crystals," Progress in Solid State Chemistry **10**(Part 2), 103–118 (1975).

[62] J. Li, S. Gauza, and S.-T. Wu, "High temperature-gradient refractive index liquid crystals," Optics Express **12**(9), 2002–2010 (2004).

[63] J. Li, S. Gauza, and S.-T. Wu, "Temperature effect on liquid crystal refractive indices," Journal of Applied Physics **96**(1), 19–24 (2004).

[64] J. Li and S.-T. Wu, "Extended Cauchy equations for the refractive indices of liquid crystals," Journal of Applied Physics **95**(3), 896–901 (2004).

[65] R. Tarao, H. Saito, S. Sawada, and Y. Goto, "Advances in liquid crystals for TFT displays," International Symposium Digest of Technical Papers SID 94 Digest pp. 233–236 (1994).

[66] Y.-Q. Lu, X. Liang, Y.-H. Wu, F. Du, and S.-T. Wu, "Dual-frequency addressed hybrid-aligned nematic liquid crystal," Applied Physics Letters **85**(16), 3354–3356 (2004).

[67] L. M. Blinov and V. G. Chigrinov, *Electrooptic Effects in Liquid Crystal Materials* (Springer-Verlag, 1994).

[68] J. Cognard, *Alignment of Nematic Liquid Crystals and Their Mixtures - Molecular Crystals and Liquid Crystals Supplement Series* (Gordon and Breach Science Publishers, 1982).

[69] A. Anawati, *Alignment in cylindrical geometry and dielectric properties* (M.Sc. thesis, Chalmers University of Tecnhology, Sweden, 2005).

[70] M. Green and S. Madden, "Low loss nematic liquid crystal cored fiber waveguides," Applied Optics **28**(24), 5202–5203 (1989).

[71] L. Scolari, *Electro-optical modulator based on liquid crystal photonic crystal fiber* (M.Sc. thesis, Technical University of Denmark, Denmark and DEIS, University of Bologna, Italy, 2005).

[72] K. Nielsen, D. Noordegraaf, T. Sørensen, A. Bjarklev, and T. P. Hansen, "Selective filling of photonic crystal fibres," Journal of Optics A: Pure and Applied Optics **7**(8), L13–L20 (2005).

[73] S. Palmer, "The optical response of liquid crystal cells to a low frequency driving voltage," Liquid Crystals **24**(4), 587–598 (1998).

[74] M. Green and S. Madden, "Low loss nematic liquid crystal cored fiber waveguides," Applied Optics **28**(24), 5202–5203 (1989).

[75] P. Steinvurzel, B. Kuhlmey, T. White, M. Steel, C. M. De Sterke, B. Eggleton, and M. Steel, "Long wavelength anti-resonant guidance in high index inclusion microstructured fibers," Optics Express **12**(22), 5424–5433 (2004).

[76] D. Noordegraaf, L. Scolari, J. Lægsgaard, T. Tanggaard Alkeskjold, G. Tartarini, E. Borelli, P. Bassi, J. Li, and S.-T. Wu, "Avoided-crossing-based liquid-crystal photonic-bandgap notch filter," Optics Letters **33**(9), 986–988 (2008).

[77] J. Lægsgaard, "Modeling of a biased liquid-crystal capillary waveguide," Journal of the Optical Society of America B: Optical Physics **23**(9), 1843–1851 (2006).

[78] S. Burylov, "Equilibrium configuration of a nematic liquid crystal confined to a cylindrical cavity," Journal of Experimental and Theoretical Physics **85**(5), 873–886 (1997).

[79] I. Malitson, "Interspecimen comparison of the refractive index of fused silica," Journal of the Optical Society of America **55**(10), 1205–1209 (1965).

[80] T. Vo-Dinh, *Biomedical Photonics Handbook* (Taylor and Francis Ltd, 2002).

[81] J. Schmitt, "Optical coherence tomography (OCT): a review," IEEE Journal of Selected Topics in Quantum Electronics **5**(4), 1205–1215 (1999).

[82] J. G. Fujimoto, C. Pitris, S. A. Boppart, and M. E. Brezinski, "Optical coherence tomography: An emerging technology for biomedical imaging and optical biopsy," Neoplasia **2**(1-2), 9–25 (2000).

[83] W. Drexler, "Ultrahigh-resolution optical coherence tomography," Journal of Biomedical Optics **9**(1), 47–74 (2004).

[84] P.-L. Hsiung, Y. Chen, T. Ko, J. Fujimoto, C. de Matos, S. Popov, J. Taylor, and V. Gapontsev, "Optical coherence tomography using a continuous-wave, high-power, Raman continuum light source," Optics Express **12**(22), 5287–5295 (2004).

[85] A. Aguirre, N. Nishizawa, J. Fujimoto, W. Seitz, M. Lederer, and D. Kopf, "Continuum generation in a novel photonic crystal fiber for ultrahigh resolution optical coherence tomography at 800 nm and 1300 nm," Optics Express **14**(3), 1145–1160 (2006).

[86] A. Akcay, J. Rolland, and J. Eichenholz, "Spectral shaping to improve the point spread function in optical coherence tomography," Optics Letters **28**(20), 1921–1923 (2003).

[87] J. Love, W. Henry, W. Stewart, R. Black, S. Lacroix, and F. Gonthier, "Tapered single-mode fibres and devices. I. Adiabaticity criteria," IEE Proceedings J Optoelectronics **138**(5), 343–354 (1991).

[88] B. Kuhlmey, H. Nguyen, M. Steel, and B. Eggleton, "Confinement loss in adiabatic photonic crystal fiber tapers," Journal of the Optical Society of America B **23**(9), 1965–1974 (2006).

[89] H. Nguyen, B. Kuhlmey, M. Steel, C. Smith, E. Mägi, R. McPhedran, and B. Eggleton, "Leakage of the fundamental mode in photonic crystal fiber tapers," Optics Letters **30**(10), 1123–1125 (2005).

[90] H. Nguyen, B. Kuhlmey, E. Mägi, M. Steel, P. Domachuk, C. Smith, B. Eggleton, and M. Steel, "Tapered photonic crystal fibres: Properties, characterisation and applications," Applied Physics B **81**(2-3), 377–387 (2005).

[91] M. Lehtonen, G. Genty, and H. Ludvigsen, "Tapered microstructured fibers for efficient coupling to optical waveguides: a numerical study," Applied Physics B **81**(2-3), 295–300 (2005).

[92] A. Bjarklev, J. Broeng, and A. Bjarklev, *Photonic crystal fibers* (Kluwer Academics Publishers, 2003).

[93] T. Dimmick, G. Kakarantzas, T. Birks, and P. Russell, "Carbon dioxide laser fabrication of fused-fiber couplers and tapers," Applied Optics **38**(33), 6845–6848 (1999).

[94] L. Tong, R. R. Gattass, J. B. Ashcom, S. He, J. Lou, M. Shen, I. Maxwell, and E. Mazur, "Subwavelength-diameter silica wires for low-loss optical wave guiding," Nature **426**(6968), 816–819 (2003).

[95] M. Sumetsky, Y. Dulashko, and A. Hale, "Fabrication and study of bent and coiled free silica nanowires: Self-coupling microloop optical interferometer," Optics Express **12**(15), 3521–3531 (2004).

[96] S. Leon-Saval, T. Birks, W. Wadsworth, P. Russell, and M. Mason, "Supercontinuum generation in submicron fibre waveguides," Optics Express **12**(13), 2864–2869 (2004).

[97] F. Fogli, L. Saccomandi, P. Bassi, G. Bellanca, and S. Trillo, "Full vectorial BPM modeling of index-guiding photonic crystal fibers and couplers," Optics Express **10**(1), 54–59 (2002).

[98] P. Steinvurzel, B. Eggleton, C. de Sterke, and M. Steel, "Continuously tunable bandpass filtering using high-index inclusion microstructured optical fibre," Electronics Letters **41**(8), 463–464 (2005).

[99] I. Cristiani, C. Liberale, V. Degiorgio, G. Tartarini, and P. Bassi, "Nonlinear characterization and modeling of periodically poled lithium niobate waveguides for $1.5 - \mu m$-band cascaded wavelength conversion," Optics Communications **187**(1-3), 263–270 (2001).

[100] G. Tartarini, R. Stolte, and H. Renner, "Experimental and theoretical analysis of leaky extraordinary modes in negative uniaxial channel waveguides," Optics Communications **253**(1-3), 109–117 (2005).

[101] G. Tartarini, M. Pansera, T. Alkeskjold, A. Bjarklev, and P. Bassi, "Polarization Properties of Elliptical-Hole Liquid Crystal Photonic Bandgap Fibers," Journal of Lightwave Technology **25**(9), 2522–2530 (2007).

[102] G. Tartarini, T. T. Alkeskjold, L. Scolari, A. Bjarklev, and P. Bassi, "Spectral properties of liquid crystal photonic bandgap fibres with splay-aligned mesogens," Optical and Quantum Electronics **39**(10-11), 913–925 (2007).

[103] R. Herda, O. Okhotnikov, E. Rafailov, W. Sibbett, P. Crittenden, and A. Starodumov, "Semiconductor quantum-dot saturable absorber mode-locked fiber laser," IEEE Photonics Technology Letters **18**(1), 157–159 (2006).

[104] C. Kiely, J. Fink, M. Brust, D. Bethell, and D. Schiffrin, "Spontaneous ordering of bimodal ensembles of nanoscopic gold clusters," Nature **396**(6710), 444–446 (1998).

[105] G. Schmid, *Cluster and colloids. From theory to Applications.* (Wiley-VCH, 1994).

[106] S. Kundu, M. Akimoto, I. Hirayama, S. Kobayashi, K. Takatoh, and M. Indue, "Enhancement of contrast ratio by using ferroelectric nanoparticles in the alignment layer of liquid crystal display," Japanese Journal of Applied Physics **47**, 4751–4754 (2008).

[107] M. Kaczmarek, O. Buchnev, and I. Nandhakumar, "Ferroelectric nanoparticles in low refractive index liquid crystals for strong electro-optic response." Applied Physics Letters **92**(10) (2008).

[108] S. Kobayashi, T. Miyama, N. Nishida, Y. Sakai, H. Shiraki, Y. Shiraishi, and N. Toshima, "Dielectric spectroscopy of metal nanoparticle doped liquid crystal displays exhibiting frequency modulation response," Journal of Display Technology **2**(2), 121–129 (2006).

[109] Y. Shiraishi, N. Toshima, K. Maeda, H. Yoshikawa, J. Xu, and S. Kobayashi, "Frequency modulation response of a liquid-crystal electro-optic device doped with nanoparticles," Applied Physics Letters **81**(15), 2845–2847 (2002).

[110] Y. Reznikov, O. Buchnev, O. Tereshchenko, V. Reshetnyak, A. Glushchenko, and J. West, "Ferroelectric nematic suspension," Applied Physics Letters **82**(12), 1917–1919 (2003).

[111] F. Li, J. L. West, O. Buchnev, Y. Reznikov, C. I. Cheon, A. Glushchenko, V. Reshetnyak, and T. J. Sluckin, "Orientational coupling amplification in ferroelectric nematic colloids," Physical Review Letters **97**(14), 147,801 (2006).

[112] S. Gauza, H. Wang, C.-H. Wen, S.-T. Wu, A. Seed, and R. Dabrowski, "High birefringence isothiocyanato tolane liquid crystals," Japanese Journal of Applied Physics **42**(6A), 3463–3466 (2003).

[113] S.-T. Wu, U. Efron, and L. Hess, "Birefringence measurements of liquid crystals," Applied Optics **23**(21), 3911–3915 (1984).

[114] A. Claesson, S. Smuk, H. Arsalane, W. Margulis, T. Naterstad, E. Zimmer, and A. Malthe-Sorenssen, "Internal electrode fiber polarization controller," Optical Fiber Communications Conference OFC 2003,

Trends in Optics and Photonics Series Vol.86, Postconference Digest (vol.1), 39–40 (2003).

[115] H. Knape and W. Margulis, "All-fiber polarization switch," Optics Letters **32**(6), 614–616 (2007).

[116] T. Erdogan, "Fiber grating spectra," Journal of Lightwave Technology **15**(8), 1277–1294 (1997).

[117] A. Vengsarkar, P. Lemaire, J. Judkins, V. Bhatia, T. Erdogan, and J. Sipe, "Long-period fiber gratings as band-rejection filters," Journal of Lightwave Technology **14**(1), 58–65 (1996).

[118] A. M. Vengsarkar, J. R. Pedrazzani, J. B. Judkins, P. J. Lemaire, N. S. Bergano, and C. R. Davidson, "Long-period fiber-grating-based gain equalizers," Optics Letters **21**(5), 336–338 (1996).

[119] C. Poole, J. Wiesenfeld, D. DiGiovanni, and A. Vengsarkar, "Optical fiber-based dispersion compensation using higher order modes near cutoff," Journal of Lightwave Technology **12**(10), 1746–1758 (1994).

[120] V. Bhatia and A. Vengsarkar, "Optical fiber long-period grating sensors," Optics Letters **21**(9), 692–694 (1996).

[121] L. Rindorf, J. B. Jensen, O. Bang, M. Dufva, L. H. Pedersen, and P. E. Høiby, "Photonic crystal fiber long-period gratings for biochemical sensing," Optics Express **14**(18), 8224–8231 (2006).

[122] B. Eggleton, P. Westbrook, R. Windeler, S. Spalter, and T. Strasser, "Grating resonances in air-silica microstructured optical fibers," Optics Letters **24**(21), 1460–1462 (1999).

[123] A. Diez, T. A. Birks, W. H. Reeves, B. J. Mangan, and P. S. J. Russell, "Excitation of cladding modes in photonic crystal fibers by flexural acoustic waves," Optics Letters **25**(20), 1499–1501 (2000).

[124] M. Nielsen, G. Vienne, J. Folkenberg, and A. Bjarklev, "Investigation of microdeformation-induced attenuation spectra in a photonic crystal fiber," Optics Letters **28**(4), 236–238 (2003).

[125] P. Steinvurzel, E. Moore, E. Magi, B. Kuhlmey, and B. Eggleton, "Long period grating resonances in photonic bandgap fiber," Optics Express **14**(7) (2006).

[126] P. Steinvurzel, E. Moore, E. Magi, and B. Eggleton, "Tuning properties of long period gratings in photonic bandgap fibers," Optics Letters **31**(14), 2103–2105 (2006).

[127] Y. Jeong, B. Yang, B. Lee, H. S. Seo, S. Choi, and K. Oh, "Electrically controllable long-period liquid crystal fiber gratings," IEEE Photonics Technology Letters **12**(5), 519–521 (2000).

[128] Y. Jeong, H.-R. Kim, S. Baek, Y. Kim, Y. W. Lee, S.-D. Lee, and B. Lee, "Polarization-isolated electrical modulation of an etched long-period fiber grating with an outer liquid-crystal cladding," Optical Engineering **42**(4), 964 (2003).

[129] H.-R. Kim, Y. Kim, Y. Jeong, S. Baek, Y. W. Lee, B. Lee, and S.-D. Lee, "Suppression of the cladding mode interference in cascaded long period fiber gratings with liquid crystal claddings," Molecular Crystals and Liquid Crystals **413**, 399–406 (2004).

[130] P. Agrawal, *Fiber-Optic Communication Systems* (John Wiley and Sons, 1997).

[131] H. Yokota, K. Kamoto, J.-i. Igarashi, N. Mouri, and Y. Sasaki, "An ASE Reduction Filter Using Cascaded Optical Fiber Grating Couplers in EDFA Repeater," Optical Review **9**(1), 9–12 (2002).

[132] J. Qian and H. Chen, "Gain flattening fibre filters using phase-shifted long period fibre gratings," Electronics Letters **34**(11), 1132–1133 (1998).

[133] P. Sahu, "Thermally tunable EDFA gain equalizer using point symmetric cascaded Mach-Zehnder coupler," Optics Communications **281**(4), 573–579 (2008).

[134] M. Ali, A. Elrefaie, R. Wagner, and S. Ahmed, "A detailed comparison of the overall performance of 980 and 1480 nm pumped EDFA cascades in WDM multiple-access lightwave networks," Journal of Lightwave Technology **14**(6), 1436–1448 (1996).

[135] T. Alkeskjold, J. Laegsgaard, A. Bjarklev, D. Hermann, J. Broeng, J. Li, S. Gauza, and S.-T. Wu, "Highly tunable large-core single-mode liquid-crystal photonic bandgap fiber," Applied Optics **45**(10), 2261–2264 (2006).

[136] L. Wei, E. Khomtchenko, T. Alkeskjold, and A. Bjarklev, "Photolithography of thick photoresist coating for electrically controlled liquid crystal photonic bandgap fiber devices," accepted for publication in Electronics Letters (2009).